PROBING NANOSCALE LIGHT-MATTER INTERACTIONS IN PLASMONIC

NANOSTRUCTURES

A Dissertation

Submitted to the Faculty

of

Purdue University

by

Harsha Reddy

In Partial Fulfillment of the

Requirements for the Degree

of

Doctor of Philosophy

May 2020

Purdue University

West Lafayette, Indiana

THE PURDUE UNIVERSITY GRADUATE SCHOOL
STATEMENT OF DISSERTATION APPROVAL

Dr. Vladimir M. Shalaev, Co-Chair

    School of Electrical and Computer Engineering

Dr. Alexandra Boltasseva, Co-Chair

    School of Electrical and Computer Engineering

Dr. Andrew M. Weiner

    School of Electrical and Computer Engineering

Dr. Xianfan Xu

    School of Mechanical Engineering

Approved by:

    Dr. Dimitri Peroulis

        Head of the School of Electrical and Computer Engineering

To my family

ACKNOWLEDGMENTS

I would like to start by thanking my advisor Vlad Shalaev. He gave me complete freedom to pursue my research interests and provided unwavering support throughout my PhD. Especially, during the times when my experiments appeared to be going nowhere, your constant encouragement and motivation pushed me to work harder. I will always remember the passion and excitement with which you spoke about science and the rich discussions we had over the years. Thank you for all your guidance and more importantly for giving me an opportunity to work in your team.

I would like to extend my gratitude to Sasha, who has been my co-advisor, for all her guidance and support. Thank you for all the meticulous feedback you provided on preparing scientific articles; your careful feedback taught me how to write scientific documents. I would also like to thank my other committee members Prof. Andrew M. Weiner and Prof. Xianfan Xu for kindly agreeing to be part of my thesis committee.

I was fortunate to have had a chance to work with several wonderful collaborators. In my early years, I closely worked with Urcan Guler (a postdoc in our group at that time), who regularly took time to mentor me and offer necessary guidance. I would also like to thank my other group mates in Purdue including Zhouxian, Rohith, Di, Naresh, Krishnakali, Aveek, Misha, Sajid, Soham, Deesha, JingJing and Jongbum for kindly helping me with various aspects related to simulation, fabrication and characterization during my PhD.

I also had a chance to closely work with wonderful collaborators at the University of Michigan, Ann Arbor. In particular, I was very lucky to have had a chance to extensively interact with Edgar since my undergraduate days. From our discussions, I learned several technical aspects ranging from designing electrical circuits to carefully building experimental setups. More importantly, I learnt how to systematically tackle a scientific problem from Edgar. I will always remember our late evening dis-

cussions and his willingness to put aside other pressing matters to offer guidance and help us with troubleshooting experiments. I was also lucky to have had a chance to closely work with Kun Wang at the University of Michigan, Ann Arbor. Together, we developed the experimental platform that enabled the determination of hot-carrier energy spectrum.

I want to thank my good friends Punya, Vasu, Surabhi, Vaibhav and Prabhu Kumar for making my stay at Purdue fun and memorable. I will cherish and remember our countless late night discussions, habits and qualities that I learned from you, our road trips across mid-west and of course the crazy *Gedanken-Experiments* that we conducted!

My visits to Ann Arbor, which for a period of time were as frequent as 3-4 times a month, were always quite enjoyable. I am immensely indebted to my cousin Pramod and sister-in-law Swathi, with whom I stayed during these visits. My adorable niece Medha and nephew Sidhu made these trips doubly enjoyable with all their curious questions (which at times got me stumped) and fun discussions during our bedtime story sessions.

Finally, I want to thank my parents for their enduring love and all the sacrifices they had to make to ensure that we (me and my siblings) received good education. My mom for her constant love and for making sure that I stay healthy; my siblings Sada and Deepi for always being there for me—this PhD would not be possible without them. I will conclude by thanking my two mentors, my dad and Pramod, who have contributed immensely to my growth as a person. Thank you very much for everything you patiently taught me (and continue to teach me), I wouldn't have been half the person I am without your constant guidance and support.

TABLE OF CONTENTS

LIST OF FIGURES

Figure   Page

ABSTRACT

Reddy, Harsha Ph.D., Purdue University, May 2020. PROBING NANOSCALE LIGHT-MATTER INTERACTIONS IN PLASMONIC NANOSTRUCTURES. Major Professor: Vladimir M. Shalaev.

This thesis describes the development of experimental methods to probe the nanoscale light-matter interactions in photonic and plasmonic nanostructures. The first part of this thesis presents the experimental findings on the temperature evolution of optical properties in important plasmonic materials. Understanding the influence of temperature on the optical properties of thin metal films—the material platforms for plasmonics—is crucial for the design and development of practical devices for high temperature applications in a variety of research avenues, including plasmonics, novel energy conversion technologies and near-field radiative heat transfer. We will first introduce a custom built experimental platform comprising a heating stage integrated into a spectroscopic ellipsometer setup that enables the determination of optical properties in the wavelength range from 370 nm to 2000 nm at elevated temperatures, from room temperature to 900 °C. Subsequently, the temperature dependent complex dielectric functions of gold, silver and titanium nitride thin films that were obtained using the above described experimental platform will be presented. Furthermore, the underlying microscopic physical processes governing the temperature evolution and the role of film thickness and crystallinity will be discussed. Finally, using extensive numerical simulations we will demonstrate the importance of incorporating the temperature induced deviations into numerical models for accurate multiphysics modeling of practical high temperature nanophotonic applications.

The second part of this thesis focuses on the development of experimental techniques to quantify the nanoscale steady-state energy distributions of plasmonic hot-

carriers. Such hot-carriers have drawn significant research interest in recent times due to their potential in a number of applications including catalysis and novel photodetection schemes circumventing bandgap. However, direct experimental quantification of steady-state energy distributions of hot-carriers in nanostructures, which is critical for systemic progress, has not been possible. Here, we show that transport measurements from suitably chosen single molecular junctions can enable the quantification of plasmonic hot-carrier distributions generated via plasmon decay. The key idea is to create single molecule junctions—using carefully chosen molecules featuring sharp molecular resonances—between a plasmonic nanostructure and the gold tip of a scanning tunneling microscope, and quantify the hot-carrier distributions form the current flowing through the molecular junctions with and without plasmonic excitation at various voltage biases. Using this approach, we reveal the fundamental role of surface-scattering assisted absorption—Landau damping—and the contributions of different plasmonic modes towards hot-carrier generation in tightly confined nanostructures. The approach pioneered in this work can potentially enable nanoscale experimental quantification of plasmonic hot-carriers in key nanophotonic and plasmonic systems.

1. INTRODUCTION

The whole field of plasmonics, one way or the other, is about confining and control-
ling light at the nanoscale—at length scales much smaller than the limits imposed
by the diffraction limit [1–3]. As elegantly described in Ref [4], the key to confin-
ing light to deep sub-diffraction length scales lies in introducing free carriers to the
material system under consideration. The key arguments of this physical picture are
outlined below. Consider a simple Fabry-Pérot resonator of characteristic dimension
l as shown schematically in Figure 1.1 below. The resonator supports an electro-
magnetic mode with a wavelength of $\lambda = 2nl$, where n is the refractive index of the
medium inside the cavity. To satisfy the boundary conditions, the spatial variation
of the electric and magnetic fields manifests as a harmonic dependence on length as
$sin(2n\pi x/\lambda)$ and $cos(2n\pi x/\lambda)$, respectively. As this optical mode oscillates the en-
ergy is transferred between electric ($u_E \approx \frac{1}{2}\epsilon E^2$) and magnetic ($u_H \approx \frac{1}{2}\mu H^2$) fields
every half period. Here ϵ and μ are the permittivity and permeability of the optical
medium in the cavity, respectively. Using $H = \sqrt{\frac{\epsilon}{\mu}}E$ it follows that $u_H = u_E$. As a
result, the maximum stored energy in electric and magnetic fields is equal and more
importantly it keeps oscillating between the two fields every half cycle, resulting in
self-sustaining oscillations. Next, if the dimension of the resonator l is reduced to
below $\frac{\lambda}{2n}$ the spatial dependence of the electric field modifies as $sin(\pi x/l)$. Using
the Maxwell's curl equation $\nabla X \vec{H} = \epsilon \frac{\partial \vec{E}}{\partial t}$, we then get $H = \frac{2nl}{\lambda}\sqrt{\frac{\epsilon}{\mu}}E$. Further, it
follows that the maximum energy stored in the magnetic field in this sub-λ mode
$u_H < u_E$. As a result, the *self-sustaining* oscillations are no longer possible and the
energy leaks out of the resonator (Figure 1.1 c, d), as expected from the diffraction
limit. The energy balance between u_H and u_E can however be restored at specific
frequencies—that depend on the geometry of the resonator—by introducing free car-
riers into the resonator. These free carriers can store part of the total energy as

kinetic energy $u_K = \frac{1}{2}\epsilon_\circ \left(\frac{\omega_p^2}{\omega^2}\right) E^2$, where ω_p is the plasma frequency of free carriers and $\epsilon_\circ$ is the permittivity of free space. The energy balance $u_E = u_H + u_K$ can thus be restored at appropriate frequencies that depend on both the geometry and the total free carriers in the resonator, thus enabling sub-diffraction confinement of light. These frequencies where the energy balance is established are precisely the surface plasmon polariton (SPP) frequencies ω_{SPP}. Metals are a natural material choice to reach the sub-diffraction light confinement. Specifically, in a metal nanoparticle, its boundaries serve as the resonator walls and the vast number of free electrons carry the necessary kinetic energy to restore the energy balance. However, beating the diffraction limit comes at a price—a substantial portion of the total energy in the resonator is stored in the kinetic energy of free electrons. This kinetic energy will eventually be lost by either radiatively, by emitting photons, or non-radiatively via surface scattering assisted absorption, electron-electron, electron-phonon and other scattering mechanisms. The two major research efforts of this thesis are intricately related to the above outlined non-radiative decay pathway of surface plasmons. These two directions are described in detail below.
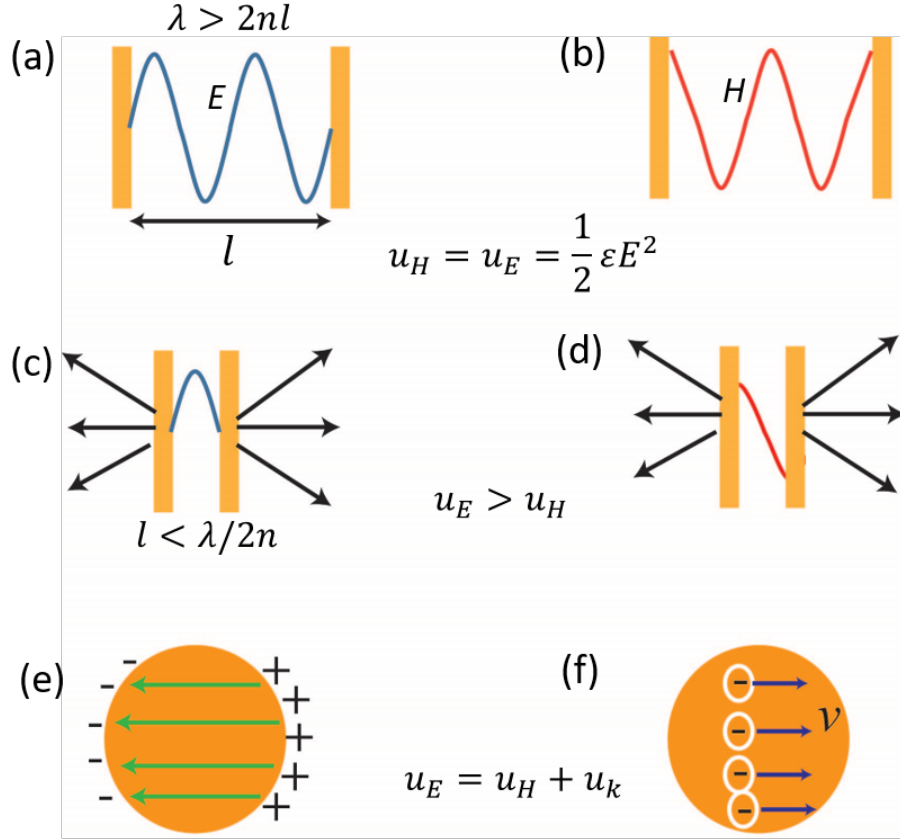
Fig. 1.1. Schematic of a cavity with dimensions larger than $\lambda/2n$ showing the Electric (E) and Magnetic (M) fields of a supported cavity mode, respectively. This cavity supports energy balance between the energy stored in electric (u_E) and magnetic fields (u_H). (c) and (d): Reducing the cavity dimension below the diffraction limit results in larger electric field energy density compared with the magnetic field energy density. Self-sustaining oscillations are no longer possible and the energy in the cavity leaks out. (e) and (f): Introducing the free carriers into the cavity will restore energy balance at appropriate frequencies, which are the surface plasmon polariton frequencies. Idea of the schematic adapted from Ref [4].

1.1 Temperature evolution of optical properties in plasmonic materials and metasurfaces

The first part of this thesis focuses on understanding the consequences of non-radiative decay on the optical properties of the constituent materials. To elaborate, as the energy stored in the kinetic energy of free electrons is dissipated via non-radiate losses the temperature of the plasmonic component under study inevitably increases. Depending on the application, the temperature rise can be anywhere between a fraction of a degree Celsius to several hundreds of degrees Celsius. For instance, in heat assisted magnetic recording (HAMR) it has been estimated that the temperature increase in a plasmonic near field transducer (NFT)—a plasmonic nanoantenna—is close to 500 °C [5–7]. Other self-heating applications imposing high temperatures include spacers, photothermal therapy and biosensors [8–11]. In addition to these self-heating applications where often times heating is unintentional and unavoidable, in the recent times, there has been a growing interest in alternative energy conversion technologies that require metal based nanophotonic components intentionally heated extreme temperatures.
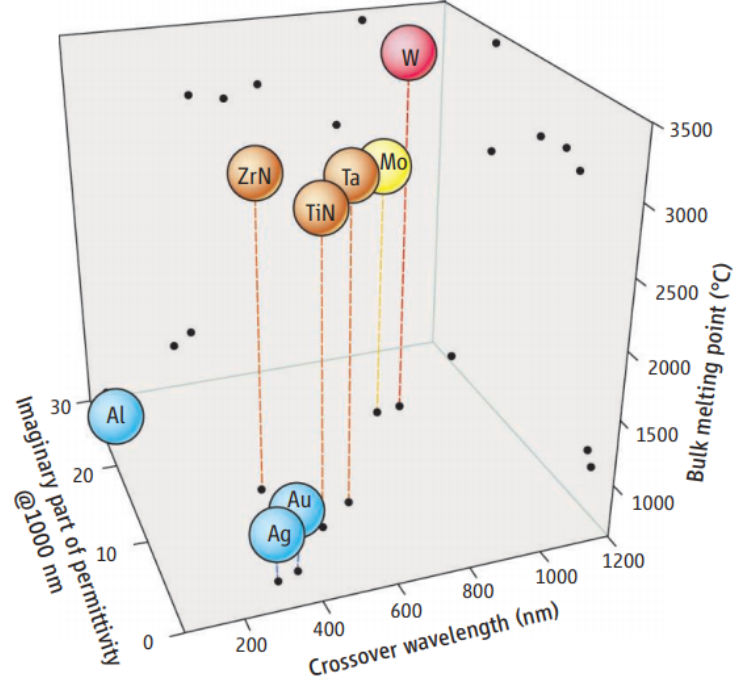
Fig. 1.2. Plasmonic behavior vs bulk melting point for different metals. Refractory metals TiN and ZrN possess optical properties comparable to Au and Ag, albeit higher losses, but have melting points nearly three times larger than conventional noble metals. Picture taken from Ref [12].

For example, the thermal energy conversion technologies thermophotovoltaics (TPV) and solar thermophotovoltaics (STPV) require spectrally selective emitters and absorbers made out of metal based plasmonic elements operating at temperatures as high as 1000 °C [13, 14]. Conventional plasmonic material platforms—noble metals gold (Au), silver (Ag) and copper (Cu)—however, have a relatively low melting point, about 1000 °C. Furthermore, the melting point is known to reduce further upon nanostructuring due to melting point depression [15], rendering noble metals unsuitable for several of these practical high temperature nanophotonic applications. Due to these limitations with noble metals, in recent years, there have been research efforts aimed at identifying and developing alternate plasmonic material platforms that display optical properties comparable to noble metals, while simultaneously ex-

hibiting superior thermal stability [16, 17]. During this search, researchers identified the so called *refractory plasmonic material* such as, titanium nitride (TiN) and zirconium nitride (ZrN), that show optical properties similar to Au and Ag, but have a bulk melting point around 3000 °C [12] (see Figure 1.2). The superior thermal stability of refractory materials has been demonstrated in the past [18]. However, an important question pertinent to both noble metals and refractory metals is the following: *how do the optical properties evolve with temperature*? Addressing this question experimentally and identifying the underpinning microscopic physical processes governing the temperature evolution in important plasmonic materials forms the central focus of the first part of this thesis.

Beyond the fundamental utility of having a reliable and resourceful database of elevated temperature optical properties of widely used plasmonic materials, probing the temperature evolution also has important practical implications. Specifically, with increasing temperature various physical mechanisms including, increasing electron-phonon interactions, reducing carrier densities, and the deviations in the electronic bandstructure (and the associated deviations in the electron effective mass) are expected to modify the optical response of the material under study [19]. Despite these deviations, the numerical modeling of aforementioned high temperature nanophotonic applications has largely relied on the room temperature optical constants. Using rigorous computational models, we demonstrate that this approach of employing room temperate optical constants to model the high temperature situations produces results that are in stark contrast with those obtained using the appropriate temperature dependent optical constants. These numerical simulations along with their utility for practical high temperature applications will also be discussed in detail in the first part of this thesis.

1.2 Quantification of plasmonic hot-carrier energy distributions via transport measurements through single molecule junctions

The later part of this thesis is focused towards the development of experimental methods that enabled quantification of the energy spectrum of so called plasmonic hot-carriers. The term "hot-carriers" essentially refers to those carriers—electrons and holes—with energy distributions that deviate from equilibrium Fermi-Dirac distribution [20]. Such non-equilibrium hot-carriers are expected to arise in plasmonic nanostructures due to the non-radiative decay of surface plasmons [21] that can be excited in metallic nanostructures under external illumination as outlined above. It is worth noting that the plasmon assisted hot-carrier generation has a key difference from the simple photon assisted hot-carrier generation via interband absorption. In case of interband absorption, the transition is "direct" i.e the initial state and the final excited state of the electron have nearly the same momentum. However, as depicted in Figure 1.3, the scheme of plasmon assisted hot-carrier generation can enable "indirect" transitions, where the initial and the excited sates differ in momentum/electronic k vector [4]. Such indirect transitions are only possible with plasmons because, when carefully engineered, plasmons can have orders of magnitude larger momentum than free space photons in tightly confined nanostructures, which is the key to enable the indirect transitions [4]. Photons, however, carry negligible momentum and therefore they alone cannot mediate the indirect transitions. The possibility of enabling indirect transitions, opens up avenues to generate hot-carriers via intraband transitions (Figure 1.3) without bandgap limitations. This key advantage has been one the major driving forces behind the immense research interest in the field.
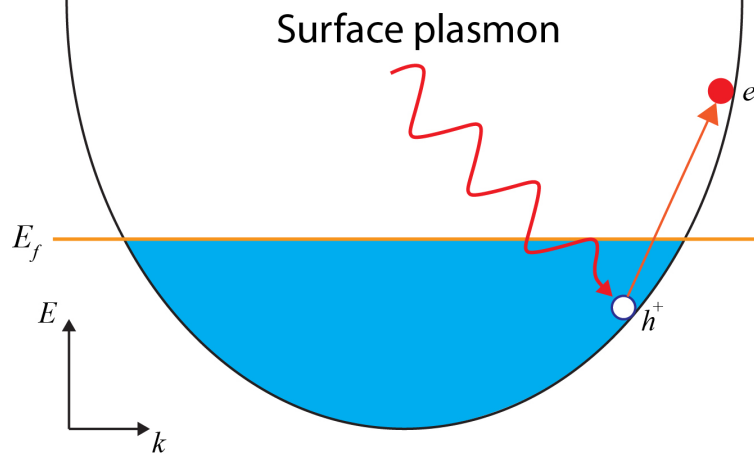
Fig. 1.3. Schematic of plasmon assisted hot-carrier generation. The energy from a surface plasmon is non-radiatively lost to an electron residing below the Fermi energy E_f and knocks it over to an excited energy state above the Fermi energy. This process leads to the generation of energetic electron-hole pairs —"hot-carriers".

Such energetic hot-carriers are of great fundamental interest due to their potential for the development of a variety of novel technologies, including plasmon-driven photochemistry [22–25], solar-energy harvesting devices [21], and efficient photodetectors operating below bandgap [26–28]. Given the considerable potential of plasmonic nanostructures for hot-carrier generation, a number of researchers have theoretically explored hot-carrier energy distributions in a variety of nanostructure geometries under external illumination [29–31], which set the ultimate limits to the performance efficiencies of the aforementioned application concepts. However, such computational approaches involve numerous assumptions on the dominant relaxation pathways of hot-carriers as well as material properties [32] that greatly influence the theoretical predictions and lead to a large uncertainty in the estimated hot-carrier energy spectrum [31, 33]. For example, some newer calculations have even suggested that the deviations from the equilibrium Fermi-Dirac distribution are negligibly small, questioning if hot-carrier distributions even have a discernible effect [34]. This uncertainty surrounding the contrasting predictions from competing theoretical frameworks is a

frustrating situation as a precise knowledge of the energy spectrum of the generated hot-carriers holds key for both making systematic progress and for the design and development of practical hot-carrier technologies.

To resolve this uncertainty, experimental methods that enable the quantification of nanoscale hot-carrier energy distributions are needed. However, such experimental approaches have remained scarce thus far, due to the immense experimental and technical challenges associated with measuring the nanoscale hot-carrier energy spectrum. While the recent optical approaches [35] provide crucial information into the transient hot-carrier distributions, the spatial resolution is limited to 200 μm preventing the quantification of hot-carrier distributions at the nanoscale where several interesting theoretical predictions have been put forward [29–31].

We will present how a scanning probe-based technique that measures charge transport in single molecules [36–38], when combined with nanoplasmonic experimental methods, can be leveraged to directly quantify the nanoscale steady-sate energy distributions of plasmonic hot-carriers. As a demonstration of this technique, we experimentally quantify the hot-carrier energy distributions generated in an ultra-thin gold film via the decay of surface plasmon polaritons. Further, we compare our experimental findings with state-of-the-art *ab initio* density functional theory (DFT) calculations and identify the theoretical frameworks that best describe and model our experimental findings. Finally, by considering Au films of different thicknesses and performing a spatial map we reveal the fundamental role of Landau damping and the contributions of different plasmonic modes towards hot-carrier generation. These findings and the development of the related experimental methods comprise the second part of this thesis.

1.3   Thesis overview

The rest of this thesis is organized as follows:

Chapter 2 describes the experimental platform that was developed to investigate the temperature evolution of optical properties. A discussion on the analytical models that will be used to model the complex dielectric function of plasmonic metals will be presented. Finally, the details of the sample preparation are also discussed.

Chapter 3 presents the experimentally measured temperature dependencies in gold, sliver and titanium nitride thin films. The underlying physical mechanisms dictating the temperature evolution will be discussed in detail. Numerical models of some practical high temperature nanophotonic applications incorporating the experimentally measured temperature induced deviations will also be presented.

Chapter 4 introduces the theoretical framework and explains in detail the central ideas of how charge transport measurements through through suitably chosen molecular junctions enable the quantification of plasmonic hot-carrier energy distributions. The preparation of ultra-thin gold films and the synthesis details of the relevant molecules that will be used for the experiments will also be discussed.

Chapter 5 details the experimental setup that simultaneously allows the excitation of surface plasmon polaritons (and therefore the hot-carriers) and the measurement of charge transport through single molecule junctions via break-junction technique. Various control experiments that rule out the possible role of temperature differentials and simple light induced transport features will be discussed. Finally, the methods used to experimentally map the transmission characteristics will be outlined.

Chapter 6 discusses the measured experimental findings of hot-carrier energy distributions in ultra-thin gold films due to the non-radiative decay of SPPs. The dependence of hot-carrier generation on the film thickness will also be presented.

Chapter 7 describes the first-principle theoretical framework that enabled the estimation of steady-state hot-carrier energy distributions. The estimates from competing theoretical frameworks will be presented. Additionally, by comparing the theoretical predictions with the measured experimental findings from **Chapter 6** the suitable theoretical framework that best models our experimental findings will be identified. Furthermore, using the experimental findings, the insights from the den-

sity functional theory calculations and electromagnetic field profile simulations the fundamental role of Landau damping and the relative contributions from different plasmonic modes will be detailed.

2. EXPERIMENTAL APPROACH TO MEASURE THE TEMPERATURE EVOLUTION OF OPTICAL PROPERTIES

Most of the material presented in this chapter is taken verbatim from the following papers: Reddy, Harsha et al. "Temperature-dependent optical properties of gold thin films", Optical Materials Express, 6(9), 2016; Reddy, Harsha et al. "Temperature-dependent optical properties of single crystalline and polycrystalline silver thin films", ACS Photonics, 4(5), 2017; Reddy, Harsha et al. "Temperature-dependent optical properties of plasmonic titanium nitride thin films", ACS photonics, 4(6), 2017.

This chapter first describes the experimental methods that were developed to probe the *in-situ* elevated temperature optical properties of the samples under study. This is followed by a discussion on the analytical models that were used to determine the frequency dependent complex dielectric function ($\hat{\epsilon}(\omega)$) at various temperatures. Details about the preparation of samples used in this work are also included in this chapter.

2.1 Experimental platform and approach to determine the optical constants

A custom built experimental platform consisting of a heating stage (Linkam Scientific model TS1500V) integrated onto a variable angle spectroscopic ellipsometer (VASE) setup was used to probe the optical properties as a function of temperature [19]. The stage has the capability of heating the sample to temperatures up to 1500 °C and a rated temperature stability of 2 °C. To prevent rapid thermal expansion, the samples were heated and cooled at a rate of 3 °C/min. In addition, the stage was operated under high vacuum ($\sim 10^{-6}$ torr). Over $400 - 450$ °C the background

thermal radiation saturates the detector, preventing reliable data retrieval. To reduce the intensity of the background thermal radiation reaching the ellipsometer detector, a pinhole was placed in the reflected beam path prior to the detector as shown in Figure 2.1. The pinhole size was adjusted such that more than 85% of the reflected beam intensity reaches the detector, while suppressing most of the background radiation. Prior to all the temperature dependent measurements, a calibration was performed using a Si/SiO_2 waver from J. A. Woolam company. Since most of the reflected beam reaches the detector (> 85 %), introducing the pinhole didn't lead to any noticeable differences in the optical properties when compared to the case without the pinhole.
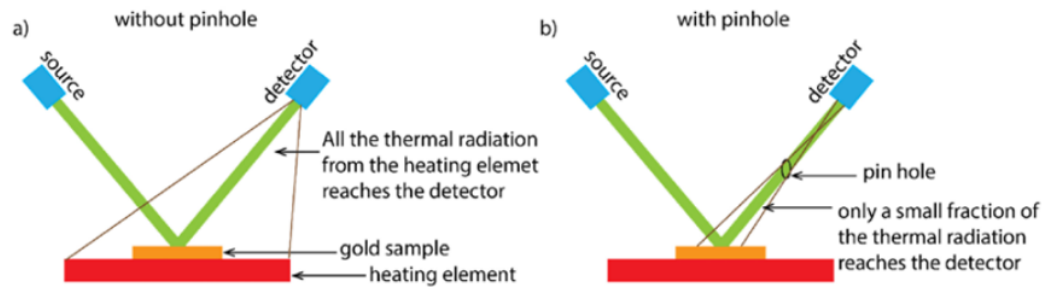
Fig. 2.1. Schematic describing the role of pinhole. (a) Without the pinhole, thermal radiation from a large surface area reaches the detector, thereby saturating the detector at temperatures beyond 450 °C. (b) Placing the pinhole in the beam path reduces the intensity of the background emission reaching the detector, while still allowing most of the reflected beam to pass through.
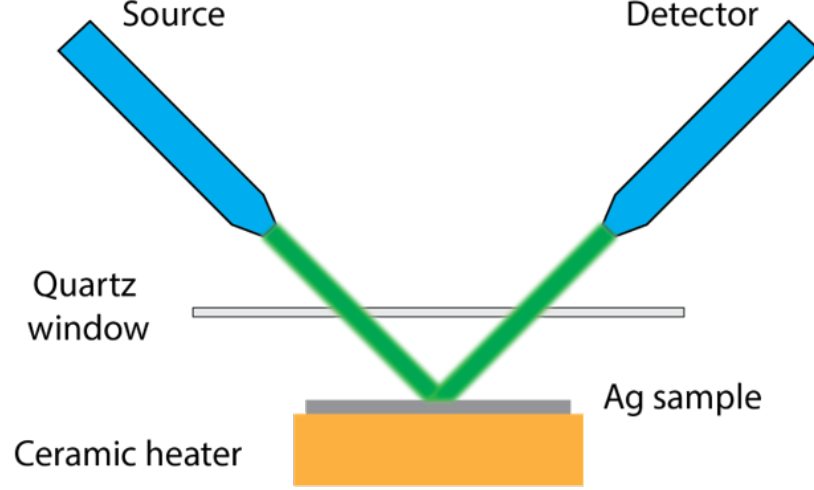
Fig. 2.2. Schematic of the high temperature ellipsometer setup. A quartz window provides optical access to the sample placed on a ceramic heater under high vacuum.

Figure 2.2 shows the schematic of the experimental setup. The ellipsometer measurements Ψ and Δ are related to the ratio of complex reflection coefficients of p ($\hat{R}_p$) and s ($\hat{R}_s$) polarizations as:

$$\frac{\hat{R}_p}{\hat{R}_s} = tan(\Psi)e^{i\Delta} \tag{2.1}$$

The quartz window located parallel to the sample surface in the beam path introduces offsets into the ellipsometer measurements. Before each set of temperature dependent measurements, we calibrate the window offsets at room temperature and correct the subsequent high temperature measurements. Our approach to calibrating and correcting window offsets is similar to Ref [39]. This approach is briefly outlined below.

The reflection from the sample can be represented using Jones matrix algebra as $\begin{bmatrix} \hat{R}_p & 0 \\ 0 & \hat{R}_s \end{bmatrix}$. The Jones matrix for transmission through the window can be written as

$\begin{bmatrix} \hat{a} & 0 \\ 0 & \hat{b} \end{bmatrix}$ correspond to the p- and s- polarization transmission coefficients of the quartz window, respectively. Together with the window the overall reflection matrix would become:

$$\begin{bmatrix} \hat{a} & 0 \\ 0 & \hat{b} \end{bmatrix} \begin{bmatrix} \hat{R}_p & 0 \\ 0 & \hat{R}_s \end{bmatrix} \begin{bmatrix} \hat{a} & 0 \\ 0 & \hat{b} \end{bmatrix} = \begin{bmatrix} \hat{a}^2 \hat{R}_p & 0 \\ 0 & \hat{b}^2 \hat{R}_s \end{bmatrix}, \tag{2.2}$$

$$\implies tan(\Psi')e^{i\Delta'} = \frac{\hat{a}^2 \hat{R}_p}{\hat{b}^2 \hat{R}_s}, \tag{2.3}$$

where Ψ' and Δ' are the ellipsometer measurements with the window in the beam path.

$$\implies \frac{tan(\Psi')}{tan(\Psi)} = \frac{|\hat{a}^2|}{|\hat{b}^2|} \tag{2.4}$$

$$\text{and } \Delta' - \Delta = 2(\delta_a - \delta_b). \tag{2.5}$$

Here δ_a and δ_b are the phases of $\hat{a}$ and $\hat{b}$, respectively. For each set of temperature dependent measurements, we collected the ellipsometer data on metal films with and without the window in the beam path. Subsequently, the correction factors for $tan(\Psi)$ and offsets in Δ were computed at each wavelength using the above expressions. These correction factors and offsets were then used to correct the ellipsometer measurements at high temperatures.

2.2 Ellipsometer models

The real and imaginary parts of the frequency dependent complex dielectric function ($\hat{\epsilon}(\omega) = \epsilon_1 + \epsilon_2$) were then extracted by fitting the corrected VASE data with either a Drude Lorentz (DL) model or a Drude critical point (DCP) models as shown below:

$$\hat{\epsilon}(\omega) = \epsilon_\infty - \frac{\omega_p^2}{\omega^2 + i\Gamma_D\omega} + \sum_{j=1}^{N} \frac{C_j}{(\hbar\omega_j)^2 - (\hbar\omega)^2 - i\gamma_j(\hbar\omega)} \tag{2.6}$$

$$\hat{\epsilon}(\omega) = \epsilon_\infty - \frac{\omega_p^2}{\omega^2 + i\Gamma_D\omega} + \sum_{j=1}^{N} C_j\omega_j \left(\frac{e^{i\phi_j}}{\omega_j - \omega - i\gamma_j} + \frac{e^{-i\phi_j}}{\omega_j + \omega + i\gamma_j} \right) \tag{2.7}$$

where ϵ_∞, ω_p and Γ_D are the background dielectric constant, plasma frequency and Drude broadening, respectively. Furthermore, C_j, Ω_j, γ_j and ϕ_j are the oscillator strength, energy, damping and phase, respectively. The Drude terms describe the free electron response while the Lorentz oscillators and critical points account for the interband absorption. We use Lorentz oscillators for Ag and TiN while for Au a critical point model was used. Critical points are better suited over Lorentz oscillators for describing asymmetric line-shapes, which are characteristic features of interband transitions in Au [19].

While using the DCP model the oscillator phases were fixed at $-\pi/4$. We treat the optically thick films (thickness larger than 100 nm) as semi-infinite layers while retrieving the dielectric function from the VASE data. For thin films (50 nm and below), substrate reflections from metal/substrate interface accumulates a thickness dependent phase. We account for these additional reflections using a two layer model consisting of a Cauchy layer for the substrate and a DL or DCP model on top for the metal film. We first collect VASE data on bare substrates (glass, MgO or Sapphire) and extract their optical constants by fitting with a Cauchy model. These optical constants were used as fixed numbers in the two layer model and the optical constants of the films were retrieved via fitting. During deposition, we monitored the thicknesses using a crystal oscillator. Subsequently, the thicknesses were verified both from SEM cross-sectional imaging and VASE fits, and were found to be consistent with the crystal oscillator readings. For thin films, along with the oscillator phases the thickness was kept fixed while fitting the elevated temperature VASE data. The rest of the terms were provided as free parameters. The mean square errors (MSEs) for all the measurements were less than 2 indicating that the fits were good.

2.3 Sample preparation

A variety of film thicknesses and crystallinities were prepared for the temperature dependent studies. The poly-crystalline Au films of varying thicknesses were deposited on 1-mm thick glass substrates using an electron beam evaporator (CHA industries model 600) at room temperature and a base pressure of $\sim 10^{-6}$ torr. No adhesion/wetting layer was used. Thick single-crystalline Au films were purchased from Phasis Sarl. These films were grown at 400 ° C on mica substrates to obtain the crystalline phase [19].

Both single-crystalline and poly-crystalline Ag films were grown on 10 x 10 x 0.5 mm (100) MgO substrates from CrysTec. A 99.99% pure Ag target was used for both e-beam evaporation and sputtering. Prior to the film growth, the substrates were sonicated in acetone, isopropanol and methanol (5 minutes in each solvent). Single-crystalline Ag films were prepared by DC magnetron sputtering (PVD products) at a base pressure of 10^{-8} torr. A thin TiN layer of 4 nm thickness was used as a wetting layer. The wetting layer enables crystalline growth. This was deposited from a Ti target under nitrogen and argon flow (8:2 sccm) at 800 °C and 200 W power with a base pressure of 10^{-8} torr. Subsequently, sliver films were grown under argon flow at 50 W. The growth parameters of silver were optimized based on feedback from extensive optical (ellipsometer), microstructure (XRD) and surface (AFM) characterizations. The XRD results on optimized SC films are shown in Figure 2.3 [40].
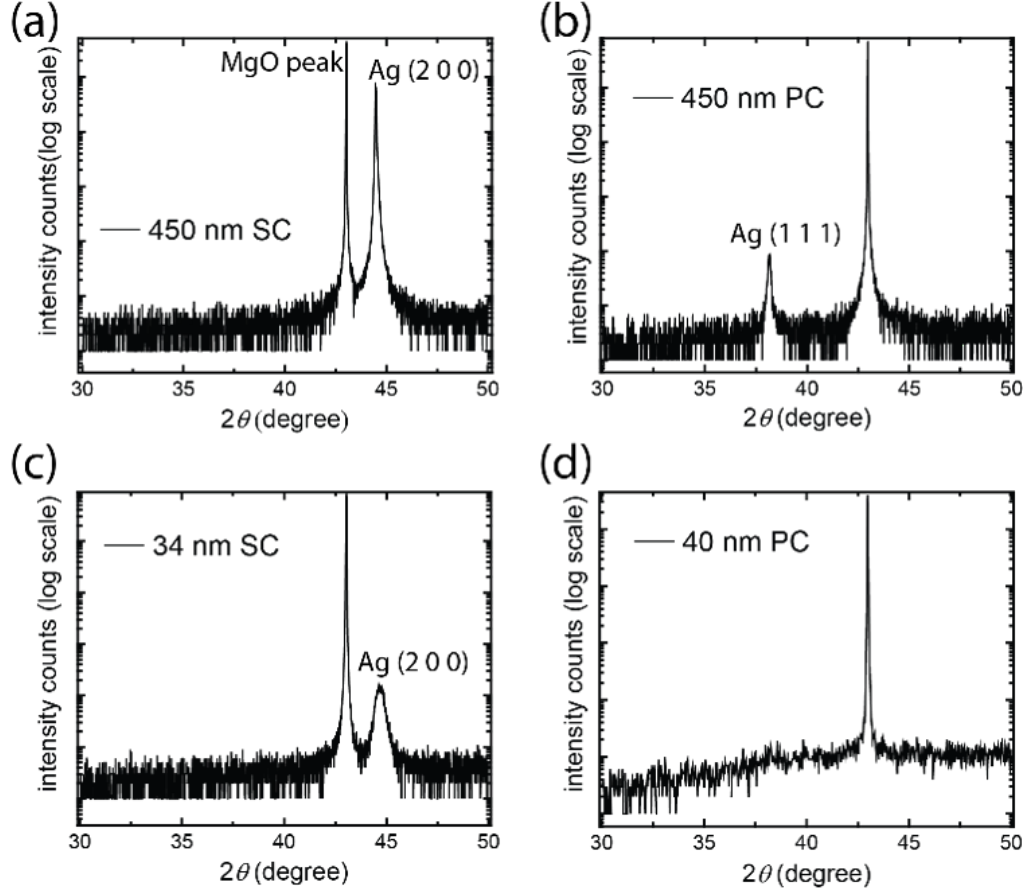
Fig. 2.3. X-ray diffraction measurements on single-crystalline and poly-crystalline silver films of varying thicknesses. The peak near 43° corresponds to (1 0 0) MgO. In sputtered Ag (a, c), an additional peak occurs at 44.5°. This corresponds to (2, 0, 0) silver. In thick poly-crystalline films the peak is at 38.2°, corresponding to Ag (1, 1, 1) (b). No Ag peak was observed in 40 nm poly-crystalline films (d).

The TiN samples were DC magnetron sputtered from a Ti target (Plasmaterials, 99.995 %) onto (001) sapphire substrates (GT Advanced Technologies, 10 x 10 x 0.5 mm). The substrate was held at 850 °C and a base pressure of 10^{-8} torr (200 W; 8 sccm N_2 and 2 sccm Ar flow) [41].

3. EXPERIMENTAL RESULTS

Most of the material presented in this chapter is taken verbatim from the following papers: Reddy, Harsha et al. "Temperature-dependent optical properties of gold thinfilms", Optical Materials Express, 6(9), 2016; Reddy, Harsha et al. "Temperature-dependent optical properties of single crystalline and polycrystalline silver thin films", ACS Photonics, 4(5), 2017; Reddy, Harsha et al. "Temperature-dependent optical-properties of plasmonic titanium nitride thin films", ACS photonics, 4(6), 2017.

This chapter is organized as follows: The experimentally determined temperature evolution of the optical constants in Au, Ag and TiN thin films of varying thicknesses and crystallinities are presented. Simple physical pictures explaining the microscopic physical mechanisms governing the observed temperature dependencies will be provided. This is followed by a discussion on the numerical simulations that demonstrate the importance of incorporating the temperature induced deviations in order to model practical high temperature nanophotonic applications. Finally, the dispersion models capturing the high temperature dielectric functions of all the films will be presented.

3.1 Temperature dependent optical properties

The experimentally obtained complex dielectric permittivity of 200-nm thick polycrystalline (PC) gold film as a function of wavelength from room temperature to 500 °C for three consecutive heating cycles are shown in Figure 3.1. The imaginary part of the dielectric function ϵ_2 (Figure 3.1b, d & f) increases monotonically with increasing temperature for all heating cycles. However, for the first cycle the increase in ϵ_2 (Figure 3.1b) is not uniform, which is due to annealing effects and grain boundary movements at high temperatures [19]. The increase in ϵ_2 is more uniform for the subsequent cycles (Figure 3.1d & f). At longer wavelength ($\lambda > 900$ nm), where the

interband transitions are insignificant, the imaginary part at 500 °C becomes nearly twice as large as it is at room temperature. This behavior in ϵ_2 can be understood by noting that the scattering rates of the free electrons increase with increasing temperature due to an increase in electron-phonon interactions. The increased scattering rate in turn increases the Drude broadening Γ_D. As a result ϵ_2, which is proportional to Γ_D at longer wavelengths ($\epsilon_2 \approx \frac{\omega_p^2 \Gamma_D}{\omega^3}$), increases with increasing temperature.
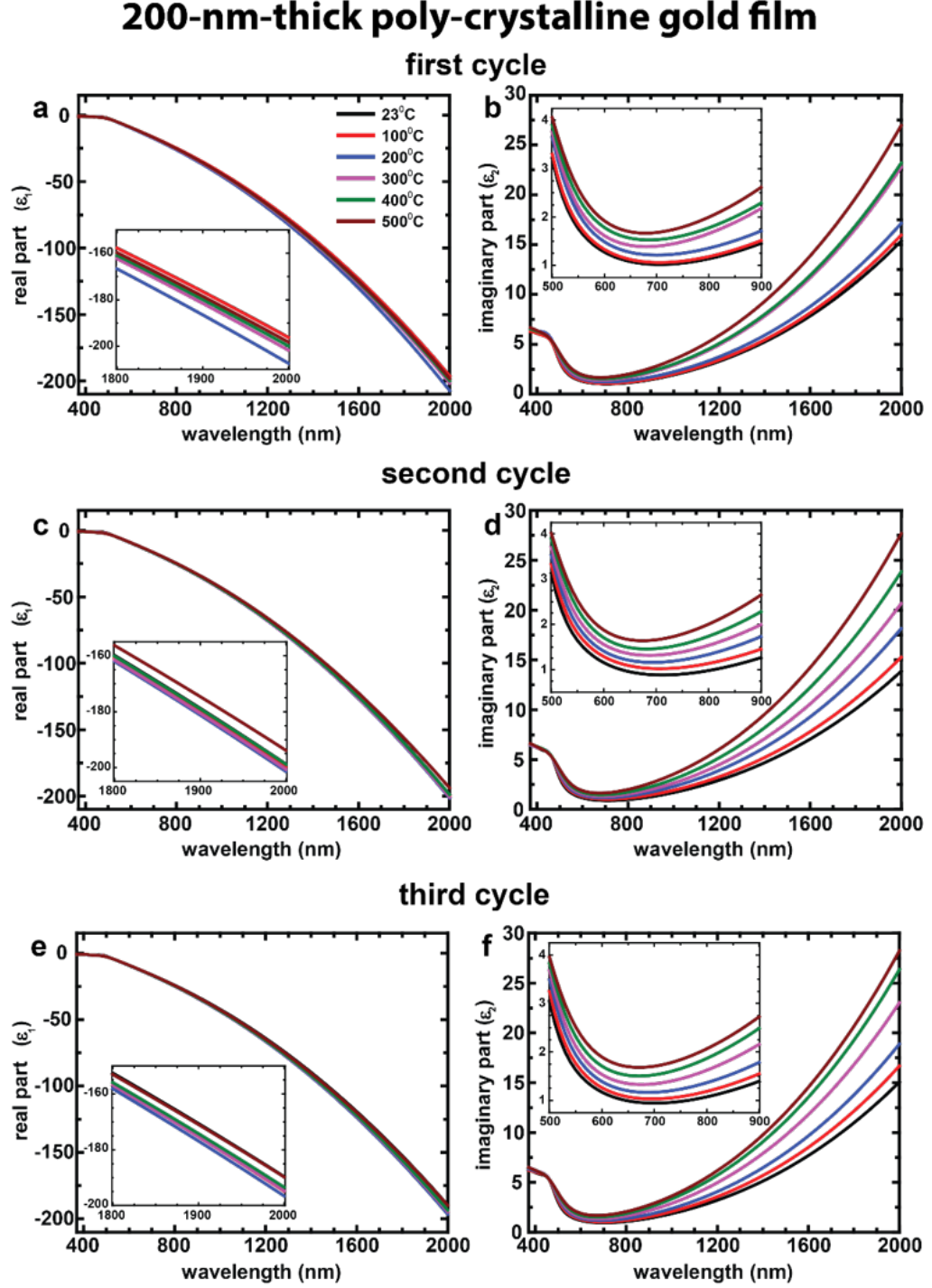
Fig. 3.1. Temperature dependent dielectric functions of thick poly-crystalline Au films for three subsequent heating cycles. (a, b), (c, d) and (e, f) show the real and imaginary parts of the complex dielectric functions of 200 nm-thick poly-crystalline gold film as a function of wavelength at various temperatures for first, second and third cycles, respectively. The imaginary part grows with increasing temperature while the real part only shows marginal changes with temperature.

Unlike the imaginary part, the real part of the dielectric permittivity ϵ_1 (Figure 3.1a, c & e) changes only marginally with increasing temperature and the trend in ϵ_1 is noticeable at longer wavelengths (insets of Figure 3.1). Initially, as the temperature is increased up to 200 °C, the real part grows in magnitude. Increasing the temperature further reduces the magnitude of the real part making the film less plasmonic. This trend is due to two counteracting mechanisms, namely decreasing carrier density and reducing electron effective mass, which will be discussed in detail later in the theory section. Figure 3.2 shows the room temperature data after each heating cycle. The first cycle improves the film quality by reducing both ϵ_1 and ϵ_2. But the subsequent cycles gradually degrade the sample properties, which is reflected in the increase in ϵ_2 (Figure 3.2b).
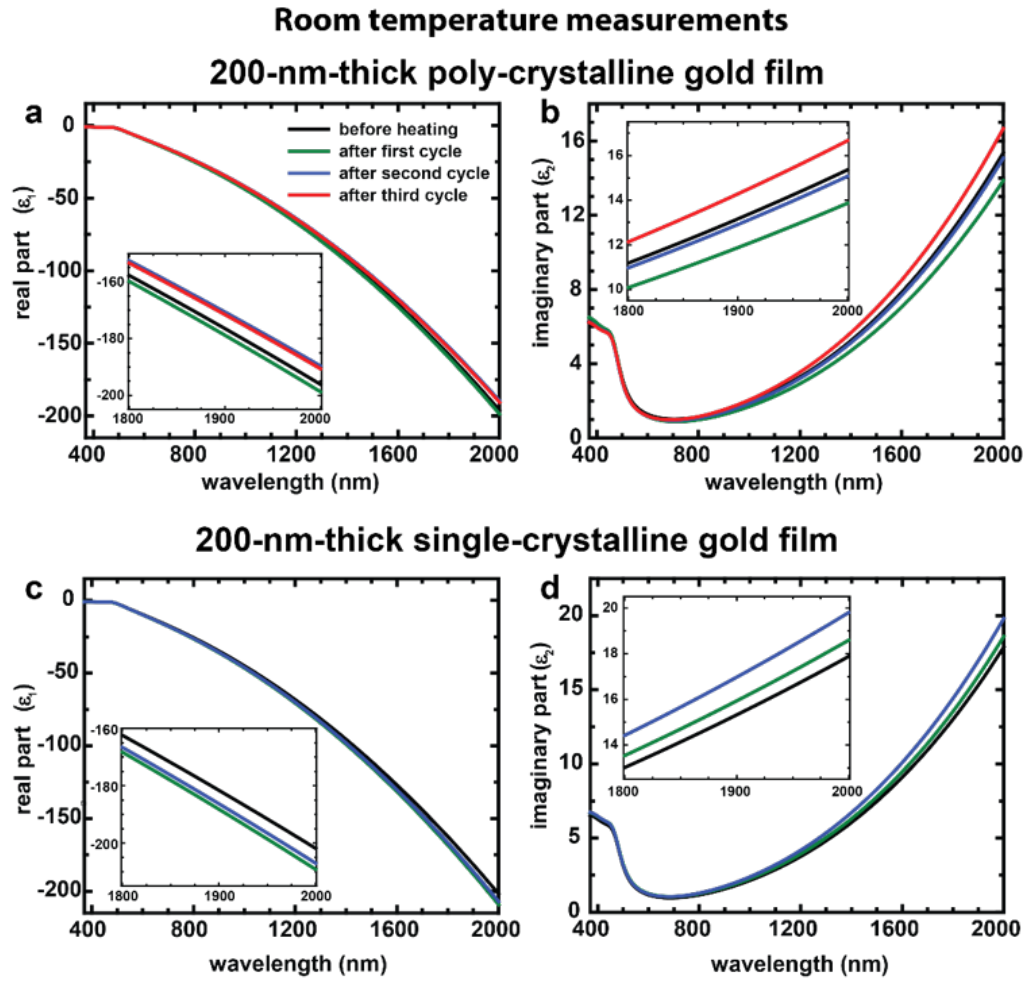
Fig. 3.2. Thick Au films' room temperature dielectric function comparison. (a) & (b) show the poly-crystalline film permittivity, while (c) & (d) show the single-crystalline film permittivity.
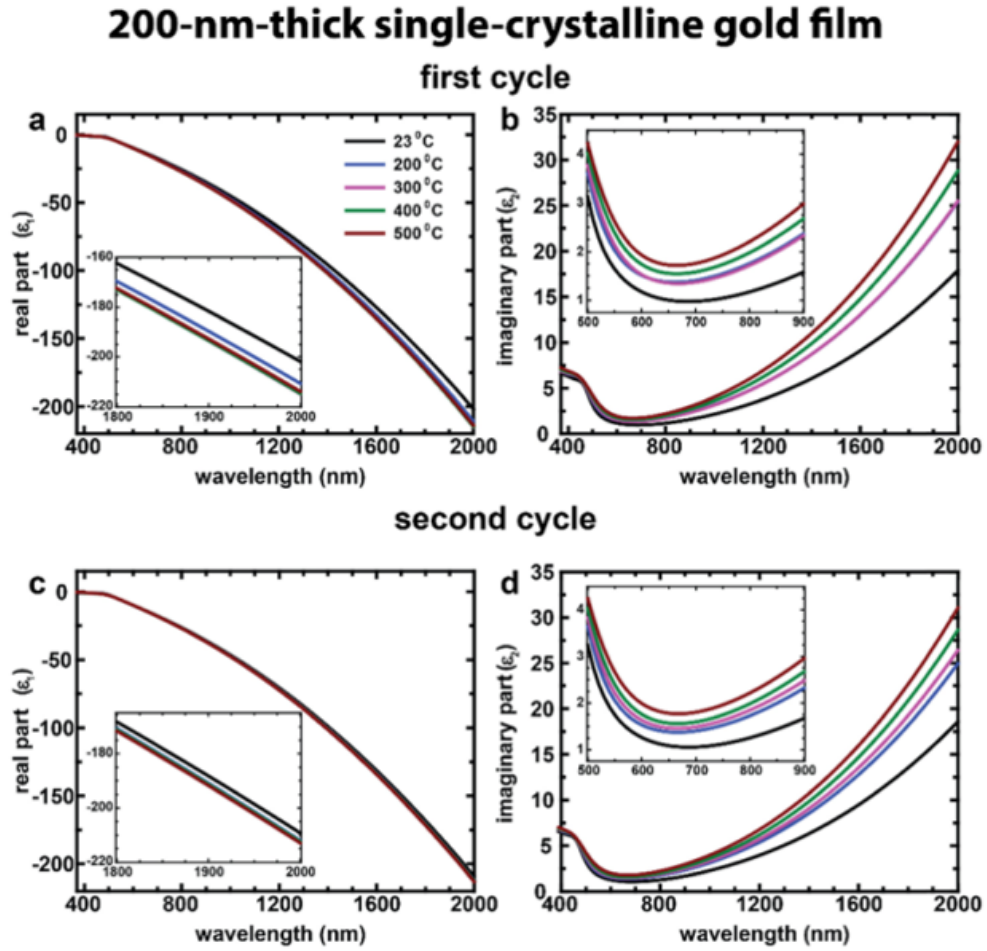
Fig. 3.3. Temperature evolution of dielectric function in thick SC film. (a) & (b) show the real and imaginary parts of the dielectric function, respectively, for the first cycle. Similarly, (c) and (d) are those from second heating cycle. The imaginary part grows monotonically with temperature, while the real part exhibits only marginal changes with temperature. Legend shows the color coding.
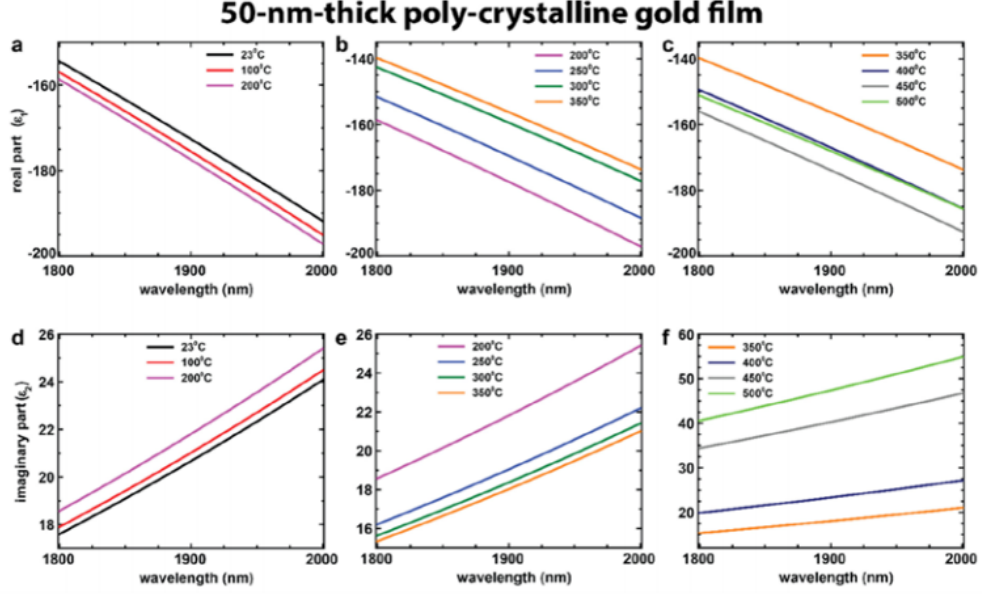
Fig. 3.4. Temperature dependent dielectric functions of 50 nm thick poly-crystalline film: (a), (b) and (c) show the real part and (d), (e) and (f) show the imaginary part of the complex dielectric functions for different temperature regions. Different colors correspond to dielectric functions at different temperatures (shown in the legend of each figure). To begin with, the imaginary part increases with temperature up to 200 °C (d). However, increasing the temperature beyond 200 °C leads to a decrease in the imaginary part, which continues till 350 °C (e). Raising the temperature further increases the imaginary part drastically, reducing the film quality substantially (f). The real part also displays increasing and decreasing behavior with temperature, depending on the temperature range.

Figure 3.3 shows results on thick single-crystalline (SC) film (200 nm thickness). The imaginary part of dielectric permittivity ϵ_2 increases monotonically with increasing temperature. At longer wavelengths ($\lambda > 900$ nm), close to two-fold increase in the imaginary part was observed upon heating to 500 °C. This trend can be attributed to the increased scattering rate picture as described above. Similar to PC films, ϵ_1 only changes marginally with temperature. The room temperature data of thick SC after multiple thermal cycles are shown in Figure 3.2. The imaginary part increases after each cycle, reducing the film quality.

Subsequently, we measured the temperature dependent dielectric function of 50-nm-thick PC film. We would like to point out that thin poly-crystalline films display losses higher than their bulk counterparts. This is predominantly due to grain boundary and surface defect scatterings that increase losses in thin films. At elevated temperatures we observed a different trend in the optical constants (Figure 3.4). Particularly, depending on the temperature range, the imaginary part can either increase or decrease, unlike thick films where a monotonic increase was observed. Based on the imaginary part behavior, we separate the temperature range into three regions: room temperature – 200 °C, 200 – 350 °C and 350 – 500 °C. For clarity of presentation only the data from 1800 - 2000 nm is shown in these plots. The DCP terms are given in Table 8, which can be used to extract the optical constants in the whole spectral range from 370 – 2000 nm. Initially, as the temperature is increased from room temperature to 200 °C ϵ_2 increases (Figure 3.4d). However, increasing the temperature over 200 °C results in a decrease in ϵ_2 (Figure 3.4e). For temperatures over 350 °C ϵ_2 increases again and the samples become extremely lossy (Figure 3.4f).
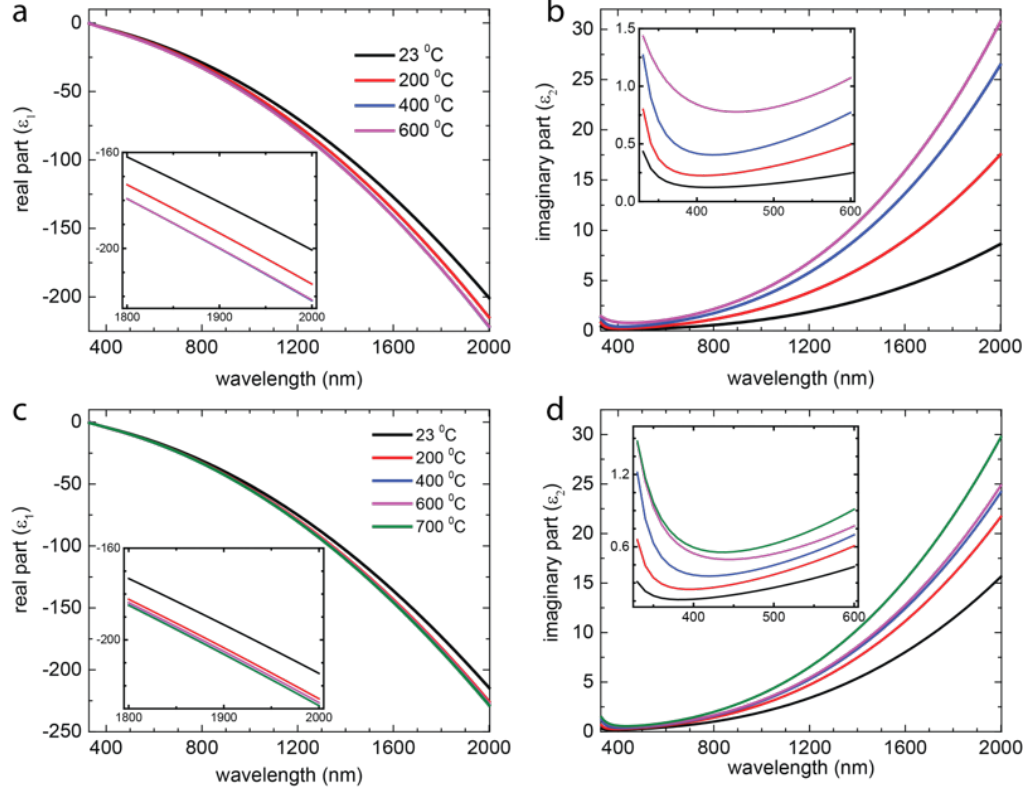
Fig. 3.5. Temperature dependent dielectric functions of 34 nm (a, b) and 450 nm (c, d) sputtered single-crystalline Ag films. Various colors correspond to different temperatures as shown in the legends. (a, c) Real and (b, d) imaginary parts of the complex dielectric functions for 34 and 450 nm thick films, respectively. The imaginary part grows with temperature, while the real part only varies marginally. Insets show the real and imaginary parts for selected wavelength ranges.

The temperature-dependent real and imaginary parts of the complex dielectric function of a 34 nm thick Ag film at selected temperatures, up to 600 ° C are shown in Figure 3.5a & b. With increasing temperature we observe significant deviations in the complex dielectric function compared to those from room temperature. These temperature-induced deviations are particularly evident at longer wavelengths ($\lambda >$ 900 nm), where the interband transitions are insignificant, and only the Drude terms contribute. At these wavelengths, ϵ_2 increases with temperature and eventually at 600 °C it becomes nearly four times larger than that at room temperature (Figure

3.5b). The observed increase in ϵ_2 is primarily due to increasing phonon number. Qualitatively, as the temperature is raised phonon number increases following Bose-Einstein statistics. This in turn increases the electron-phonon scattering, thereby elevating losses. As a result ϵ_2, which is proportional to the scattering rate also increases.
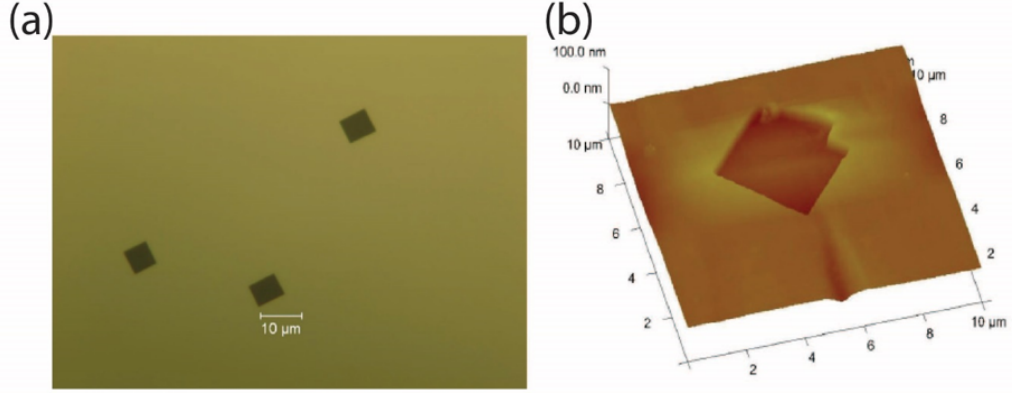
Fig. 3.6. (a) Optical image of 34 nm heat treated single-crystalline film. (b) AFM surface topograph of the same film. Depth profile analysis on the crack showed that the depth of the crack to be 32 nm, close the thickness of the Ag film.

The real part (ϵ_1), on the other hand, only changes marginally with temperature (Figure 3.5a). The small deviations in the real part can be understood by considering the temperature dependencies at longer wavelengths where interband transitions are insignificant (shown in the inset of Figure 3.5a). At these wavelengths, with increasing temperature the real part becomes more negative, making the films more metallic. The increase in metallicity can be attributed to the decrease in the electron effective mass, which in turn increases the plasma frequency thereby making the films more metallic. A detailed description of the physics associated with these temperature-induced deviations is given in the theory section below. Subsequent optical images taken on heat-treated samples revealed the formation of regular rectangular cracks (Figure 3.6a). Depth profile analysis from AFM measurements showed the depth of

the cracks to be quite close to the thickness of the film (Figure 3.6b). Such regular cracks are a good indication of a high degree of crystallinity in these films.

In Figure 3.5c & d we plot the temperature dependencies of ϵ_1 and ϵ_2 in a 450 nm thick SC Ag film from room temperature to 700 °C. Similar to thin SC Ag film, the imaginary part grows, while the real part reduces marginally with temperature. It should however be noted that the maximum increase in ϵ_2 at longer wavelengths is only a factor of 2, whereas in thin films nearly four-fold increase was observed. These temperature dependencies can be attributed to an increase in the electron-phonon interaction and the reduced effective mass as described above. Unlike thin films, no cracks were found in thick films upon heat treatment. Note that the maximum temperature of interest in thin SC films was 600 °C, whereas for thick samples we collected data upto 700 °C. This was because at temperatures over 600 °C thin SC films showed severe structural degradation with the cracks occupying a significant fraction of the film area (see Figure 3.6). As a result, it was no longer possible to reliably retrieve the dielectric function with a simple Drude-Lorentz model beyond breakdown temperature.
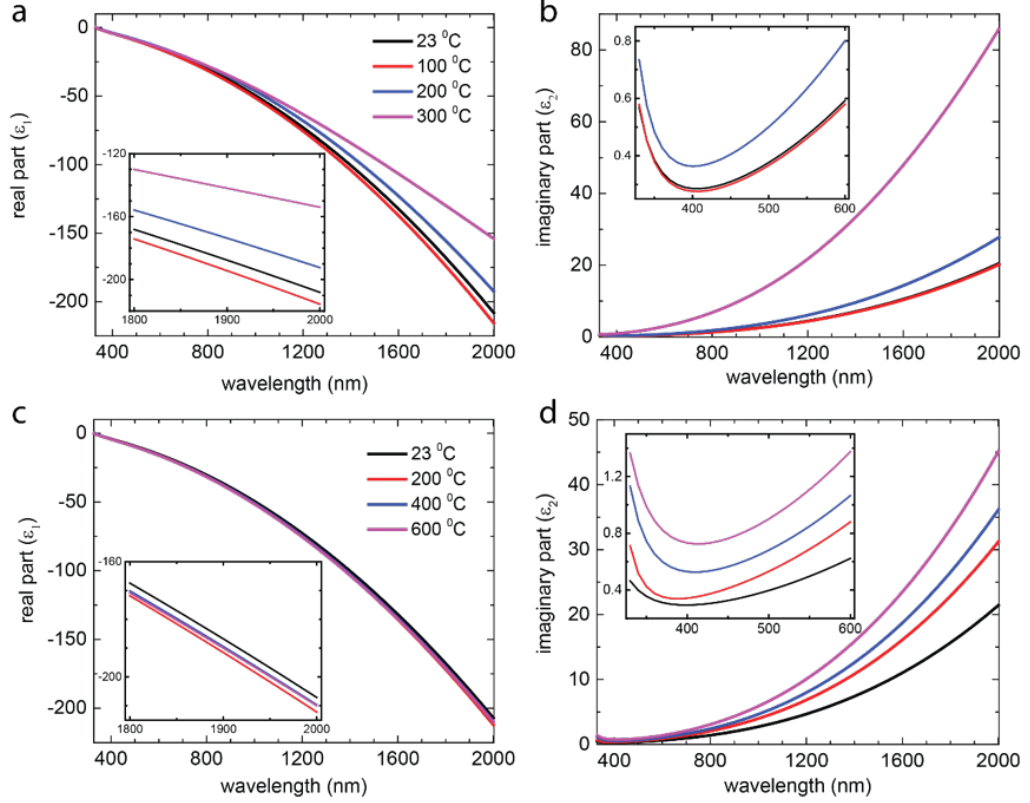
Fig. 3.7. Temperature evolution of dielectric function in 40 nm and 100 nm e-beam evaporated poly-crystalline Ag films. The real part is shown in (a) and (c), while the imaginary part is shown in (b) and (d). In 40 nm thick films, both the real and imaginary parts deviate substantially with temperature. For 100 nm thick films, the real part changes only marginally with temperature (c), while the imaginary part increases monotonically with temperature (d). The evolution for selected wavelength ranges are shown in insets.

Subsequently, we measured the temperature dependencies in PC Ag films. Due to smaller grain sizes in these films, the scattering rates and therefore the optical losses are expected to be larger than their SC counterparts. This is manifested in a larger imaginary part compared with their SC counterparts. Figure 3.7a & b shows the extracted temperature-dependent dielectric functions of 40 nm thick PC films. Initially, when the temperature is increased to 100 °C, the imaginary part reduces a bit (inset of Figure 3.7b). This is known to be due to grain merging in polycrystalline films

at slightly elevated temperatures, similar to what has been observed in Au. However, raising the temperature over 100 °C increases the imaginary part. Eventually, at 300 °C it increases by nearly four times compared to room temperature imaginary part. Significant deviations in ϵ_1 were also observed in these films (Figure 3.6a). The observed temperature dependencies in ϵ_1 are primarily due to the deviations in Drude broadening Γ_D but not because of plasma frequency. At even higher temperatures, we could no longer acquire reliable fits to our VASE measurements with a simple Drude-Lorentz oscillator model. Furthermore, the optical images on the heat-treated film showed features with strong contrast (Figure 3.8). The irregularities in the fits and the contrast in the optical images led us to suspect that the film may no longer be continuous after the heat treatment. This was subsequently verified from AFM topographs and depth profile analysis, which are shown in Figure 3.9. Several cracks could be seen in the film, revealing the structural degradation due to the heat treatment. In contrast to SC films, these cracks were completely irregular. Analytical models incorporating the changes in the surface morphology would be required to retrieve the optical responses beyond the breakdown temperatures [42, 43]. These studies are beyond the scope of the current work.
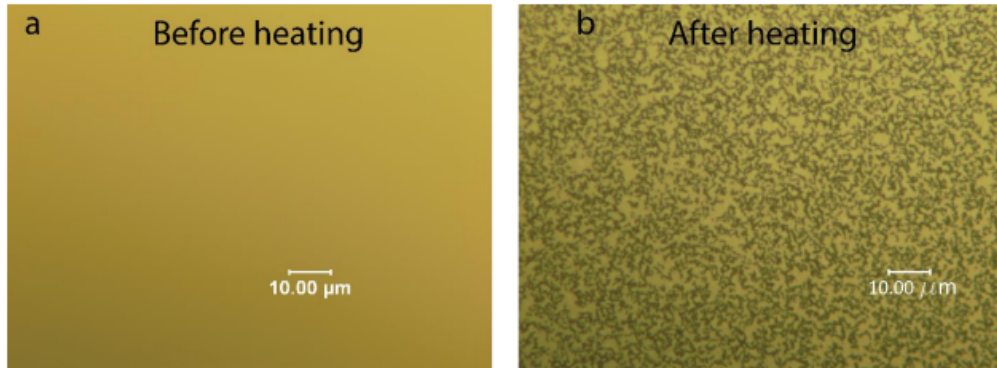
Fig. 3.8. Optical images of 40 nm poly-crystalline Ag films from before (a) and after heat treatment (b).
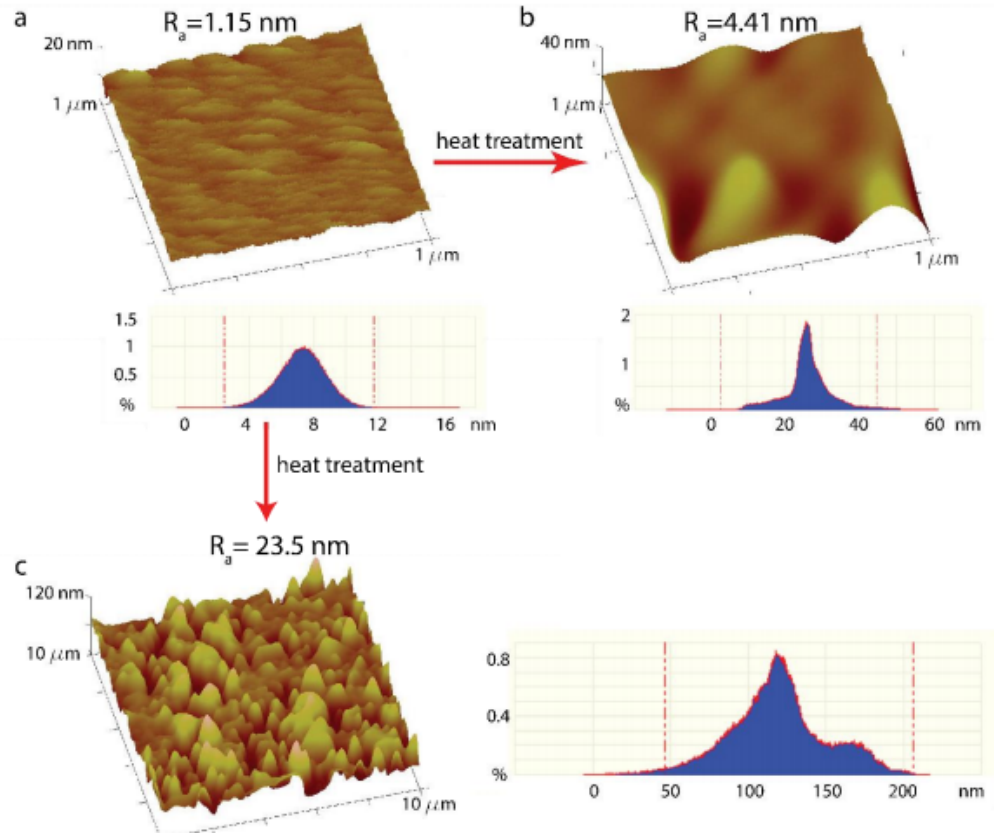
Fig. 3.9. AFM topographs and depth profile histograms on a poly-crystalline Ag film with 40 nm thickness from before (a) and after heat treatment (b, c).

The temperature-induced deviations in a 100 nm thick PC film are shown in Figure 3.7c & d. The real part only shows marginal changes with temperature, similar to thick SC films. This is because of small deviations in the plasma frequency and the fact that the Drude broadening is significantly smaller than the photon energies considered in this study (Table 14). On the other hand, the imaginary part increases by about two times upon heating the sample to 600 °C. At 700 °C, we could not get good fits, indicating that the film was no longer continuous. This was later confirmed from AFM topographs and optical images.
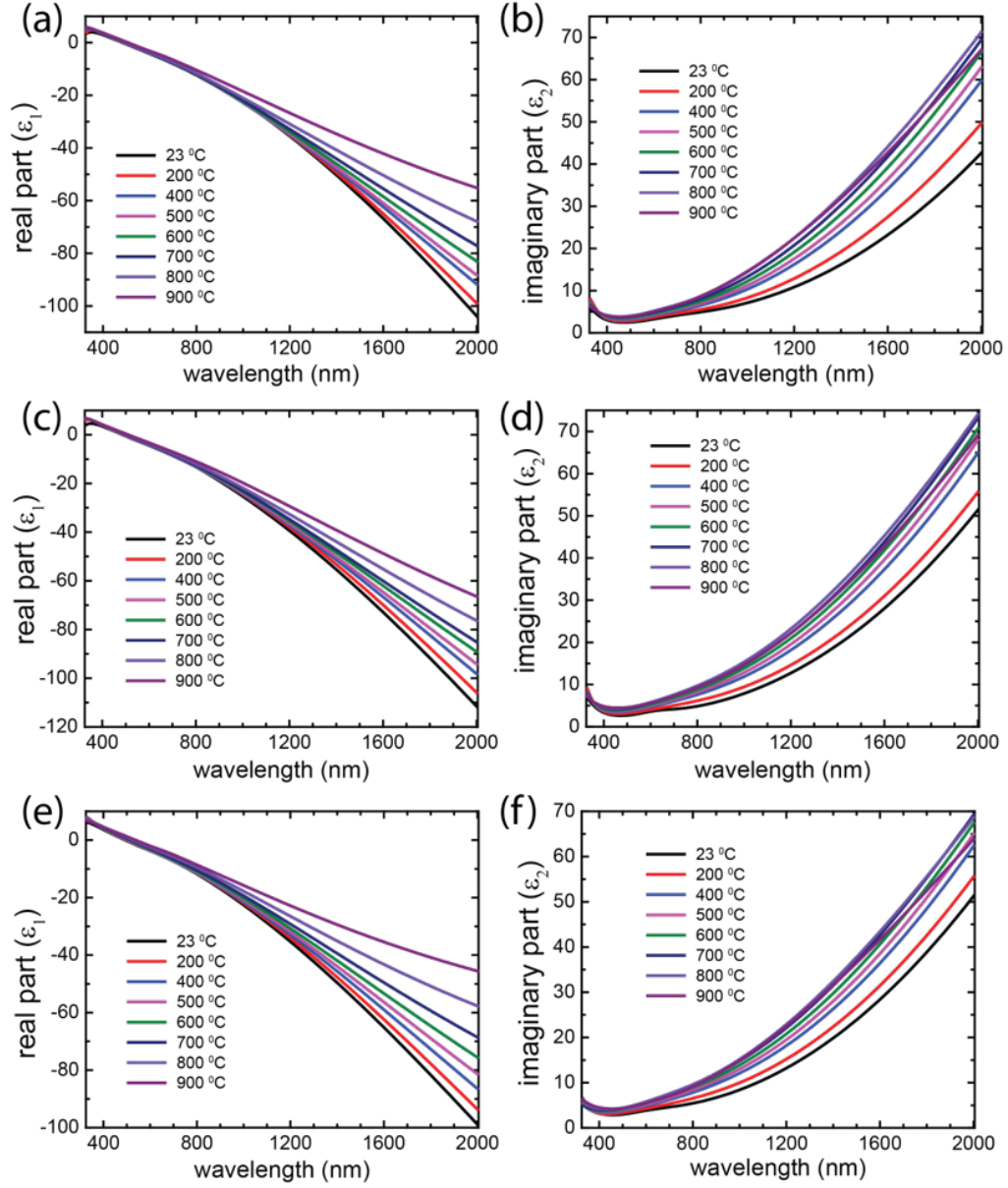
Fig. 3.10. Temperature-dependent dielectric functions of 200 nm (a, b), 50 nm (c, d), and 30 nm (e, f) TiN films. With increasing temperature, the real part decreases in magnitude, while the imaginary part increases up to 800 °C. Increasing the temperature even further reduces the imaginary part. The color coding is shown in the legends.

In Figure 3.10 we plot the experimentally extracted real and imaginary parts of the complex dielectric function of 200 nm, 50 nm and 30 nm TiN films at different temperatures, upto 900 °C. As the temperature is raised, both the real and imaginary parts show significant deviations from ambient temperature measurements. Particularly, the real part of all the films showed a monotonic decrease in magnitude (Figure 3.10a, c & e), reducing the metallicity. Contrary to the conventional understanding, the observed decrease in the magnitude of the real part is primarily because of the increase in the Drude broadening Γ_D, but not due to the decrease in the plasma frequency ω_p. In fact, ω_p marginally increases with temperature up to 800 °C (maximum deviation $< 6\%$, see Drude-Lorentz oscillator models in Tables 15-17). The observed temperature dependence in ϵ_1 can be understood from the Drude term, which captures the free electron response:

$$\hat{\epsilon}(\omega) = \epsilon_1 + i\epsilon_2 = \frac{\omega_p^2}{\omega^2 + i\Gamma_D\omega} \tag{3.1}$$

$$\text{where } \epsilon_1 = \frac{-\omega_p^2}{\omega^2 + \Gamma_D^2} \text{ and } \epsilon_2 = \frac{-\omega_p^2\Gamma_D}{\omega^3 + \Gamma_D^2\omega} \tag{3.2}$$

when $\Gamma_D \ll \omega$, which is the case with noble metals close to ambient temperatures, the real part can be approximated as $\epsilon_1 \approx \frac{-\omega_p^2}{\omega^2}$, independent of Γ_D. This approximation is no longer valid when Γ_D is comparable to ω. For TiN films, Γ_D varies from 0.2 - 0.75 eV, depending on the temperature and film thickness (Tables 15-17). For the photon energy ranges considered in the current study, particularly at near-IR wavelengths, the above approximation is no longer valid. From the exact expression of ϵ_1 in Eq. 3.2 it is clear that an increase in Γ_D leads to a decrease in the magnitude of ϵ_1, which is what we observed in all TiN films.

The imaginary part at longer wavelengths, on the other hand, increases with temperature up to 800 °C (Figure 3.10b, d & f). Increasing the temperature even further leads to a decrease in ϵ_2. The observed deviations in the imaginary part are due to the increase in Γ_D and the non-monotonic behavior of ω_p. As pointed out earlier, Γ_D increases monotonically with temperature. The plasma frequency on
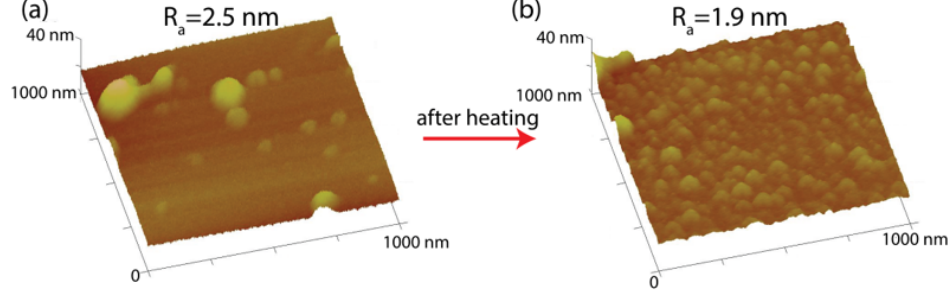
Fig. 3.11. AFM topogrphs on 50 nm TiN film. Topographs (a) and (b) correspond to before and after heat treatment, respectively.

the other hand, deviates marginally with temperature, increasing until 800 °C and decreasing when the temperature is raised to 900 °C (see Tables 15-17). As a result, the numerator in the Drude expression of ϵ_2 in Eq. 3.2, $\omega_p^2 \Gamma_D$, increases monotonically, increasing the imaginary part. At the same time, the denominator $\omega^3 + \Gamma_D^2 \omega$, increases quadratically with Γ_D, counteracting the increase in the numerator. Based on the experimental evidence, we conclude that the increase in $\omega_p^2 \Gamma_D$ dominates until 800 °C. However, at 900 °C, the quadratic dependence of the denominator on Γ_D, along with the marginal decrease in ω_p, contribute to the observed decrease in the imaginary part.

We would like to point out a couple of key differences between the evolution of optical properties in TiN compared to noble metals, Au and Ag. In thin Au and Ag films, both ϵ_1 and ϵ_2 showed significantly larger deviations with temperature compared to their thicker counterparts (nearly 4-fold increase in ϵ_2 and 30% decrease in the magnitude of ϵ_1 in thin films compared to a 2-fold increase in ϵ_2 and 10-15% decrease in the magnitude of ϵ_1 in thick films). In contrast to noble metals, the temperature evolution of the dielectric function in TiN is nearly independent of the thickness. Furthermore, thin Au and Ag PC (SC) films showed severe structural and surface morphological degradation upon heating to temperatures close to 400 °C (600 °C). However, the microstructure of TiN films remained intact, even though

the samples were heated to higher temperatures (AFM topographs of 50 nm TiN are shown in Figure 3.11).

We estimated the plasmonic performance of Au, Ag and TiN at high temperatures using quality factors, plasmonic performance metrics, of both localized and propagating plasmons. For localized surface plasmons, the strength of the local electric field enhancement in a spherical nanoparticle, under quasi static assumption, is given by $Q_{LSPR} = -\epsilon_1/\epsilon_2$ [17]. Whereas for propagating plasmons, the decay length of surface plasmon polaritons (L_{SPP}), serves as a figure of metric for waveguiding applications [44]. In Figure 3.12 we plot the quality factors of the localized surface plasmon resonances and the propagation lengths of surface plasmon resonances, computed using the temperature-dependent dielectric functions of 30 nm PC Au, 40 nm PC Ag and 30 nm SC TiN, at various temperatures. From Figure 3.12a it is clear that although TiN has field enhancement and surface plasmon polaritons (SPP) propagation quality factors inferior to noble metals at room temperature, the difference between the performance metrics reduces substantially and the quality factors in TiN approach those in Au and Ag at temperatures over 400 °C. Table 1 (Table 2) shows a comparison of Q_{LSPR} (SPP propagation lengths) in TiN, Au, and Ag at different temperatures and a wavelength of 1550 nm.
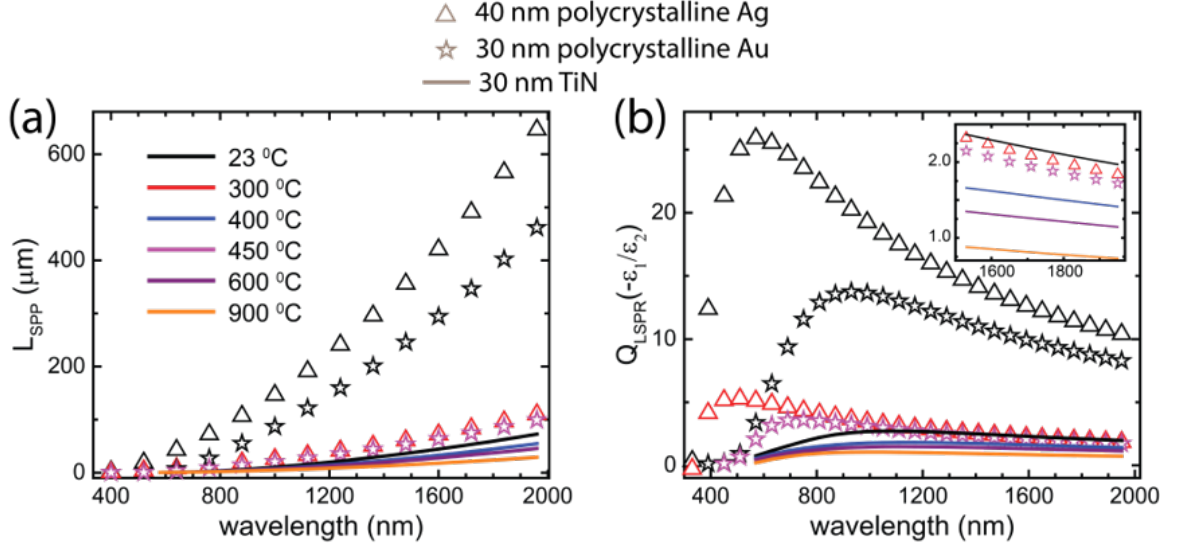
Fig. 3.12. Comparison of Au, Ag, and TiN plasmonic performance at high temperatures. SPP propagation lengths (a) and Q_{LSPR} (b) of 40 nm Ag (open triangles), 30 nm Au (open stars), and 30 nm TiN (solid lines) at different temperatures. Legend in (a) shows the temperature color coding for both the plots. The Q_{LSPR} at longer wavelengths are shown in the inset of (b).

Table 1: Computed quality factors of localized surface plasmon resonances in Au, Ag and TiN at various temperatures and a wavelength of 1550 nm.

Sample type	Q_{LSPR} at 23 °C	Q_{LSPR} at 300 °C	Q_{LSPR} at 400 °C	Q_{LSPR} at 450 °C	Q_{LSPR} at 600 °C	Q_{LSPR} at 900 °C	% change at the largest temperature
30 nm PC Au	10.2	10.2	4.9	2.1	-	-	79.4
40 nm PC Ag	12.9	2.3	-	-	-	-	82.2
30 nm TiN	2.3	-	1.6	-	1.3	0.87	62.2
50 nm TiN	2.7	-	1.8	-	1.5	1.2	55.5
200 nm TiN	2.9	-	1.9	-	1.5	1.01	65.2

Table 2: Computed propagation lengths of SPPs in Au, Ag and TiN at various temperatures and a wavelength of 1550 nm.

Sample type	L_{SPP} in μm at 23 ^{0}C	L_{SPP} in μm at 300 ^{0}C	L_{SPP} in μm at 400 ^{0}C	L_{SPP} in μm at 450 ^{0}C	L_{SPP} in μm at 600 ^{0}C	L_{SPP} in μm at 900 ^{0}C	% change at the largest temperature
30 nm PC Au	273	265	136	59	-	-	78.4
40 nm PC Ag	393	67	-	-	-	-	82.9
30 nm TiN	41	-	30	-	25	17	58.5
50 nm TiN	55	-	36	-	31	23	58.2
200 nm TiN	50	-	34	-	29	20	60

3.2 Numerical simulations

We use numerical simulations to demonstrate the practical importance of our findings for important high-temperature applications. We consider two designs 1) an Ag nanoantenna as a near-field transducer (NFT) design for heat assisted magnetic recording (HAMR) and 2) the role of temperature induced deviations in generating nanoscale thermal hot-spots in a diabolo antenna. In HAMR the nanoantennas are excited with lasers at their resonance frequencies, which leads to intense electromagnetic fields in the near field of the plasmonic nanoantennas—hotspots. It was proposed and later experimentally demonstrated that these hot spots could reduce the coercivity of the magnetic medium locally when the NFTs are brought into close proximity to the recording medium [5–7]. The reduced coercivity then allows for writing/recording information locally onto the magnetic medium using a nearby magnetic head. Although this is a promising approach, it suffers from a serious drawback. The strong absorption of laser light leads to significant heating of plasmonic nanoantenna. It has been estimated that the internal heating would lead to temperatures close to 400 °C. Here, we show that the temperature-induced changes to the dielectric function lead to significant modifications to the field profile, which should be taken into account to have an accurate estimation of the field enhancement. Furthermore, the larger breakdown temperatures of the single crystalline films make them better candidates for HAMR applications.
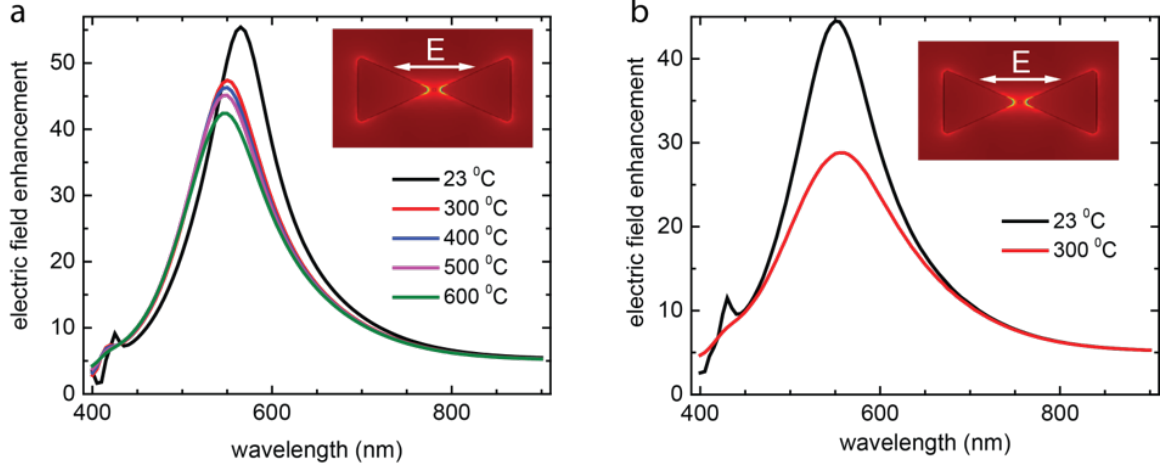
Fig. 3.13. Computed field enhancement in the gap between the bow-tie nanoantennas at room temperature and elevated temperatures using the temperature-dependent dielectric function of 34 nm single-crystalline (a) and 40 nm poly-crystalline (b) Ag films. Incident field polarization was along bow-tie axis. Field enhancement reduces with temperature.

We performed field profile simulation in the gap between the bowtie antennas on MgO (refractive index = 1.73), a near-field transducer design, using a commercial FEM solver (COMSOL Multiphysics). The extracted optical properties from the temperature dependent VASE measurements were used as the material properties for our simulations. Figure 3.13 shows the simulated average electric field in a small volume (64 nm^3) in the gap between the two nanoantennae at different temperatures computed using the optical properties of thin SC and PC Ag films. Insets show the polarization of incident electric field and the generated hot spots. It should be noted that the field enhancement is larger in the SC case due to lower losses. At 300 °C, the maximum field enhancement in SC and PC cases reduces by nearly 17% and 50%, respectively. These findings illustrate a couple of important points: 1) Incorporating the temperature-dependent optical properties in modeling high-temperature applications leads to significantly different results versus those obtained with the room temperature data; 2) For NFTs, as the field enhancement reduces at elevated temperatures, one would have to increase laser pumping to even higher intensities to

achieve the same enhancement, which would increase the temperature even further; 3) The relative changes in the electric field enhancement in SC case are smaller compared to the PC case. As a result, together with their larger thermal stability, SC films can play a major role in applications requiring moderate elevation temperatures such as spasers, biosensors, along with NFTs.

Absorption and losses in metals have long been considered to be detrimental to plasmonic performance. However, in the emerging field of thermos-plasmonics, the goal is to take advantage of the strong optical absorption in plasmonic nanostructures and generate nanoscale thermal sources [45–47]. These nanoscale thermal sources are of great interest in a wide variety of applications such as cancer therapy, photothermal imaging, nanochemistry, and opto/plasmo fluidics [45]. By engineering the geometries of nanoantennas, temperatures as high as 800 °C can be generated locally in plasmonic components (with continuous wave excitation), while keeping the background/substrate close to room temperature. Such intense nanoscale heat sources can be of great use in chemical reactions requiring high temperatures, such as ammonia synthesis, methane oxidation, and other heterogeneous chemical reactions, alleviating the need for bulky experimental setups operating at very high temperatures [48].

Here we show that incorporating the temperature-induced deviations would lead to significantly different opto-thermal responses in plasmonic heat sources [47]. We performed a couple opto-thermal finite-element method (FEM) based multiphysics simulation of heating in diabolo antenna (DA) arrays, induced by external optical excitation. We numerically considered three different cases of DA arrays on 0.5 mm thick sapphire substrate: made of gold, silver, and TiN, with optical resonances at 1.14, 1.16, and 1.3 μm, respectively. Dimensions of the unit cell are shown in Figure 3.14a. We use a Gaussian profile illumination with power P_{in}, and a full width at half-maximum of 19.5 μm at the resonance wavelength exciting 936 antennas.

Heat generation in plasmonic structures is governed by Joule heating, with the strength of the heat source determined by the dissipated electromagnetic power density inside the nanoparticle. The spatial heat source density is determined by the

distribution of the local electromagnetic field inside the plasmonic DA and the imaginary part of the dielectric function as

$$q(r,T) = \epsilon_\circ \omega \text{Img}(\epsilon(T))|\mathbf{E}(r)|^2 \qquad (3.3)$$

where $\epsilon_\circ$, ω and $\mathbf{E}(r)$ are the permittivity of free space, frequency of the incident photons and the local electric field, respectively, while $\epsilon(T)$ is the temperature-dependent dielectric function of the metal. The dissipated energy is determined by both the distribution of the local electric field inside the plasmonic DA, as well as the imaginary part of the complex dielectric function. Since the imaginary part has a strong dependence on temperature, estimating the temperature rise in DA requires a recursive calculation that takes into account the temperature dependence of ϵ.
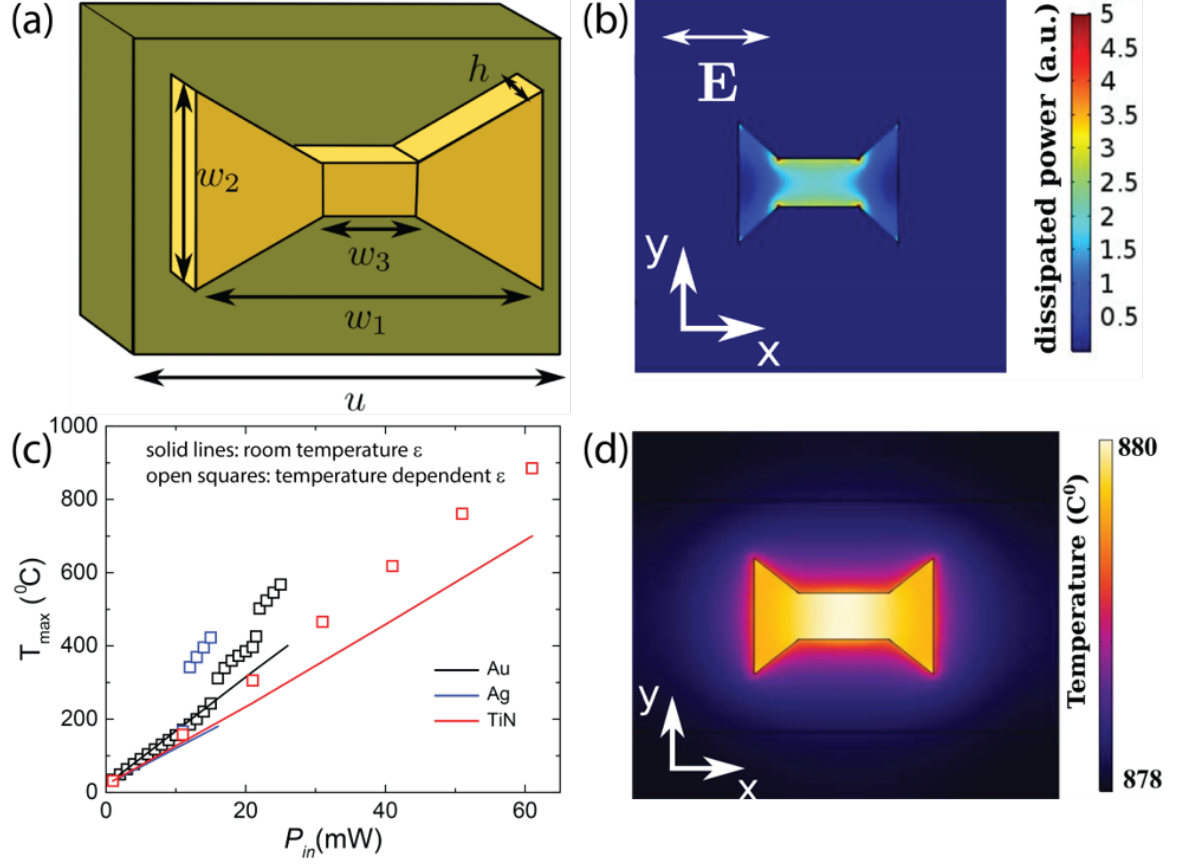
Fig. 3.14. Opto-thermal response of a diabolo antenna. (a) Diabolo unit cell u=500 nm, w_1=235 nm, w_2=150 nm, w_3=100 nm, and h=50 nm. (b) Typical spatial distribution of dissipated power in a diabolo antenna for polarization along x. (c) Maximum temperature on the diabolo surface as a function of input power in Au, Ag, and TiN. Solid lines correspond to the temperature rise with room temperature dielectric function, while open squares correspond to the temperature rise when the temperature dependencies are included into FEM models. (d) Spatial profile of temperature in a TiN diabolo antenna, computed using the temperature deviations with 61 mW input power. The temperature profile is nearly uniform across the nanoantenna, unlike the strongly localized electric field.

We performed these calculations using the experiment fitted temperature-dependent dielectric functions of 30 nm Au, 40 nm Ag and 30 nm TiN films. The coupled opto-thermal simulations were performed using a commercial finite element method based solver (COMSOL Multiphysics). A typical spatial distribution of the dissipated power

density in a DA at resonance condition is shown in Figure 3.14b. In Figure 3.14c we plot the dependence of the maximum temperature on the surface of the DA as a function of the input power P_{in}, which was computed using the temperature-induced deviations. For a comparison, the expected temperature rise using the room temperature imaginary part is also plotted. These findings unambiguously show that incorporating the temperature dependencies lead to higher temperatures in the plasmonic thermal sources, particularly for high input powers. For instance, at the maximum incident powers considered here, nearly 41, 145, and 27% increase in the maximum temperature is expected in Au, Ag and TiN, respectively. We would like to emphasize that despite pumping at higher powers the TiN-based DA has a more stable response due to its refractory nature, exhibiting smaller relative changes in the maximum temperature, compared to Au and Ag. Figure 3.14d shows the computed temperature field in TiN DA when excited with 61 mW input power. Because of high thermal conductivity, the temperature is nearly uniform across the surface of the diabolo antenna.

3.3   Theory

In this section, we discuss the theoretically expected temperature dependencies in the plasma frequency and Drude damping and compare them with our experimental findings. At longer wavelengths, where inter-band transitions become insignificant, the observed temperature dependencies in the optical constants are due to the two Drude terms: Plasma frequency ω_p and the Drude damping Γ_D. The temperature dependencies of these two terms are primarily due to the following factors: 1) the decrease in the carrier density due to volume expansion, 2) decrease in the effective mass of the free electrons in the metal and 3) increase in the electron-phonon interaction with temperature. The plasma frequency ω_p is dependent on the carrier density (N) and the effective mass (m*) of electrons according to the relation:

$$\omega_p^2 = \frac{Ne^2}{m^*\epsilon_\circ} \tag{3.4}$$

The carrier density N reduces with increase in the temperature due to volume thermal expansion as

$$N = \frac{N_o}{\sqrt{1 + \gamma(T - T_\circ)}} \tag{3.5}$$

where γ is the volume thermal expansion coefficient. On the other hand, the effective mass m* in metals has been reported to decrease with increasing temperature [49]. The decrease in m* increases the plasma frequency whereas the decrease in N counteracts it. The interplay between these two mechanisms dictates the observed behavior in the plasma frequency. The temperature dependence of ω_p for thick PC (SC) Au film is shown in Figure 3.15a (3.15c). The error bars in the plots show the 90% confidence limits obtained from the fits. Based on these experimental findings we conclude that the decrease in m* (increase in the plasma frequency) is the dominant mechanism compared to the change in N (reducing the plasma frequency). A similar decrease in the plasma frequency up to 200 °C was observed in thin films (Tables 1-9). On the other hand, for thick SC film the plasma frequency monotonically increases indicating that the decrease in effective mass is the dominant mechanism throughout the measured temperature range (Figure 3.15c).

The Drude damping $\Gamma_D = \hbar/\tau_D$ depends on the electron-electron (Γ_{ee}) and electron-phonon ($\Gamma_{e\phi}$) scattering mechanisms

$$\Gamma_D = \Gamma_{ee} + \Gamma_{e\phi} \tag{3.6}$$

$$\frac{1}{\tau_D} = \frac{1}{\tau_{ee}} + \frac{1}{\tau_{e\phi}} \tag{3.7}$$

where $\frac{1}{\tau_{ee}}$ and $\frac{1}{\tau_{e\phi}}$ are given by [50–53]:

$$\frac{1}{\tau_{ee}} = \frac{1}{12}\pi^3 \Gamma \Delta \left(\frac{1}{\hbar E_F}\right) \left[(K_B T)^2 + \left(\frac{\hbar\omega}{2\pi}\right)^2\right] \tag{3.8}$$
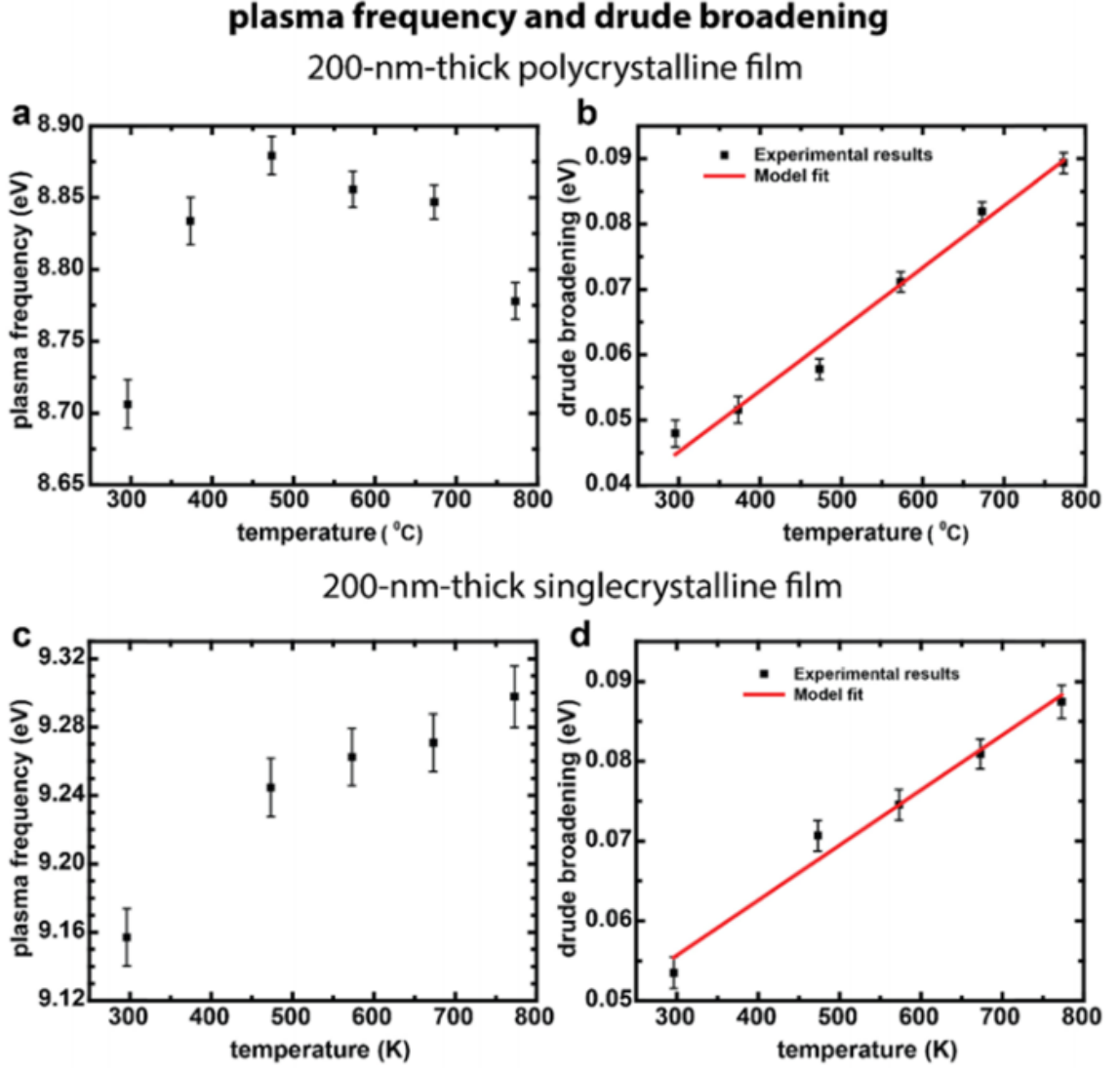
Fig. 3.15. Plasma frequency and Drude broadening of 200-nm-thick poly (a, b) and single-crystalline (c, d) films. Depending on the temperature range the plasma frequency either increases or decrease in poly-crystalline film, while grows monotonically in single-crystalline film. On the other hand, Drude broadening increases monotonically with increasing temperature for both films. The red curve is the fit using Eq. 3.10.

$$\frac{1}{\tau_{e\phi}} = \frac{1}{\tau_\circ}\left[\frac{2}{5} + 4\left(\frac{T}{\theta}\right)^5 \int_0^{\theta/T} \frac{z^4}{e^z - 1}dz\right] \tag{3.9}$$

Here $\Gamma, \Delta, \mathrm{E}_F, \theta$ and $\tau_\circ$ are the average scattering probability over the Fermi surface, the fractional Umklapp scattering, the Fermi energy of free electrons, Debye temperature and a material dependent constant, respectively.

The Debye temperature of gold is 170 K. So θ/T, the upper limit of the integral in Eq. 3.9 is <1 for the entire temperature range considered in this work. Hence the exponential in the denominator of the integrand can be approximated using Taylor's series as $e^z = 1+z$. This simplifies the above expression on electron-phonon scattering as:

$$\frac{1}{\tau_{e\phi}} = \frac{1}{\tau_\circ}\left[\frac{2}{5} + \frac{T}{\theta}\right] \tag{3.10}$$

Although the electron-electron scattering has a quadratic dependence on temperature, its contribution due to the temperature dependent term is weak compared to the frequency dependent term at the optical frequencies. However, a frequency independent Γ_D (hence a frequency independent scattering rate) is widely used in modeling the optical constants of metal films. We therefore treat the contribution due to electron-electron scattering as independent of both temperature and frequency and obtain good fits for the Drude broadening. These results for the thick PC (SC) Au films are shown in Figure 3.15b (3.15d).

3.4 Dispersion models

3.4.1 Temperature-dependent Drude-Critical Point Models for Au thin films

The following form of Drude and 2 critical Point (DCP) model was used to fit the VASE data for Au samples:

$$\hat{\epsilon}(\omega) = \epsilon_\infty - \frac{\omega_p^2}{\omega^2 + i\Gamma_D\omega} + \sum_{j=1}^{2} C_j\omega_j \left(\frac{e^{i\phi_j}}{\omega_j - \omega - i\gamma_j} + \frac{e^{-i\phi_j}}{\omega_j + \omega + i\gamma_j}\right)$$

The experimentally determined temperature dependent coefficients of the DCP model for Au films of different thicknesses are shown below:

Table 3: 200-nm-thick poly-crystalline gold film, first heating cycle.

T	ϵ_∞	ω_p (eV)	Γ_D (eV)	C_1	ϕ_1	γ_1 (eV)	$\hbar\omega_1$ (eV)	C_2	ϕ_2	γ_2 (eV)	$\hbar\omega_2$ (eV)	MSE
23 °C	2.27	8.856	0.0471	2.31	$-\pi/4$	1.215	3.082	0.226	$-\pi/4$	0.256	2.625	1.19
100 °C	2.45	8.863	0.0489	2.28	$-\pi/4$	1.198	3.060	0.224	$-\pi/4$	0.273	2.620	1.04
200 °C	2.04	9.113	0.0496	2.64	$-\pi/4$	1.464	3.270	0.395	$-\pi/4$	0.359	2.631	0.93
300 °C	2.06	9.012	0.0678	2.49	$-\pi/4$	1.357	3.218	0.371	$-\pi/4$	0.375	2.607	1.09
400 °C	2.03	8.978	0.0695	2.56	$-\pi/4$	1.407	3.208	0.375	$-\pi/4$	0.398	2.599	0.98
500 °C	1.90	8.959	0.0815	2.54	$-\pi/4$	1.369	3.209	0.394	$-\pi/4$	0.429	2.578	0.86

Table 4: 200-nm-thick poly-crystalline gold film, second heating cycle.

T	ϵ_∞	ω_p (eV)	Γ_D (eV)	C_1	ϕ_1	γ_1 (eV)	$\hbar\omega_1$ (eV)	C_2	ϕ_2	γ_2 (eV)	$\hbar\omega_2$ (eV)	MSE
23 °C	2.33	8.909	0.0421	2.32	$-\pi/4$	1.160	3.080	0.206	$-\pi/4$	0.235	2.620	1.41
100 °C	2.24	8.940	0.0460	2.41	$-\pi/4$	1.250	3.124	0.254	$-\pi/4$	0.277	2.622	1.35
200 °C	2.23	8.985	0.0542	2.41	$-\pi/4$	1.313	3.171	0.259	$-\pi/4$	0.332	2.619	1.35
300 °C	2.04	8.980	0.0618	2.50	$-\pi/4$	1.365	3.211	0.356	$-\pi/4$	0.362	2.608	1.10
400 °C	1.93	8.954	0.0720	2.47	$-\pi/4$	1.353	3.213	0.392	$-\pi/4$	0.403	2.592	1.24
500 °C	1.66	8.865	0.0857	2.50	$-\pi/4$	1.359	3.233	0.405	$-\pi/4$	0.432	2.572	0.99

Table 5: 200-nm-thick poly-crystalline gold film, third heating cycle.

T	ϵ_∞	ω_p (eV)	Γ_D (eV)	C_1	ϕ_1	γ_1 (eV)	$\hbar\omega_1$ (eV)	C_2	ϕ_2	γ_2 (eV)	$\hbar\omega_2$ (eV)	MSE
23 ^{0}C	1.99	8.706	0.0479	2.27	$-\pi/4$	1.205	3.110	0.225	$-\pi/4$	0.250	2.628	1.51
100 ^{0}C	2.41	8.834	0.0515	2.22	$-\pi/4$	1.205	3.085	0.251	$-\pi/4$	0.281	2.622	1.34
200 ^{0}C	2.08	8.879	0.0578	2.36	$-\pi/4$	1.307	3.175	0.324	$-\pi/4$	0.332	2.615	0.96
300 ^{0}C	1.83	8.856	0.0711	2.39	$-\pi/4$	1.301	3.194	0.349	$-\pi/4$	0.361	2.601	1.08
400 ^{0}C	1.85	8.847	0.0819	2.38	$-\pi/4$	1.320	3.203	0.377	$-\pi/4$	0.398	2.590	0.98
500 ^{0}C	1.59	8.778	0.0893	2.48	$-\pi/4$	1.368	3.221	0.381	$-\pi/4$	0.423	2.577	0.90

Table 6: 200-nm-thick single-crystalline gold film, first heating cycle.

T	ϵ_∞	ω_p (eV)	Γ_D (eV)	C_1	ϕ_1	γ_1 (eV)	$\hbar\omega_1$ (eV)	C_2	ϕ_2	γ_2 (eV)	$\hbar\omega_2$ (eV)	MSE
23 ^{0}C	2.64	8.991	0.0534	2.22	$-\pi/4$	1.105	3.062	0.206	$-\pi/4$	0.235	2.618	1.41
200 ^{0}C	2.27	9.218	0.0725	2.57	$-\pi/4$	1.337	3.258	0.371	$-\pi/4$	0.334	2.629	1.00
300 ^{0}C	2.52	9.310	0.0712	2.45	$-\pi/4$	1.337	3.277	0.465	$-\pi/4$	0.391	2.623	0.96
400 ^{0}C	2.13	9.324	0.0805	2.63	$-\pi/4$	1.405	3.352	0.517	$-\pi/4$	0.426	2.612	0.93
500 ^{0}C	1.79	9.323	0.0898	2.73	$-\pi/4$	1.425	3.400	0.579	$-\pi/4$	0.469	2.602	0.91

Table 7: 200-nm-thick single-crystalline gold film, second heating cycle.

T	ϵ_∞	ω_p (eV)	Γ_D (eV)	C_1	ϕ_1	γ_1 (eV)	$\hbar\omega_1$ (eV)	C_2	ϕ_2	γ_2 (eV)	$\hbar\omega_2$ (eV)	MSE
23 ^{0}C	2.82	9.157	0.0535	2.34	$-\pi/4$	1.144	3.079	0.224	$-\pi/4$	0.246	2.626	1.40
200 ^{0}C	2.33	9.245	0.0707	2.61	$-\pi/4$	1.284	3.210	0.319	$-\pi/4$	0.312	2.621	0.95
300 ^{0}C	1.91	9.262	0.0746	2.73	$-\pi/4$	1.425	3.351	0.458	$-\pi/4$	0.384	2.628	0.97
400 ^{0}C	1.92	9.271	0.0809	2.69	$-\pi/4$	1.397	3.336	0.487	$-\pi/4$	0.416	2.611	0.87
500 ^{0}C	1.67	9.298	0.0875	2.87	$-\pi/4$	1.445	3.374	0.514	$-\pi/4$	0.450	2.599	0.89

Table 8: 50-nm-thick poly-crystalline gold film, first heating cycle

T	ϵ_∞	ω_p (eV)	Γ_D (eV)	C_1	ϕ_1	γ_1 (eV)	$\hbar\omega_1$ (eV)	C_2	ϕ_2	γ_2 (eV)	$\hbar\omega_2$ (eV)	MSE
23 ^{0}C	1.90	8.800	0.0752	2.54	$-\pi/4$	1.344	3.112	0.245	$-\pi/4$	0.272	2.641	1.25
100 ^{0}C	2.05	8.876	0.0752	2.57	$-\pi/4$	1.350	3.106	0.250	$-\pi/4$	0.281	2.633	1.23
200 ^{0}C	1.85	8.927	0.0771	2.67	$-\pi/4$	1.444	3.194	0.327	$-\pi/4$	0.339	2.631	0.98
250 ^{0}C	1.59	8.713	0.0706	2.54	$-\pi/4$	1.436	3.193	0.335	$-\pi/4$	0.356	2.622	0.97
300 ^{0}C	1.43	8.449	0.0725	2.25	$-\pi/4$	1.464	3.242	0.406	$-\pi/4$	0.404	2.614	0.90
350 ^{0}C	1.38	8.365	0.0726	2.24	$-\pi/4$	1.460	3.221	0.390	$-\pi/4$	0.408	2.606	0.86
400 ^{0}C	2.34	8.683	0.0877	2.26	$-\pi/4$	1.286	3.046	0.289	$-\pi/4$	0.381	2.589	0.85
450 ^{0}C	2.46	9.002	0.1451	2.45	$-\pi/4$	1.311	3.140	0.346	$-\pi/4$	0.408	2.594	0.79
500 ^{0}C	2.39	8.949	0.1770	2.18	$-\pi/4$	1.270	3.226	0.488	$-\pi/4$	0.479	2.585	0.85

Table 9: 30-nm-thick poly-crystalline gold film, first heating cycle

T	ϵ_∞	ω_p (eV)	Γ_D (eV)	C_1	ϕ_1	γ_1 (eV)	$\hbar\omega_1$ (eV)	C_2	ϕ_2	γ_2 (eV)	$\hbar\omega_2$ (eV)	MSE
23 ^{0}C	1.91	8.670	0.0740	2.57	$-\pi/4$	1.318	3.078	0.195	$-\pi/4$	0.267	2.634	1.10
100 ^{0}C	1.22	8.724	0.0769	2.98	$-\pi/4$	1.899	3.434	0.440	$-\pi/4$	0.392	2.665	1.09
200 ^{0}C	1.43	8.767	0.0780	2.91	$-\pi/4$	1.619	3.283	0.353	$-\pi/4$	0.376	2.642	1.10
250 ^{0}C	1.21	8.629	0.0715	2.68	$-\pi/4$	1.674	3.381	0.463	$-\pi/4$	0.429	2.634	1.08
300 ^{0}C	1.61	8.525	0.0744	2.26	$-\pi/4$	1.448	3.239	0.451	$-\pi/4$	0.442	2.615	1.04
350 ^{0}C	2.12	8.547	0.0890	2.08	$-\pi/4$	1.302	3.128	0.399	$-\pi/4$	0.436	2.594	0.97
400 ^{0}C	2.64	8.773	0.152	2.10	$-\pi/4$	1.263	3.131	0.404	$-\pi/4$	0.451	2.598	0.99
450 ^{0}C	3.69	8.773	0.354	0.68	$-\pi/4$	0.607	3.401	0.977	$-\pi/4$	0.568	2.621	1.41

3.4.2   Temperature-dependent Drude-Lorentz oscillator models for Ag thin films

We used the following form of Drude-Lorentz oscillator model to fit the elevated temperature ellipsometer data for Ag films:

$$\hat{\epsilon}(\omega) = \epsilon_\infty - \frac{\omega_p^2}{\omega^2 + i\Gamma_D\omega} + \frac{C_1}{(\hbar\omega_1)^2 - (\hbar\omega)^2 - i\gamma_1(\hbar\omega)}$$

All our Ag films were fitted with one Lorentz oscillator. The tables below show the extracted temperature dependent parameters from the fits at different temperatures.

Table 10: 450-nm-thick single-crystalline Ag film, first heating cycle

T (^{0}C)	ϵ_∞	ω_p (eV)	Γ_D (eV)	C_1(eV^2)	γ_1 (eV)	ω_1 (eV)	MSE
23	3.40	9.19	0.044	9.47	0.09	4.21	1.19
200	3.74	9.44	0.059	8.39	0.15	4.12	0.52
400	3.79	9.51	0.064	9.66	0.33	4.14	0.67
600	3.41	9.49	0.067	15.17	0.63	4.32	0.84
700	3.83	9.55	0.079	12.67	0.75	4.29	0.75

Table 11: 200-nm-thick single-crystalline Ag film, first heating cycle

T (^{0}C)	ϵ_∞	ω_p (eV)	Γ_D (eV)	C_1(eV^2)	γ_1 (eV)	ω_1 (eV)	MSE
23	3.66	9.40	0.039	10.51	0.13	4.25	0.81
200	3.92	9.61	0.039	11.16	0.26	4.24	0.62
400	3.98	9.68	0.056	13.45	0.51	4.32	0.67
600	3.22	9.61	0.060	20.96	0.73	4.49	1.00
700	3.08	9.61	0.069	23.90	0.84	4.58	0.96

Table 12: 34-nm-thick single-crystalline Ag film, first heating cycle

T (^{0}C)	ϵ_∞	ω_p (eV)	Γ_D (eV)	C_1(eV^2)	γ_1 (eV)	ω_1 (eV)	MSE
23	3.38	8.87	0.026	7.27	0.14	4.15	1.80
200	3.83	9.21	0.050	6.75	0.20	4.09	0.79
400	3.50	9.38	0.073	11.32	0.37	4.19	0.91
600	1.55	9.39	0.084	55.18	0.96	5.10	1.14

Table 13: 40-nm-thick poly-crystalline Ag film, first heating cycle

T (^{0}C)	ϵ_∞	ω_p (eV)	Γ_D (eV)	C_1(eV^2)	γ_1 (eV)	ω_1 (eV)	MSE
23	2.96	9.07	0.060	15.04	0.26	4.42	1.69
100	3.03	9.22	0.057	14.95	0.22	4.37	0.66
200	2.44	8.76	0.088	15.47	0.25	4.35	1.92
300	1.94	8.85	0.340	17.22	0.10	4.31	2.37

Table 14: 100-nm-thick single-crystalline Ag film, first heating cycle

T (^{0}C)	ϵ_∞	ω_p (eV)	Γ_D (eV)	C_1(eV^2)	γ_1 (eV)	ω_1 (eV)	MSE
23	2.39	9.05	0.063	24.58	0.23	4.66	1.25
200	3.11	9.21	0.090	10.75	0.16	4.18	1.34
400	2.37	9.18	0.105	19.66	0.35	4.37	1.47
600	2.41	9.26	0.131	23.51	0.59	4.52	1.29

3.4.3 Temperature-dependent Drude-Lorentz oscillator models for TiN thin films

We used the following form of Drude-Lorentz model to describe the dielectric function of TiN thin films:

$$\hat{\epsilon}(\omega) = \epsilon_\infty - \frac{\omega_p^2}{\omega^2 + i\Gamma_D\omega} + \sum_{j=1}^{2} \frac{C_j}{(\hbar\omega_j)^2 - (\hbar\omega)^2 - i\gamma_j(\hbar\omega)}$$

Table 15: 200-nm-thick single-crystalline TiN film, first heating cycle

T (^{0}C)	ε_∞	$\omega_p(eV)$	$\Gamma_D(eV)$	$C_1(eV^2)$	$\Upsilon_1(eV)$	$\omega_1(eV)$	$C_2(eV^2)$	$\Upsilon_2(eV)$	$\omega_2(eV)$
23	4.74	7.01	0.23	36.7	1.45	4.1	3.88	1.33	1.85
200	4.35	7.06	0.28	39	1.15	4.01	4.33	1.38	1.92
400	3.89	7.20	0.37	54.4	1.40	4.24	3.61	1.46	1.95
500	3.58	7.25	0.40	66.3	1.54	4.39	3.58	1.54	1.94
600	3.37	7.31	0.45	76.8	1.70	4.50	2.91	1.44	1.96
700	3.14	7.37	0.50	92.2	1.94	4.67	2.22	1.27	1.94
800	2.67	7.39	0.58	114.9	2.13	4.90	1.15	0.92	2.00
900	2.08	7.17	0.66	122.6	2.13	4.96	0.46	0.58	2.01

Table 16: 50-nm-thick single-crystalline TiN film, first heating cycle

T (°C)	ε_∞	$\omega_p(eV)$	$\Gamma_D(eV)$	$C_1(eV^2)$	$\Upsilon_1(eV)$	$\omega_1(eV)$	$C_2(eV^2)$	$\Upsilon_2(eV)$	$\omega_2(eV)$
23	5.18	7.38	0.26	42.2	1.42	4.07	2.26	0.87	2.02
200	4.43	7.37	0.30	47.9	1.04	4.09	5.76	1.75	1.99
400	4.28	7.49	0.37	60.0	1.19	4.26	7.05	2.03	1.93
500	4.28	7.52	0.40	66.0	1.30	4.33	7.29	2.06	1.90
600	4.30	7.55	0.43	70.3	1.40	4.37	7.68	2.14	1.86
700	4.06	7.59	0.47	81.7	1.54	4.47	7.11	2.00	1.86
800	3.21	7.55	0.53	110	1.83	4.72	5.38	1.82	1.84
900	1.00	7.27	0.57	187	2.30	5.23	3.01	1.49	1.78

Table 17: 30-nm-thick single-crystalline TiN film, first heating cycle

T (°C)	ε_∞	$\omega_p(eV)$	$\Gamma_D(eV)$	$C_1(eV^2)$	$\Upsilon_1(eV)$	$\omega_1(eV)$	$C_2(eV^2)$	$\Upsilon_2(eV)$	$\omega_2(eV)$
23	3.93	7.10	0.29	62.9	1.39	4.40	3.97	1.35	2.03
200	3.75	7.12	0.33	65.3	0.97	4.42	8.53	2.22	2.08
400	3.17	7.21	0.39	95.9	1.15	4.77	10.53	2.59	2.00
500	2.64	7.22	0.43	125.4	1.37	5.04	9.80	2.48	1.95
600	2.16	7.25	0.48	158.8	1.63	5.30	8.34	2.22	1.90
700	1.30	7.28	0.54	211	1.92	5.62	6.61	1.94	1.88
800	1.00	7.24	0.63	227.8	2.29	5.68	2.98	1.34	1.90
900	1.00	7.04	0.74	197.7	2.57	5.47	0.31	0.46	1.96

4. QUANTIFICATION OF PLASMONIC HOT-CARRIER ENERGY DISTRIBUTIONS: THEORY, MOLECULAR SYNTHESIS AND SAMPLE PREPARATION

Most of the material presented in this chapter is taken verbatim from the following paper: Reddy, Harsha et al. "Determining plasmonic hot-carrier energy distributions via single-molecule transport measurements", *Science*, 369 (6502), 423-426, 2020.

This chapter introduces the theoretical framework and explains the central ideas of how transport measurements through single molecular junctions with suitably transmission characteristics enable the quantification of hot-carrier energy distributions in plasmonic nanostructures. The synthesis details of molecules used in this work, the growth of ultra-thin Au films and the preparation of monolayer of molecules will be described.

4.1 Background and approach to determine the energy distributions of plasmonic hot-carriers

As outlined in the introduction, "Hot-carriers" that are highly energetic electrons and holes with energy distributions that deviate significantly from equilibrium Fermi-Dirac distributions [20], are expected to arise in metallic (plasmonic) nanostructures due to the non-radiative decay of surface plasmons. Such hot-carriers are of great fundamental interest and hold promise for the development of a variety of novel technologies, including plasmon-driven photochemistry [22–24], alternative solar-energy harvesting devices [21], and efficient photodetectors operating below bandgap [26–28]. A key aspect that is central to the design and development of these applications is knowledge of the energy spectrum of the generated hot-carriers under steady-state conditions [29]. Due to the daunting experimental challenges in quantifying hot-

carrier energy distributions, researchers had to resort to first-principle calculations or semi-classical approaches to estimate this crucial information [30, 31, 33]. However, such computational approaches involve numerous assumptions on the dominant relaxation pathways of hot-carriers as well as material properties [32] that greatly influence the predictions and lead to a large uncertainty in the estimated hot-carrier energy spectrum [31, 33]. For example, some newer calculations have even suggested that the deviations from the equilibrium Fermi-Dirac distribution are negligibly small, questioning if hot-carrier distributions even have a discernible effect [34]. Direct experimental observations of hot-carrier distributions are therefore crucial for obtaining a precise understanding of the generation, decay, density and energy spectrum of hot-carriers as well as for rationally engineering the aforementioned technologies.

Here, we show how advanced scanning probe-based techniques [36–38] that measure the charge transport in single molecules, when combined with nanoplasmonic experimental methods, can be leveraged to directly quantify the steady-state energy distribution of hot-carriers ($f_{hot}(E)$) in a key model system—a plasmonic gold thin film that supports propagating surface plasmon polaritons (SPPs). Our basic strategy is to first create single molecule junctions (SMJs)—using carefully chosen molecules with appropriate transmission characteristics (see below)—between a plasmonic gold (Au) film and the Au tip of a scanning tunneling microscope (STM), and elucidate the current voltage characteristics with and without plasmonic excitation at various voltage biases (V) (see Figure 4.1A). The difference in the measured currents for the cases with ($I_{SPP}(V)$) and without ($I_d(V)$) plasmonic excitation, which we call the hot-carrier current $I_{hot}(V) = I_{SPP}(V) - I_d(V)$, enables us to directly infer the energy distribution of the hot-carriers $f_{hot}(E)$.
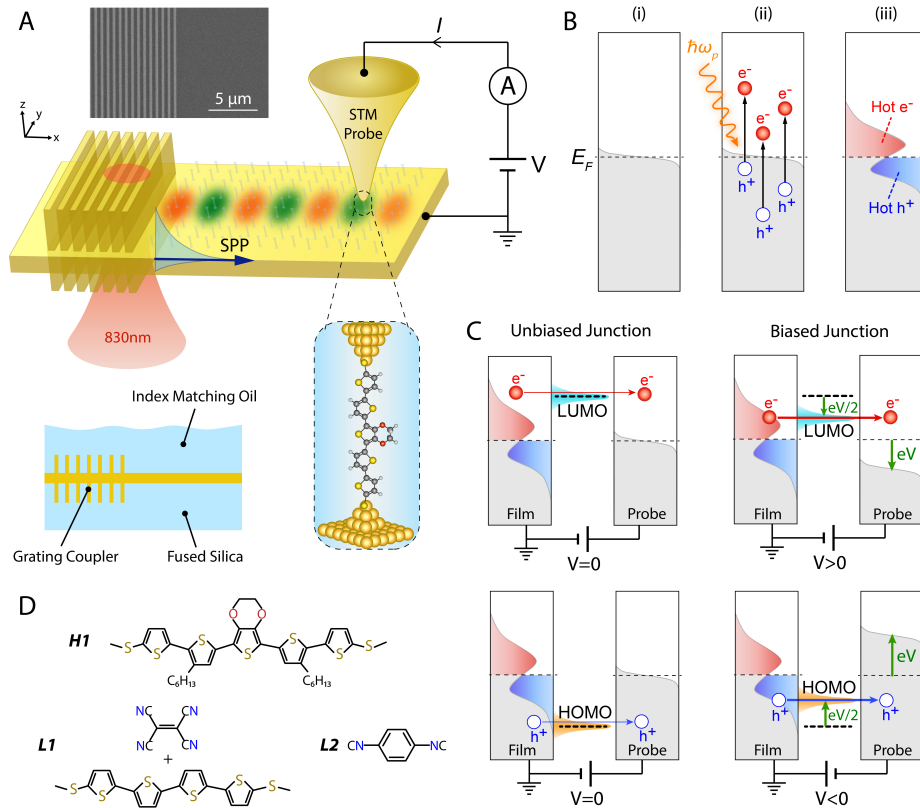
Fig. 4.1. Experimental setup and strategy to map hot-carrier energy distributions. (A) Schematic representation of the experimental set-up. Single molecule junctions (SMJs) are formed between a nanofabricated Au film with integrated gratings and a Au STM probe when the probe is withdrawn from the surface after contact (see text). Bias voltages are applied to the STM probe relative to the grounded sample. Hot-carriers are generated via surface plasmon polaritons (SPPs) by illuminating the grating coupler with 830 nm CW laser, and the currents flowing through the SMJs in the presence and absence of hot-carriers are measured. The SEM image (top left) shows a 6 nm-thick Au film with a nanofabricated grating coupler, the bottom left schematic represents a cross-section of the fused silica substrate and the grating coupler with index matching oil on top. (B) Schematic of hot-carrier generation and their energy distributions. (i) Equilibrium Fermi function. (ii) Non-radiative decay of SPP energy ($\hbar\omega_p$) generates electron-hole pairs, resulting (iii) in a non-equilibrium carrier distribution of hot-electrons and holes. (C) Schematic showing how SMJ currents can reveal the energy spectrum of hot-carriers. LUMO or HOMO-dominated SMJs with sharp peaks in their transmission function (depicted as Lorentzian) selectively transmit hot-carriers with matching energies. Biasing the junctions shifts the transmission peak as shown, enabling the determination of the relative energy spectrum of hot-carriers. (D) Molecular structures of HOMO (H1) and LUMO (L1 and L2) molecules used in this work.

To elaborate, as depicted in Figure 4.1B & 4.1C, $I_{hot}(V)$ arises due to the generation of non-equilibrium hot-carriers from the non-radiative decay of excited SPPs. The generated hot-carriers, governed by a non-equilibrium energy distribution $f_{ne}(E)$, in turn drive $I_{hot}(V)$ across the SMJ. We note that the energy distribution $f_{hot}(E)$ represents the difference between $f_{ne}(E)$, the non-equilibrium distribution under plasmonic excitation, and the equilibrium Fermi-Dirac distribution $f_{eq}(E)$ as $f_{hot}(E) = f_{ne}(E) - f_{eq}(E)$. As described below, $f_{hot}(E)$ can be readily obtained from $I_{hot}(V)$.
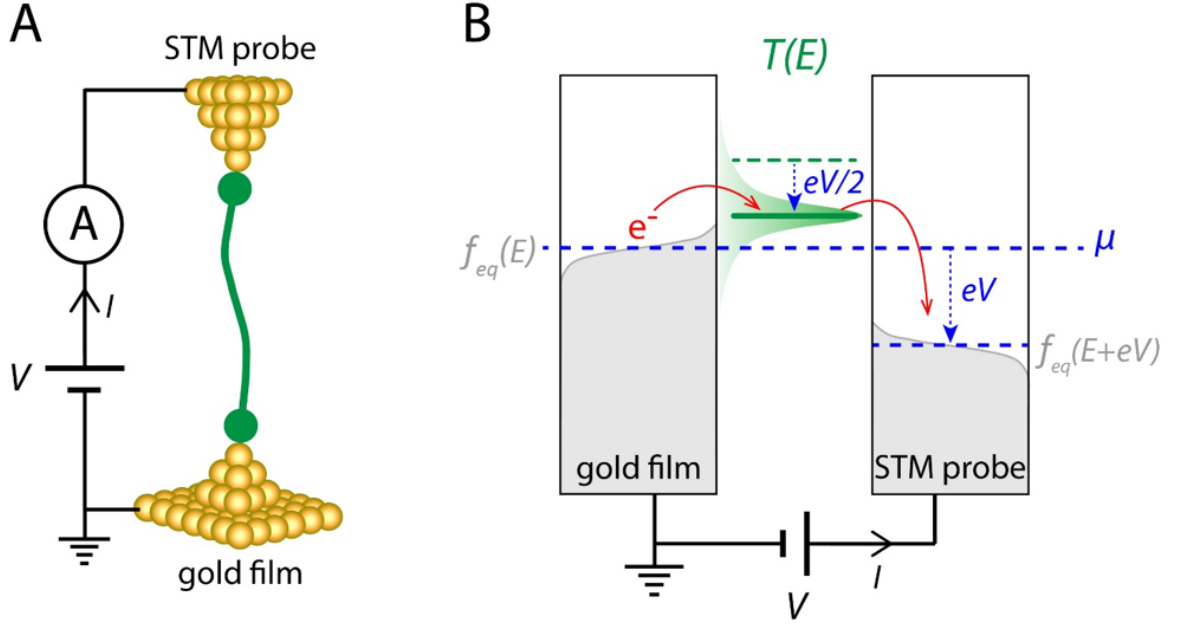
Fig. 4.2. Schematic describing the experimental approach and the electrical current flowing through a molecular junction. (A) Schematic showing a SMJ trapped between a gold film and a gold STM probe. A voltage bias is applied to the STM probe while keeping the gold film grounded, and the current flowing through the junction is measured using an external current amplifier (Stanford Research Systems, SR570 low-noise current amplifier). (B) Upon applying a voltage bias, the Fermi level of the STM probe shifts from the equilibrium chemical potential μ as depicted leading to a current (I) through the molecular junction that is proportional to the electronic transmission function $T(E)$. The green colored Lorentzian shape represents the $T(E)$ of the molecular junction and $f_{eq}(E)$ is the equilibrium Fermi function.

The current ($I_d(V)$) flowing through a single molecule junction (SMJ) (from the STM probe to the gold film as shown in Figure 4.2) under the biasing scheme shown above but without plasmonic excitation can be described within the Landauer-Büttiker approach for coherent transport as [54]:

$$I_d(V) = \frac{2e}{h} \int_{-\infty}^{\infty} T\left(E + \frac{eV}{2}\right)[f_{eq}(E) - f_{eq}(E + eV)]dE, \qquad (4.1)$$

where $f_{eq}(E) = [1 + exp[(E - \mu)/K_B T]^{-1}$ is the equilibrium Fermi function, e is the elementary charge, h is the Planck constant and $T(E)$ is the electronic transmission function of the SMJ, when no bias is applied across the junction. Here the chemical potential $\mu = E_F$ is the Fermi energy.

As described above, the non-radiative decay of SPPs that are excited on an ultra-thin Au film (via 830 nm laser illumination) leads to the generation of non-equilibrium hot-carriers. The generated hot-carriers result in a modified distribution function ($f_{ne}(E)$), which can be represented as

$$f_{ne}(E) = f_{eq}(E) + f_{hot}(E), \qquad (4.2)$$

where $f_{hot}(E)$ is the energy distribution of the generated hot-carriers. (In general, this function is dependent on the spatial location, but this is not explicitly shown here.) As a result of the non-equilibrium distribution function $f_{ne}(E)$, the current flowing through the SMJ under the excitation of SPPs ($I_{SPP}(V)$) is modified as

$$I_{SPP}(V) = \frac{2e}{h} \int_{-\infty}^{\infty} T\left(E + \frac{eV}{2}\right)[f_{ne}(E) - f_{eq}(E + eV)]dE. \qquad (4.3)$$

Therefore, the resulting additional current flowing through the SMJ due to the generated hot-carriers, $I_{hot}(V)$, is given by:

$$I_{hot}(V) = I_{SPP}(V) - I_d(V) = \frac{2e}{h} \int_{-\infty}^{\infty} T\left(E + \frac{eV}{2}\right)[f_{ne}(E) - f_{eq}(E)]dE. \qquad (4.4)$$

Using Eq. 4.2 and a change of variable $E' = E + eV/2$ we can rewrite Eq. 4.4 as

$$I_{hot}(V) = \frac{2e}{h} \int_{-\infty}^{\infty} T(E') f_{hot}\left(E' - \frac{eV}{2}\right) dE'. \tag{4.5}$$

For the purpose of retrieving $f_{hot}(E)$ it is insightful to consider the following integral transform of Eq. 4.5

$$\int_{-\infty}^{\infty} I_{hot}(V) e^{\frac{-i\omega eV}{2}} d\left(\frac{eV}{2}\right) = \frac{2e}{h} \int_{-\infty}^{\infty} \int_{-\infty}^{\infty} T(E') f_{hot}\left(E' - \frac{eV}{2}\right) dE' e^{\frac{-i\omega eV}{2}} d\left(\frac{eV}{2}\right). \tag{4.6}$$

Using the properties of Fourier transform, Eq. 4.6 can be rewritten as

$$\frac{e}{2} \tilde{I}_{hot}\left(\frac{e\omega}{2}\right) = \frac{2e}{h} \int_{-\infty}^{\infty} \int_{-\infty}^{\infty} T(E') f_{hot}\left(E' - \frac{eV}{2}\right) dE' e^{\frac{-i\omega eV}{2}} d\left(\frac{eV}{2}\right). \tag{4.7}$$

$\tilde{I}_{hot}$ is the Fourier transform of $I_{hot}(V)$ $(\tilde{I}_{hot} = \int_{-\infty}^{\infty} I_{hot}(V) e^{-i\omega V} dV)$. After interchanging the order of integration and rearranging the terms in Eq. 4.7 we obtain

$$\frac{e}{2} \tilde{I}_{hot}\left(\frac{e\omega}{2}\right) = \frac{2e}{h} \int_{-\infty}^{\infty} T(E') \int_{-\infty}^{\infty} f_{hot}\left(E' - \frac{eV}{2}\right) e^{\frac{-i\omega eV}{2}} d\left(\frac{eV}{2}\right) dE', \tag{4.8}$$

$$\implies \frac{e}{2} \tilde{I}_{hot}\left(\frac{e\omega}{2}\right) = \frac{2e}{h} \int_{-\infty}^{\infty} T(E') e^{-i\omega E'} \int_{-\infty}^{\infty} f_{hot}\left(E' - \frac{eV}{2}\right) e^{-i\omega\left(\frac{eV}{2} - E'\right)} d\left(\frac{eV}{2}\right) dE', \tag{4.9}$$

which gives

$$\tilde{I}_{hot}\left(\frac{e\omega}{2}\right) = \frac{2e}{h} \int_{-\infty}^{\infty} T(E') e^{-i\omega E'} \tilde{F}_{hot}^*(\omega) dE', \tag{4.10}$$

$$\implies \tilde{I}_{hot}\left(\frac{e\omega}{2}\right) = \frac{4}{h} \tilde{T}(\omega) \tilde{F}_{hot}^*(\omega), \tag{4.11}$$

$$\implies \tilde{F}_{hot}(\omega) = \frac{h}{4} \left[\frac{\tilde{I}_{hot}^*\left(\frac{e\omega}{2}\right)}{\tilde{T}^*(\omega)}\right], \tag{4.12}$$

$$\text{and } f_{hot}(E) = \tilde{f}^{-1}\left(\frac{h}{4}\left[\frac{\tilde{I}^*_{hot}(\frac{e\omega}{2})}{\tilde{T}^*(\omega)}\right]\right). \tag{4.13}$$

Here $\tilde{F}_{hot}(\omega)$ and $\tilde{T}(\omega)$ are the Fourier transforms of $f_{hot}(E)$ and $T(E)$, respectively, while $\tilde{f}^{-1}$ and * represent the inverse Fourier transform and complex conjugate, respectively. It is thus clear that $f_{hot}(E)$ can be completely determined from any arbitrary transmission function provided both $I_{hot}(V)$ and $T(E)$ are known for all voltage biases and energies—a stringent requirement impossible to meet in practical experimental scenarios. A strategy to overcome this limitation is to employ SMJs that feature sharp peaks in the transmission characteristics. $I_{hot}(V)$ in such SMJs can be readily obtained from the following simplified equation, as long as the hot-carrier distribution varies much more slowly than the transmission function (an excellent approximation as shown from both our computational expectations and experimental results):

$$I_{hot}(V) \approx \frac{2e}{h}f_{hot}\left(E_o - \frac{eV}{2}\right)\int_{-\infty}^{\infty} T(E')dE', \tag{4.14}$$

where E_o is the peak energy of the transmission function. Eq. 4.14 relates $I_{hot}(V)$ to $f_{hot}(E)$ via a constant scaling factor($\frac{2e}{h}\int_{-\infty}^{\infty} T(E'dE')$). Intuitively, the physical origin of the approximation used above, wherein the energy distribution of the hot-carriers is pulled out of the integral in Eq. 4.5, can be understood by noting that the SMJs with sharply peaked transmission characteristics serve as tunable voltage bias controlled energy filters. Therefore, given knowledge of $T(E)$ and by measuring the voltage bias dependent $I_{hot}(V)$ in the bias window of $\{V_o : -V_o\}$ $f_{hot}(E)$ can be accurately determined within the energy range $\{E_0 - \frac{eV_o}{2} : E_0 + \frac{eV_o}{2}\}$ (Figure 4.1C).

In this work, we employ molecules (Figure 4.1D) that form SMJs featuring sharp peaks in their transmission characteristics. The first SMJ is created from a charge-transfer complex of quaterthiophene (T4) and tetracyanoethylene (TCNE) with terminal thiophenes containing the gold-binding methyl sulfides (referred to as L1 in the manuscript). Based on past studies, SMJs created from L1 are expected to exhibit transmission characteristics dominated by the lowest unoccupied molecular orbital (LUMO) with a resonance very close to the Fermi level [55,56] that arises as a

consequence of the charge-transfer interaction between the oligothiophene backbone and the TCNE LUMO. The second SMJ is created from 3,4-ethylenedioxythiophene (EDOT), flanked by two thiophenes with terminal thiophenes containing gold-binding methyl sulfides (referred to as H1). In contrast to L1, the transmission characteristics of H1 are dominated by the highest occupied molecular orbital (HOMO) [57]. Finally, we also utilize 1,4-benzenediisonitrile molecules (referred to as L2). SMJs formed with this molecule exhibit transmission characteristics that are also dominated by the LUMO [58], but features a relatively weak energy dependence. As described in **Chapter 6**, experiments performed using these three SMJs enable a complete experimental quantification of the energy spectrum of the hot-carriers generated in the plasmonic films investigated in this work. The synthesis details of these molecules is described in the next section.

4.2 Chemical synthesis of L1, L2 and H1 molecules

4.2.1 Synthesis of molecule L1
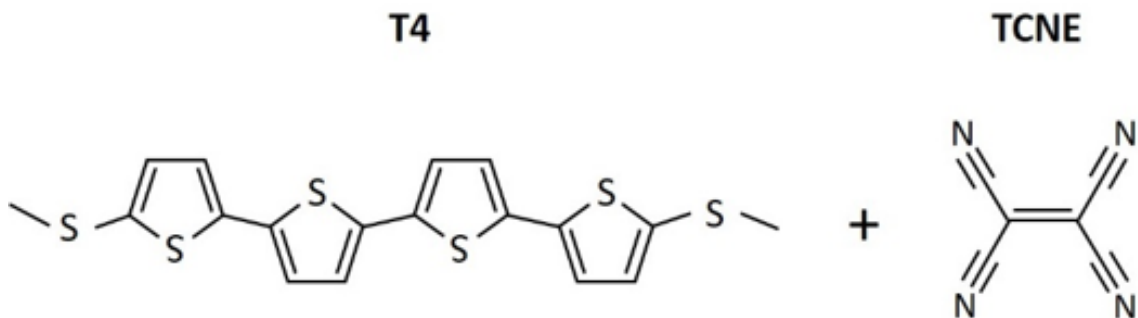
Fig. 4.3. Chemical structure of molecule L1.

The molecule L1 is the charge-transfer complex of quaterthiophene (T4) and tetra-cyanoethylene (TCNE) with the terminal thiophenes containing the gold-binding methyl sulfides (Figure 4.3). Molecule T4 was synthesized using a method previ-

ously reported in (21). Tetracyanoethylene (TCNE, 98%) was purchased from Sigma-Aldrich and used without further purification. The preparation of the charge-transfer complex of T4 and TCNE is described in the discussion of molecular sample preparation outlined in section 4.4.

4.2.2   Synthesis of molecule L2

Molecule L2 was purchased from Sigma Aldrich (97%) and used without further purification.

4.2.3   Synthesis of molecule H1

Molecule H1 was commercially synthesized by LifeTein, LLC, following the same synthesis steps reported in Ref [57]. The key steps involved in the synthesis of H1 are shown in Figure 4.4 and are briefly outlined below. 2-(methylthio)thiophene (compound 1) and 2-bromo-3-hexylthiophene (compound 3) were purchased from Sigma-Aldrich and used without further purification, as was 3,4-ethylenedioxythiophene which was converted to compound 6 by a previously reported method [59]. All palladium coupling and lithiation reactions were done in oven-dried glassware using dry solvents from a solvent still. To determine and verify the molecular structure, ESI+MS and NMR measurements were performed on the synthesized molecule H1. The measured molecular weight of molecule H1 from ESI+MS was found to be 730.1212, in excellent agreement with the expected molecular weight of 730.1224. The measured ^{1}H-NMR and ^{13}C-NMR results on H1 are shown in Figure 4.5, which are in good agreement with reports from a prior work [57].
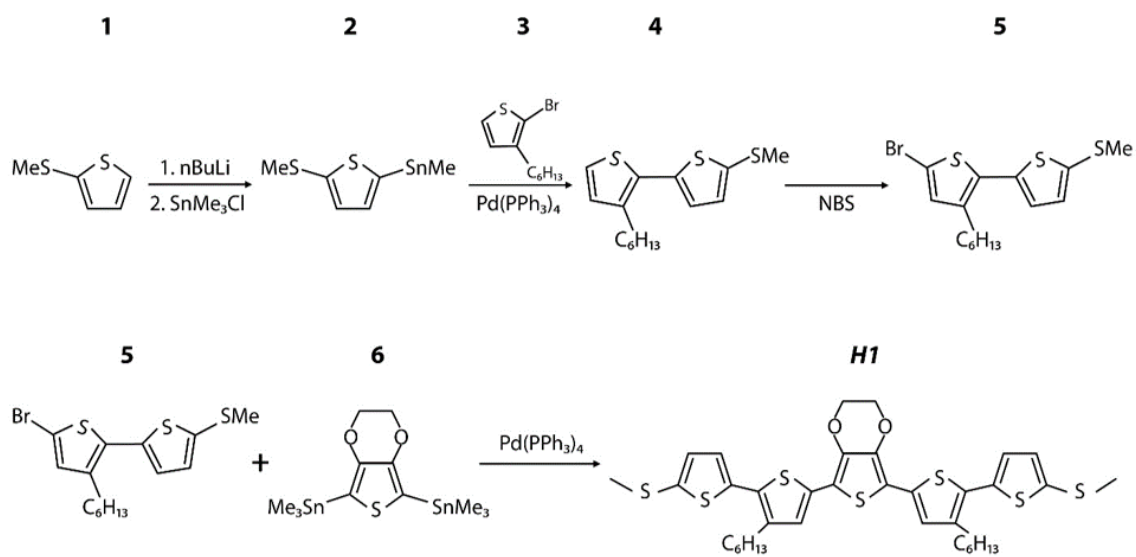
Fig. 4.4. Key steps involved in the synthesis of molecule H1.

Fig. 4.5. NMR spectra of molecule H1. Measured ^{1}H-NMR (A) and ^{13}C-NMR (B) spectra of the synthesized molecule H1. Both ^{1}H-NMR and ^{13}C-NMR measurements were performed at room temperature. Solvent residual peaks are marked in the spectra with an asterisk—^{1}H NMR: 7.26 ppm = CHCl$_3$; 1.56 ppm = H$_2$O and ^{13}C NMR: 77.0 ppm = CDCl$_3$. The curved lines in ^{1}H-NMR spectra are the integration lines of the peak.

4.3 Ultra-thin gold film preparation, fabrication of grating coupler and Au STM probe preparation

In our work, we utilized plasmonic gold films fabricated on fused silica substrates (Figure 4.1A) with integrated rectangular metallic grating strips to excite SPPs and generate hot-carriers. We note that in our experiments the thickness of the Au films was as small as 6 nm. In such thin films, the strong confinement of carriers is expected to result in increased surface scattering-assisted absorption of plasmons—Landau damping—that enhances hot-carrier generation [4,32,60]. One of the major roadblocks to our experiments was producing thin (thickness < 10 nm), smooth and continuous Au films, which is known to be very challenging due to island formation [61,62]. We overcame this technical hurdle by functionalizing the fused silica substrates with an organofunctional silane—(3-mercaptopropyl) trimethoxysilane (MPTMS)—featuring thiol end groups. The key steps involved in the preparation of these ultra-thin Au films are outlined below.

Our approach to produce smooth and continuous Au films with sub-10 nm thickness closely follows the approach described in Ref [63]. The key steps involved in the preparation of ultra-thin gold films are outlined in Figure 4.6. We begin by using UV grade fused silica (obtained from MTI Corporation, 1 cm x 1 cm x 0.5 mm) as substrate. Substrates were cleaned in a freshly prepared piranha solution (3:1 mixture of H_2SO_4 and H_2O_2) and kept at 80 °C for 20 min. This step removes organic residues while also hydroxylating the surface. Subsequently, the substrates were rinsed in deionized water, dried in a stream of dry nitrogen gas and immediately transferred to a beaker filled with a 0.5% solution of MPTMS in toluene to incubate for 24 hours at room temperature. As established in prior work, this process functionalizes fused silica substrates with a monolayer of MPTMS, forming strong covalent siloxane bonds and free thiol end groups [64,65] (see schematic in Figure 4.6). Following the incubation period, the substrates were thoroughly cleaned in toluene to remove excess MPTMS solution. The functionalized substrates were dried under

nitrogen gas and transferred to an electron beam evaporation chamber. Gold was then evaporated at a base pressure of 2 x 10^{-6} mbar at a deposition rate of 0.1 nm/s. The thiol groups form strong bonds with evaporated gold and enable preparation of continuous Au films with sub-10 nm thickness. The deposited film thickness was monitored using a crystal oscillator located inside the evaporation chamber. Additionally, the deposition rate was independently verified by depositing a nominally 30 nm-thick film on a substrate and was subsequently confirmed by SEM cross-section analysis that the film was indeed close to 30 nm thick. Using this functionalization method, smooth and continuous Au films with thicknesses down to 6 nm were obtained (see SEM micrographs and AFM scans in Figure 4.7). Topography scans from AFM measurements revealed a smooth texture with $\sim$ 0.38 nm rms roughness, as opposed to films obtained on untreated fused silica substrates that displayed granular and semi-continuous characteristics with a roughness of 0.83 nm.
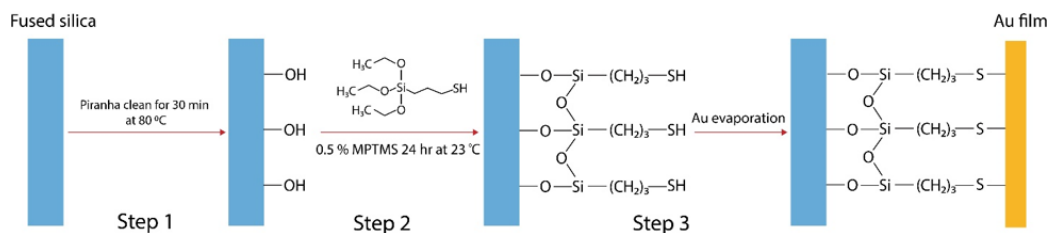
Fig. 4.6. Illustration of gold thin film preparation. (Step 1) Hydroxylation of fused silica substrates. (Step 2) Formation of Siloxane bonds and monolayer of MPTMS. (Step 3) Evaporation of Au film.
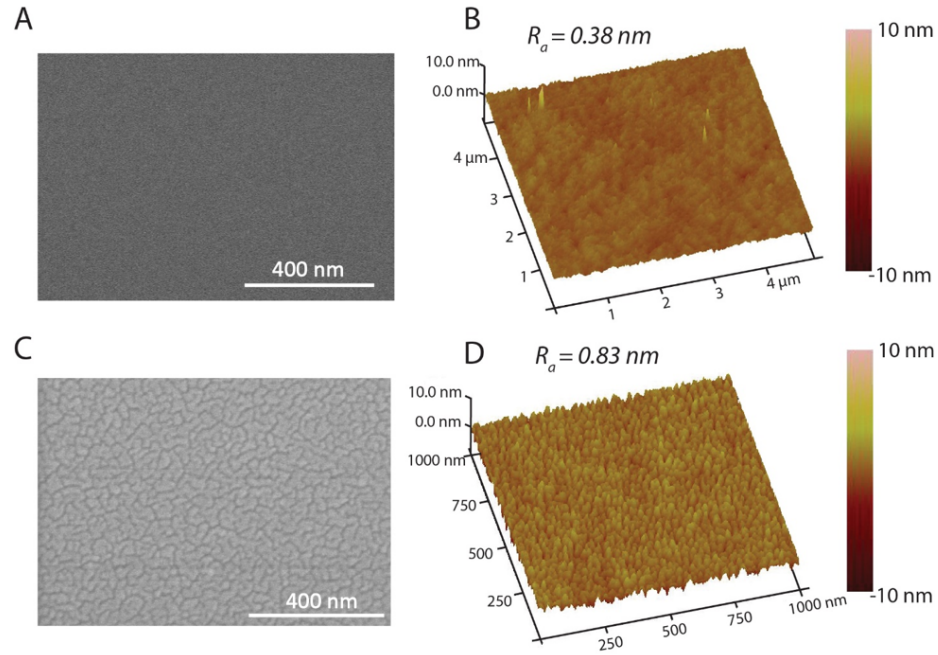
Fig. 4.7. SEM and AFM images of 6 nm Au films. (A) & (B) SEM micrograph and AFM topograph of a 6 nm Au film evaporated on a fused silica substrate activated with MPTMS, revealing the smooth and continuous texture of the gold film. The color gradient in (B) shows the color coding for the height and depth profile. (C, D) Same as in (A, B), respectively, but for a film evaporated on bare untreated fused silica substrate. To reveal the semi-continuous and granular nature of the film grown on untreated substrate, an AFM scan on a smaller area ($1\mu m^2$) is shown in (D). The rms roughness R_a from AFM scans are shown in (C) and (D).

Furthermore, Au films deposited on MPTMS activated substrates showed a golden metallic luster, while those produced on untreated bare substrate had a bluish luster (Figure 4.8), suggesting absorption due to plasmon resonances in the semi-continuous films. This was subsequently confirmed with optical transmission spectroscopy (using a V-VASE JA Woolam ellipsometer). Films grown on bare fused silica substrates showed a pronounced dip in the transmission around 750 nm wavelength (Figure 4.9), which can be attributed to additional absorption from surface plasmon resonances arising from the granular gold structures in the semi-continuous film. On the other

hand, films grown on the MPTMS functionalized substrate showed no dips in the transmission spectrum. Similar features in the transmission spectrum were observed in semi-continuous films and films grown on MPTMS activated substrate from prior work [63]. Smooth and continuous 13 nm-thick gold films were also produced using the same MPTMS functionalization technique.
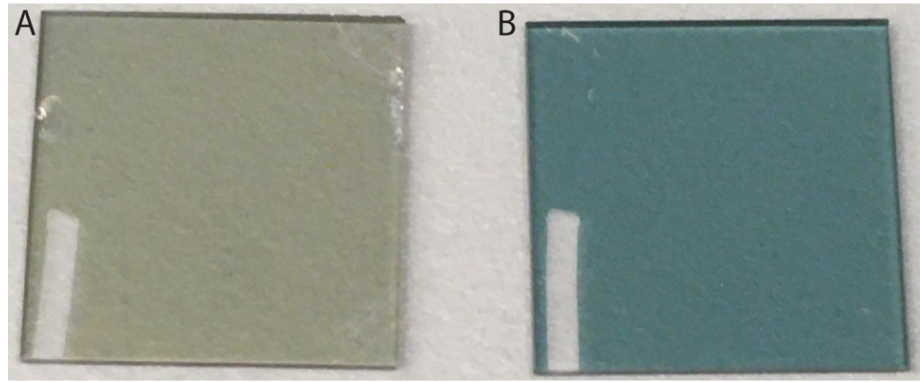
Fig. 4.8. Optical images of 6 nm Au films. Images of 6 nm-thick Au films deposited on MPTMS activated (A) and untreated fused silica substrates (B), showing the golden metallic luster and bluish color, respectively.

The grating couplers required for this work were fabricated on gold films evaporated on MPTMS activated substrates. Figure 4.10 shows the steps involved in our fabrication process flow. Briefly, positive E-beam resist PMMA A4-950 was spin-coated on the Au film to obtain a thickness of about 170 nm and soft baked at 165 °C for 2 minutes. This was followed by E-beam patterning and developing, thereby opening an array of periodic rectangular grating strips. Using the patterned resist as the mask, the gold layer underneath was physical etched in Ar plasma in an ion milling tool. Using the same mask, approximately 25 nm of SiO_2 was etched in a buffered oxide etch (BOE) opening trenches in fused silica. The grating coupler is then formed by depositing a stack of 3 nm Ti/ 50 nm Au/ 3nm Ti, ensuring a symmetric geometry, followed by liftoff and resist removal in Remover PG. The SEM images of the fabricated grating coupler are shown in Figure 4.11.
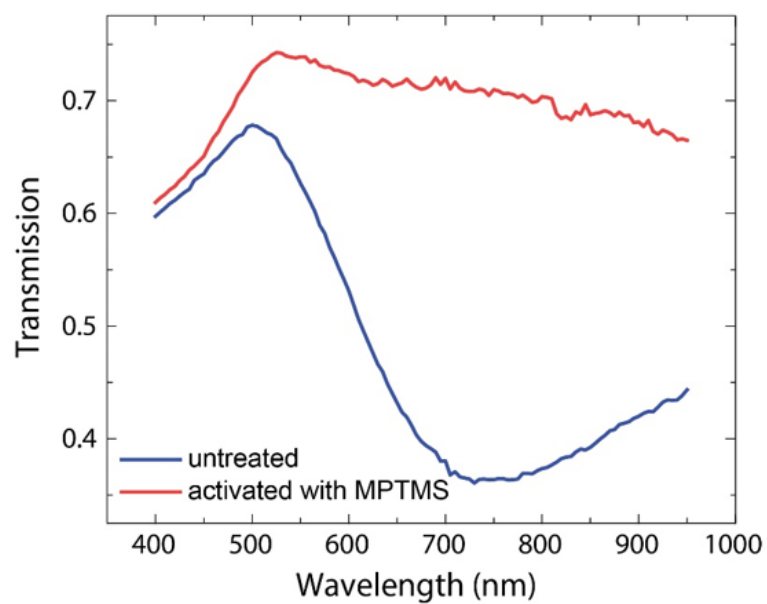
Fig. 4.9. Optical transmission spectra. Transmission spectra through 6 nm-thick Au films evaporated on untreated (blue curve) and MPTMS activated (red curve) fused silica substrates.
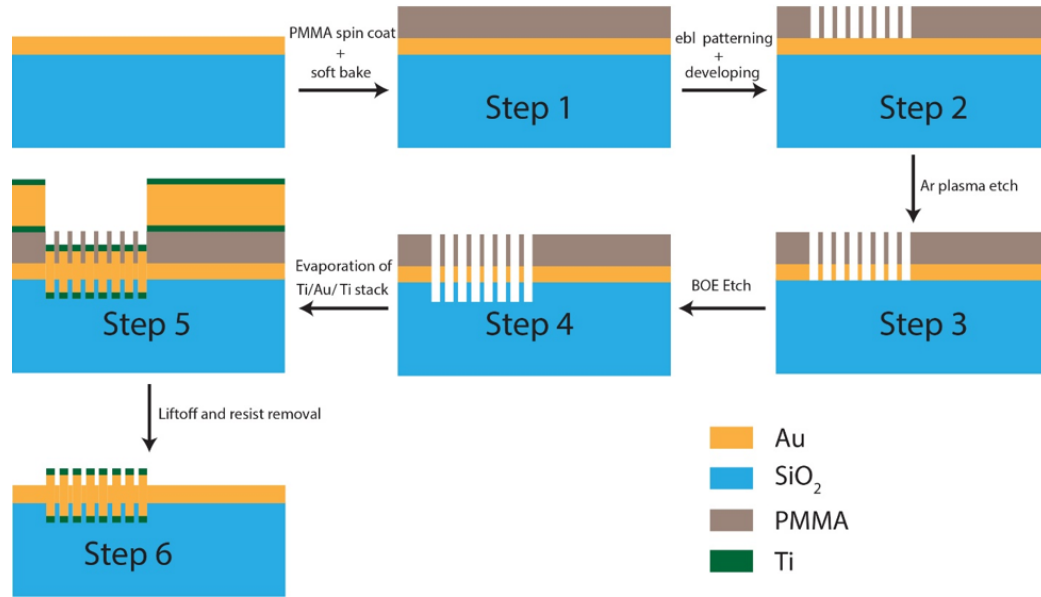
Fig. 4.10. Nanofabrication of the grating coupler. (Step 1) PMMA resist spin-coating followed by baking for 2 minutes at 165 °C. (Step 2) Patterning and developing of grating strips. (Step 3) Etching of Au film via Ar plasma. (Step 4) BOE etch and opening of trenches in fused silica substrates. (Step 4) Deposition of Ti/Au/Ti stack. (Step 5) Liftoff and formation of the grating coupler.
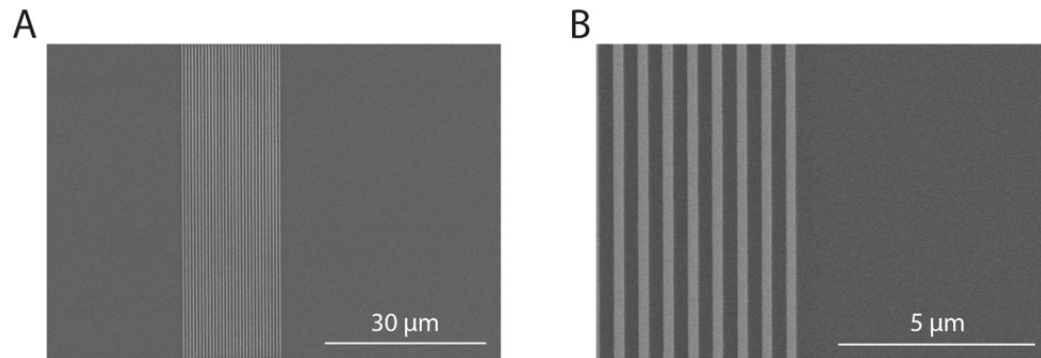
Fig. 4.11. SEM images of a nanofabricated grating coupler on a 6 nm Au film. The scale bars are included in the figures.

The Au STM probes used in this work were prepared following standard electro-chemical etching [66] of 1 mm diameter gold wires in concentrated HCl and ethanol solution (1:1 volume ratio).

4.4   Preparation of samples with molecular monolayers

A monolayer of L1 molecules was formed on our sample surface upon charge transfer complexation between T4 and TCNE. For this purpose, a freshly plasma-cleaned Au thin film with nanofabricated gratings was incubated in a solution of T4 molecules (1 mM, CH_2Cl_2: Ethanol 1:1) for 3 hours to allow the formation of a monolayer of T4 molecules. The sample was then thoroughly rinsed with ethanol and dried with high purity nitrogen gas. To form the T4-TCNE complexes, the prepared T4 monolayer was immersed in a TCNE solution (5 mM in CH_2Cl_2: Ethanol 1:1) for 5 hours. The sample was then copiously rinsed with ethanol and dried with high purity nitrogen gas. The resulting sample was used immediately for single molecule charge transport measurements.

To form the monolayers of L2 and H1 molecules, freshly plasma-cleaned Au thin films with nanofabricated gratings were incubated in solutions of either L2 (1mM in toluene) or H1 (1 mM in toluene) for 3-5 hours to allow the formation of respective molecular monolayers. The sample was then thoroughly rinsed with ethanol, dried with high purity nitrogen gas and was immediately used for single molecule transport measurements.

5. EXPERIMENTAL SETUP TO QUANTIFY HOT-CARRIER ENERGY DISTRIBUTIONS AND CONTROL EXPERIMENTS

Most of the material presented in this chapter is taken verbatim from the following paper: Reddy, Harsha et al. "Determining plasmonic hot-carrier energy distributions via single-molecule transport measurements", *Science*, 369 (6502), 423-426, 2020.

This chapter starts with a detailed discussion on the development of experimental methods that enabled the quantification of plasmonic hot-carrier energy distributions. Subsequently, preliminary experimental data and control experiments that unambiguously show the hot-carrier effects will be presented. Finally, the experimental technique used to map the transmission characteristics of the SMJs will be introduced.

5.1 Experimental setup and approach: An STM integrated with optical components and the creation of molecular junctions

In order to excite SPPs in the gold films and to facilitate the positioning of the STM tip at the desired location, we integrated illumination and imaging optics into our setup (Figure 4.1A and Figure 5.1). A linearly polarized 830 nm continuous wave (CW) laser is coupled into the illumination optics to excite SPPs in Au films via the integrated grating coupler. A linear translation stage facilitates control over the relative separation between the gratings and the STM probe with micrometer resolution in the lateral plane (xy plane in Figure 4.1A).
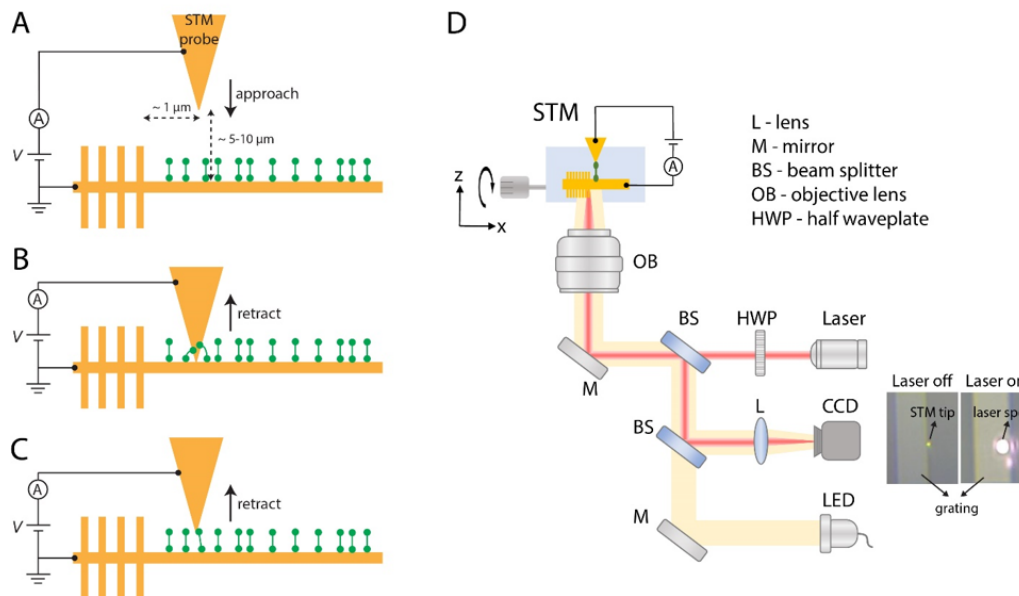
Fig. 5.1. Schematic representation of the experimental protocol and the optical components coupled into a scanning tunneling microscope. (A) A Gold STM probe is positioned about 1 μm from the grating edge and $\sim$ 5 - 10 μm above the ultra-thin gold film covered with a self-assembled monolayer of either L1, L2 or H1 molecules. Subsequently, the STM probe was displaced towards the sample until a Au-Au contact (B) was established. The formation of Au-Au contact is often associated with either one or a few molecules binding to the STM probe. The STM probe was then gradually withdrawn from the gold film at a rate of 2 nm/s. (C) During this process, the Au-Au contacts break sequentially, leading to a brief time window where a single molecular junction is formed between the gold film and the STM probe. (D) Schematic representation of our experimental setup showing the key optical elements integrated into an STM (Keysight model # 5500). A collimated, linearly polarized 830 nm CW laser is focused onto the sample (either a gold film with integrated grating coupler or a bare gold film) by a microscope objective lens (Zeiss Epiplan 20x HD objective lens) (OB). The sample is mounted on a linear translation stage and is covered with fused silica index matching oil (Cargille labs, Cat # 19571). A zero order half-wave plate (Thorlabs, $\lambda/2$ @ 830nm wavelength) (HWP) introduced into the laser beam path is used to control the polarization direction of the incident laser beam. Additionally, a white LED allows illumination of a 50 μm diameter region on the sample to image the tip of the STM probe, the nanofabricated grating coupler and the focused laser beam with a CCD camera as shown in the bottom right.

In our experiment, we first exposed the 6 nm-thick gold film to a solution containing L1 molecules to create a monolayer of the molecules (see discussion in section 4.4). Next, we positioned a Au STM tip at a distance of $\sim$1 μm from the grating edge and $\sim$5 - 10 μm above the plasmonic Au film (see schematic in Figure 5.1). Subsequently, the gold film was covered with fused silica index matching oil, creating a symmetric optical medium around the film. We then applied a bias voltage ($V_{bias} = 0.1$V) to the gold STM tip while grounding the 6 nm-thick gold film, and displaced the tip towards the sample, while monitoring the electrical current (I) using a current amplifier (see Figure 4.1A and Figure 5.1), until an electrical conductance (I/V_{bias}) of 0.1 G_o was obtained ($G_o \approx (12.9$ k$\Omega)^{-1}$ is the quantum of electrical conductance). The STM tip was then further displaced into the sample by 0.5 - 1 nm and a gold-to-gold contact was created. We then withdrew the tip from the Au sample at a rate of 2 nm/s, while simultaneously recording the electrical current. During the withdrawal, the Au-Au contact and Au-L1-Au junctions break sequentially, resulting in a precipitous decline in current (and conductance) with a few brief current plateaus. These brief plateaus represent periods where a single molecule or a few molecules are transiently trapped between the two gold electrodes. To unambiguously identify the conductance of a single molecule Au-L1-Au junction we leverage a well-established [36, 37] analysis method and plot the currents from many recordings in a histogram. Such a histogram from over 2000 traces along with representative conductance traces is shown in Figure 5.2A (grey color). The peak in the histogram at 6.59 nA represents the most probable current (I_d)—corresponding to a conductance of 8.5 x $10^{-4}G_o$ for a Au-L1-Au junction under dark conditions in the absence of plasmonic excitation. This is in good agreement with prior work [56]. Subsequently, we illuminated the gratings with a focused 830 nm laser beam linearly polarized perpendicular to the grating strips (estimated peak power density of 0.3 mW/μm^2), launching SPPs in the Au film (schematic in Figure 4.1A). Concurrently, we measured the electrical current, under laser illumination, following the same approach outlined above and found that the most probable electrical current under laser illumination, I_{SPP},

is larger than I_d(Figure 5.2A, magenta color). We then determined the hot-carrier current as $I_{hot}(V_{bias} = 0.1V) = I_{SPP}(V_{bias} = 0.1V)$ - $I_d(V_{bias} = 0.1V)$. The measured $I_{hot}(V_{bias} = 0.1V)$ displayed a strong dependence on the polarization of the 830 nm laser (Figure 5.2B). This behavior is consistent with the expectations based on the polarization dependent SPP excitation efficiency for grating strips, indicating that the measured $I_{hot}(V)$ is due to the excitation of SPPs.
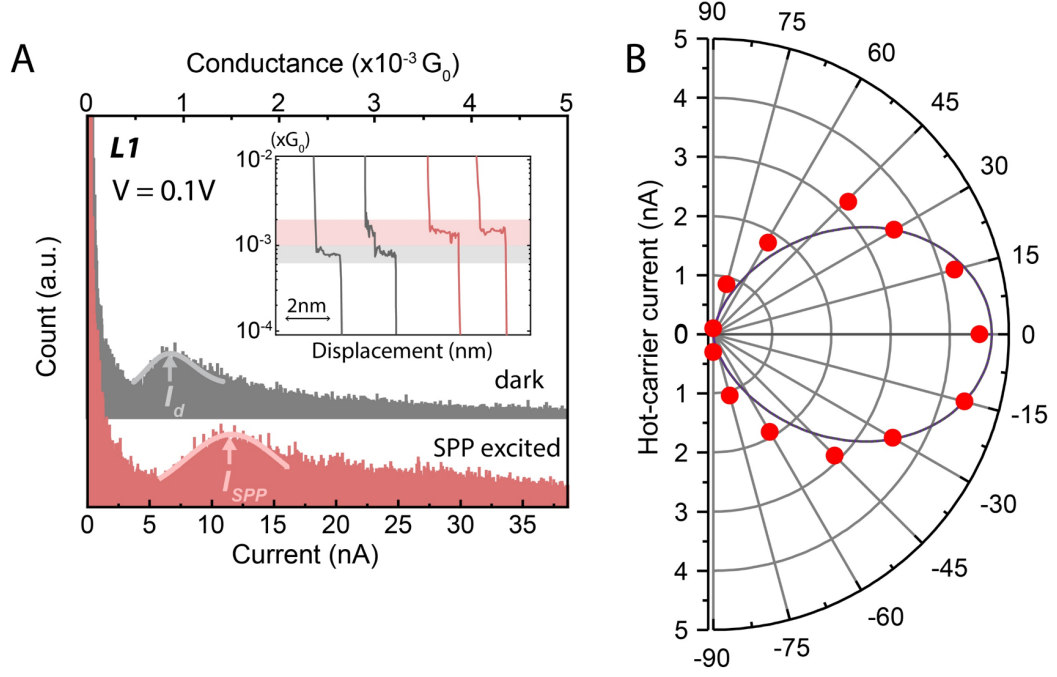
Fig. 5.2. Hot-carrier induced changes in SMJ currents and polarization dependence of Au-L1-Au SMJs. (A)Electrical current and conductance histograms of Au-L1-Au SMJs from over 2000 traces of dark (grey) and SPP-excited (magenta) measurements at a voltage bias of 0.1V. Gaussian fits to the histogram peaks are represented as solid lines and the most probable conductance and current are indicated by vertical arrows. Inset shows representative conductance traces for dark and SPP-exited measurements following the same color coding. (B)Polarization-dependence of the hot-carrier current for Au-L1-Au junctions (red circles) at 0.1V bias voltage along with the best-fit $\cos^2 \theta$ dependence (solid black line).

In order to assess the contributions of direct photon excitation of charges and temperature differentials to I_{hot}, we performed additional control experiments. To study the effect of pure light assisted transport, we created Au-L1-Au junctions on a 6 nm-thick Au film and measured the most probable current through SMJs at a voltage bias of 0.1V upon directly illuminating the junction and the STM probe with the same 830 nm laser at its peak power (schematic in Figure 5.3A). No gratings were involved in this experiment. The histogram constructed from one such measurement along with a typical histogram under no light illumination (dark) are shown in Figure 5.3A. As is evident from the figure, no perceptible changes in the most probable electrical current were observed. Additional experiments performed at varying laser powers further revealed no perceptible hot-carrier currents on bare Au film, while measurements performed by illuminating the gratings as described in the manuscript showed a linear dependence on the incident power (Figure 5.4). These control experiments ruled out the role of laser illumination assisted transport as a possible mechanism for the observed changes in the current.

We also performed experiments to determine if sample heating has an impact on the observed electrical conductance shifts. Towards this goal, we performed a measurement where a 6 nm-thick gold film was heated to temperatures ranging from 22 °C to 95 °C. To raise the temperature, the sample was attached onto a copper piece with an integrated Kapton heater, and the surface temperature was monitored using a thermocouple mounted on the surface of the gold film. At each temperature we measured the current through Au-L1-Au SMJs and constructed a current histogram for a bias of 0.1V as described in the manuscript. The results from these measurements at various temperatures are shown in Figure 5.3B. No discernable deviations were observed in the most probable current at all temperatures up to 95 °C. Furthermore, we performed opto-thermal simulations (see section 7.3.2 for additional details) and estimated that the maximum temperature rise in the 6 nm-thick gold film due to the absorption of incident laser power coupled into SPPs to be ~65 °C. Finally, using the measured transmission characteristics (see discussion in section 5.2), we estimated the

Seebeck coefficient of Au-L1-Au junctions to be $\sim 80\ \mu$V/K [67]. Therefore, a temperature differential of 42 K—as predicted from our opto-thermal simulation—would result in a Seebeck voltage of $\sim$3.4 mV. As a result, the expected additional thermoelectric current is only about 3.4% of the total current flowing through the junction at 0.1V. This simple analysis is consistent with the experimental observations in Figure 5.3B, indicating that the thermoelectric current arising from the temperature differential has negligible contributions. Our temperature dependent measurements taken together with the estimated temperature rise from the opto-thermal simulations establishes that the increased sample temperature has no observable contributions to the hot-carrier currents measured through the SMJs. These control experiments confirmed that the measured $I_{hot}(V)$ is indeed due to hot-carrier effects and not due to an increased temperature or simply the incidence of light
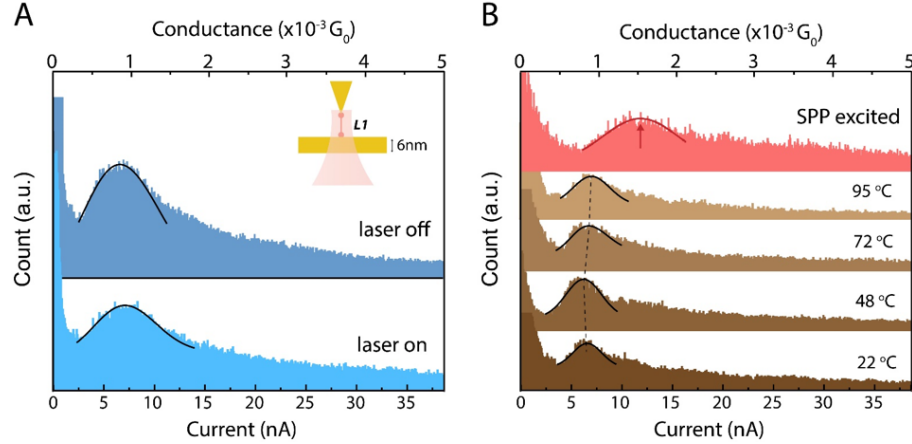
Fig. 5.3. Control measurements on bare gold film. (A) Current and conductance histograms of Au-L1-Au junctions for a voltage bias of 0.1V on a bare Au film under dark conditions and with an 830 nm laser (estimated laser power density of 0.3 mW/μm^2) illuminating the molecular junction. Inset shows the schematic of the experiment under laser illumination. (B) Current and conductance histograms of Au-L1-Au junctions at various Au film temperatures. As a guide, the histogram from the SPP excited case is also included (magenta color). The dashed line is a guide to the temperature evolution of the most probable current through L1 junctions. The measurements in (A) & (B) were performed on 6 nm-thick Au films.
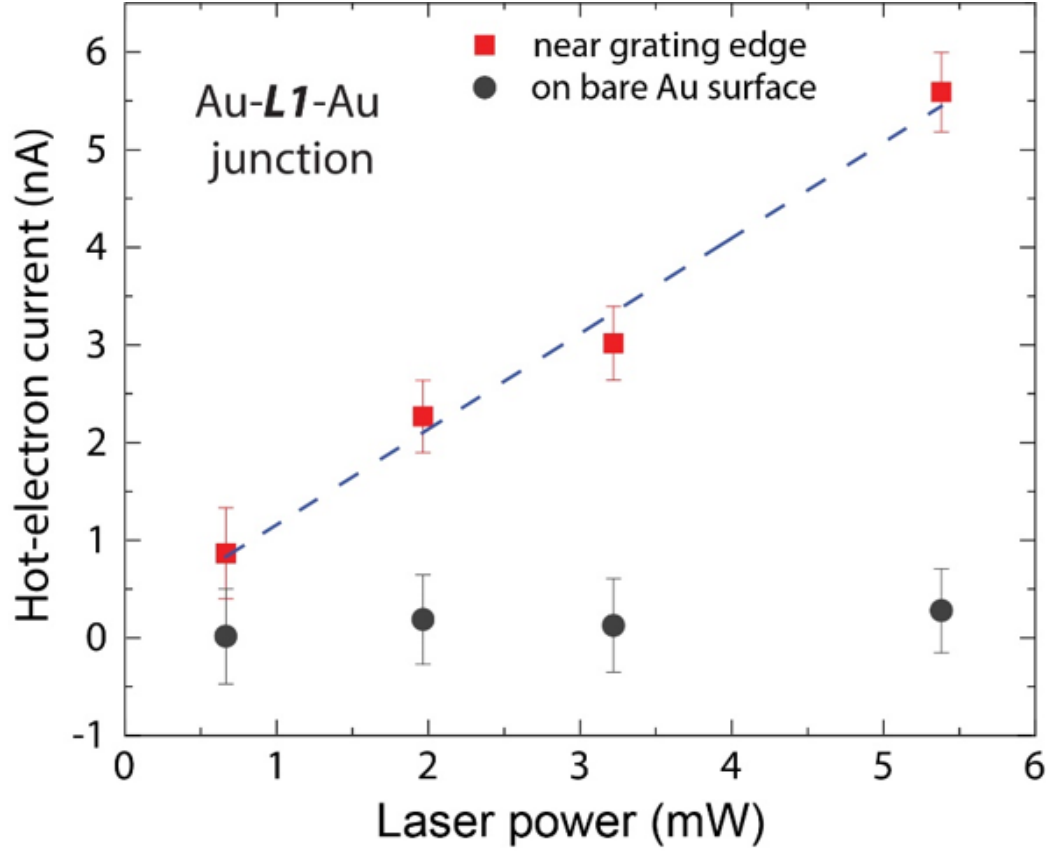
Fig. 5.4. Dependence on laser power. Measured hot-carrier current as a function of 830 nm laser power on either a bare 6 nm Au film (grey circles) or a 6 nm film with nanofabricated gratings (red squares). For the measurements on nanofabricated gratings, the grating coupler was illuminated with an 830 nm laser and the Au-L1-Au SMJs were created at separations smaller than 1 um from the edge of the gratings as described in the manuscript. The measurements on bare gold were conducted with the laser beam directly illuminating the STM probe, and thereby the L1 SMJs, as shown in the inset of Figure 5.3A. No discernable hot-carrier current was observed on bare Au at all laser powers. The dashed line is a linear fit to the measurements performed near the grating edge.

5.2 Measurement of electronic transmission function characteristics

Having established the origin of the observed deviations in the current flowing through SMJs in the presence of excited SPPs, we focused on determining the energy

distribution of hot-carriers generated in Au films. As described above (see section 4.1), we require the transmission characteristics of the SMJs to determine the spectral distribution of the hot-carriers from $I_{hot}(V)$. For this purpose, and to avoid the uncertainties associated with computational methods, we determined the transmission characteristics of L1 and H1 SMJs by employing an experimental approach developed in a recent study [57].

Briefly, an Apiezon wax-coated Au tip was used as the STM probe and SMJs were repeatedly created in a polar solvent, propylene carbonate (PC), on a 150 nm-thick template stripped gold film using break junction technique (Figure 5.5A) [36] and the current-voltage characteristics of the molecular junctions were measured. As established in prior work [68], when experiments are done in a polar solvent (PC in this case) the molecular energy level is pinned with respect to the Fermi level of the Au film on the substrate (Figure 5.5B) so that the entire voltage drop, for both positive and negative biases occurs at the STM probe-molecule junction. This pinning is due to the asymmetric electrostatic environment created between the STM probe and the gold film, which arises from the differences in the exposed area of gold film and the STM probe with the polar solvent PC. Specifically, the asymmetric environment results in the formation of a much denser double layer near the probe electrode compared to the film, which in turn leads to the above described voltage drop at the probe-molecule junction, or equivalently a bias polarity-dependent shift of the molecular junction resonance energy [57, 68].

Under such conditions, the current flowing through the SMJ is given by

$$I(V) = \frac{2e}{h} \int_{-\infty}^{\infty} T(E)\bigg(f_{eq}(E) - f_{eq}(E + eV) \bigg). \tag{5.1}$$

Assuming T = 0K (which is an excellent approximation when the applied bias is much larger than $k_B T/e \sim 25$ mV at room temperature), we can simplify the above equation as

$$I(V) = \frac{2e}{h} \int_{E_F - eV}^{E_F} T(E) dE. \tag{5.2}$$

Differentiating Eq. 5.2 with respect to V and using Leibniz integral rule we obtain

$$\frac{dI(V)}{dV} = \frac{2e^2}{h}T(E_F - eV). \tag{5.3}$$
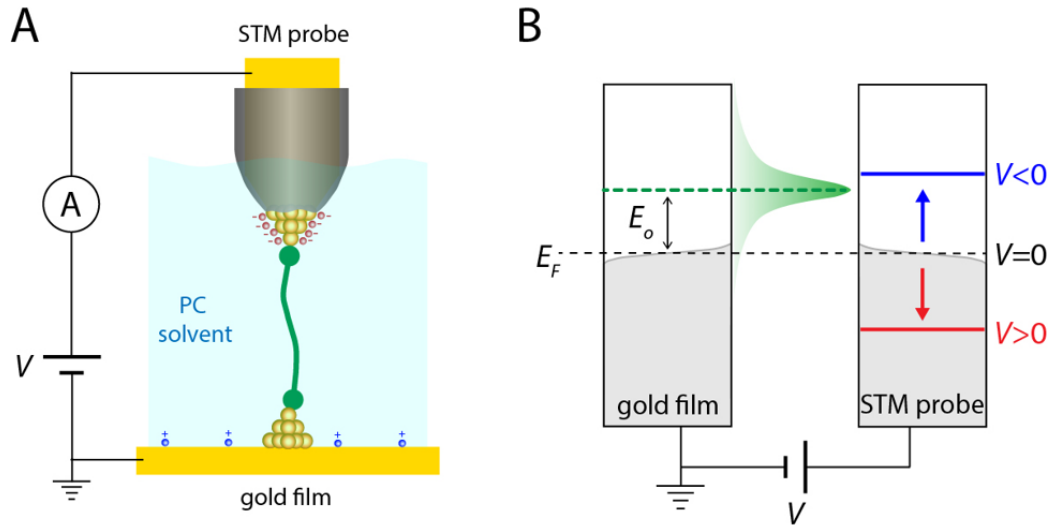
Fig. 5.5. Strategy to map the electronic transmission function of SMJs. (A) Schematic describing the approach to map the transmission function mapping. The STM probe was coated with Apiezon wax, leaving only the apex of the STM probe exposed to the polar solvent, propylene carbonate(PC). The wax coating also reduces the background capacitive and Faradaic electrochemical currents from the electrolyte. External bias was applied to the STM probe with the gold film being grounded and break junctions were repeatedly formed in the polar solvent PC. (B) Illustration of the energy diagram when a SMJ is formed between the two electrodes as shown in panel (A). The transmission function of the SMJ is indicated by the Lorentzian function in green and E_o represents the molecular resonance energy with respect to the Fermi energy E_F. Due to the PC solvent, the molecular resonance energy remains pinned to the Fermi level of the gold film, while the energy levels of the STM probe are displaced as indicated upon applying a voltage bias to the STM probe. This allows us to map the transmission characteristics of the trapped junctions.

The energy dependence of the transmission function $T(E)$ can thus be obtained from the bias dependent currents, $I(V)$, using 5.3. The measured currents at various

voltage biases flowing though L1 and H1 SMJs are shown in Figure 5.6. Due to pinning of the resonance to the substrate described above, the measured current displayed a strong bias dependence. It should be noted that the current drops as the magnitude of applied bias increases beyond a threshold voltage (-0.14V for L1 and 0.7V for H1). A similar decrease in current was previously observed in H1 [57]. The origin of this surprising current decrease was successfully attributed to changes in the local charge density of the molecular orbitals. Specifically, it was suggested that when the molecular resonance energy of the probe junctions with HOMO dominated transport approaches the chemical potential, the HOMO levels are expected to become partially unoccupied. On the other hand, for junctions with LUMO dominated levels the orbital is expected to become partially occupied. Both situations lead to polarization of the junctions. Such polarization is expected to change the transmission function (only when resonance is very close to the Fermi level of the tip) resulting in a spurious drop in the observed current.
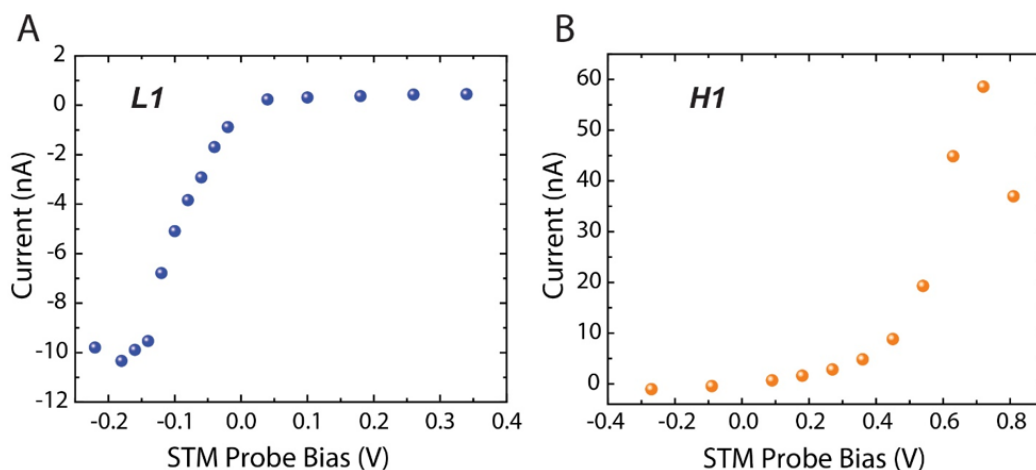
Fig. 5.6. Current-voltage characteristics of SMJs measured with Apiezon wax-coated STM probes in PC solvent. (A) & (B) Current measurements at various bias voltages in Au-L1-Au and Au-H1-Au SMJs are shown in (A) and (B), respectively.

Prior work [57] has established that the peak position of the transmission function $T(E)$ can be determined by fitting the measured $T(E)$, obtained following the experimental methods outlined above, with a Lorentzian function. We follow the same approach and fit the $T(E)$ measured on both Au-L1-Au and Au-H1-Au junctions with a Lorentzian function of the functional form shown in Equation 5.4:

$$T(E) = \frac{\Gamma^2}{(E - E_o)^2 + \Gamma^2}. \tag{5.4}$$

Here E_o and Γ are the energy of the transmission function peak relative to the Fermi energy E_F and the width of the peak, respectively. While performing the fits we only used the measured $T(E)$ data on the rising edge and excluded the measurements beyond the peak to avoid the spurious measurements from the polarization of the junctions described above [57]. Using the Lorentzian functional form, we obtained $E_0 \approx 0.18eV$ $(-0.7eV)$ and $\Gamma \approx 2.6meV$ $(6.8meV)$ for Au-L1-Au (Au-H1-Au) junctions from the least-squared fits to the measured $T(E)$ as shown in Figure 5.7A (Figure 5.7B) in the manuscript. Note that the obtained widths of the transmission function peaks are extremely narrow for both L1 and H1 junctions when compared with the energy distributions of the hot-carriers, confirming that the assumption used to arrive at Equation 4.14 (described in more detail in section 4.1) is indeed an excellent approximation.

5.3 Estimation of error bars in hot-carrier currents

We estimated the error bars associated with the hot-carrier currents from the uncertainties in the position of most probable current flowing through the SMJs. Specifically, the most probable current for a given voltage bias was obtained by first fitting the region around the peak in the current histograms with a Gaussian function. The peak of the Gaussian function fit was identified as the most probable current I, while the uncertainty in the most probable current ΔI was obtained from the 90% confidence intervals of the peak position. This process was repeated for dark and SPP

excited cases and the uncertainties in I for dark (ΔI_d) and SPP excited (ΔI_{SPP}) cases were obtained at each voltage bias. Subsequently, the error in the hot-carrier current was estimated to be $\Delta I_d + \Delta I_{SPP}$, at each bias voltage.
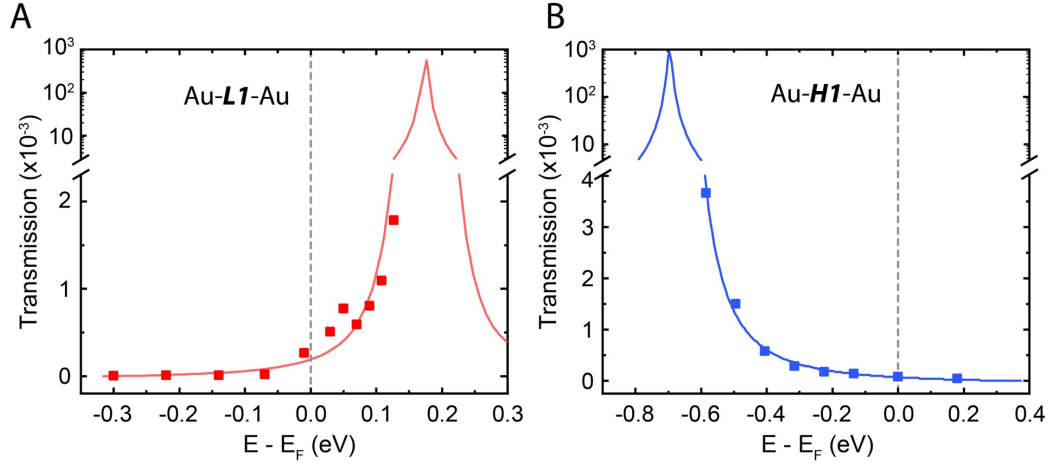
Fig. 5.7. (A) and (B): Experimentally measured transmission functions of Au-L1-Au and Au-H1-Au junctions along with the Lorentzian fits (solid lines). Dashed lines indicate the Fermi level.

6. HOT-CARRIER ENERGY DISTRIBUTIONS: EXPERIMENTAL RESULTS

Most of the material presented in this chapter is taken verbatim from the following paper: Reddy, Harsha et al. "Determining plasmonic hot-carrier energy distributions via single-molecule transport measurements", *Science*, 369 (6502), 423-426, 2020.

This chapter presents the experimental results of hot-carrier energy distributions that are generated in ultra-thin Au films due to the non-radiative decay of SPPs. The dependence of hot-carrier generation on the film thickness will also be presented

6.1   Hot-carrier energy distributions in ultra-thin Au films

Armed with the transmission characteristics, we focused on determining the energy distribution of hot-carriers generated in 6-nm thick Au films. Towards this goal, we performed additional measurements from Au-L1-Au SMJs at a location $\sim 1~\mu$m (along the x direction in Figure 4.1A) from the edge of the grating coupler, while systematically varying the voltage bias applied across the SMJs from -0.3 V to 0.3 V. The bias-dependent $I_{hot}(V)$ (see Figure 6.1A for the measured bias voltage-dependent hot-carrier current) obtained from such measurements displayed an asymmetric shape with a peak around 0.15 V.

Using the measured bias-dependent $I_{hot}(V)$ and the experimentally obtained transmission characteristics of Au-L1-Au SMJs (see Figure 5.7A) we obtained $f_{hot}(E)$ using Equation 4.14. The measured $f_{hot}(E)$ (see Figure 6.2A) revealed the relative hot-electron energy distribution, displaying a peak around 100 meV followed by a decaying tail extending up to about 330 meV above E_F. It should be noted, that as the transmission function peak enters the window between the chemical potential of the two contacts, extremely large currents flow through the molecular junction and

distort the line shape of $T(E)$ (see discussion in section 5.2 and Ref [57]). Because of this limitation, the voltage bias sweep window in L1 was restricted to {-0.3 V:0.3 V} (thus limiting the accessible energy window to {0.03 eV:0.33 eV} with respect to E_F), beyond which the distortion in the line shape prevents the reliable retrieval of $f_{hot}(E)$ (see section 5.2).
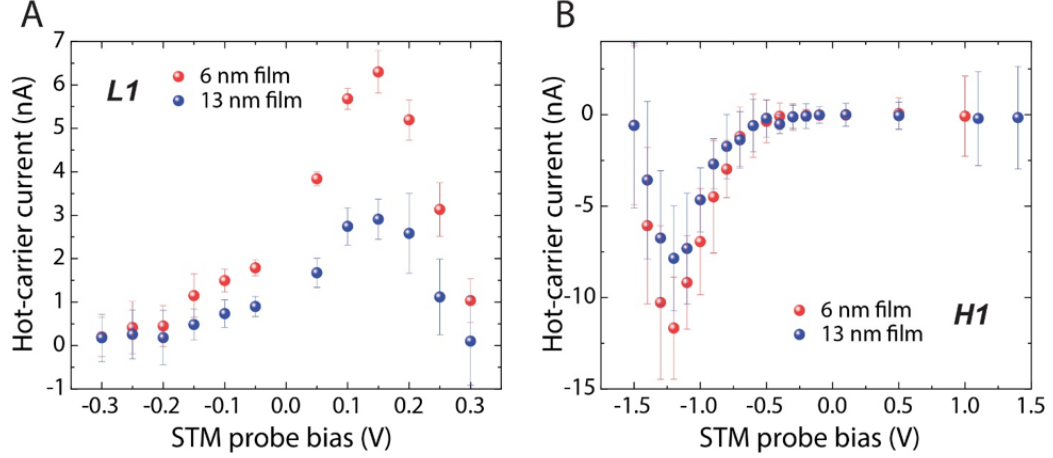
Fig. 6.1. Hot-carrier current measurements from L1 and H1 SMJs. (A) Measured hot-carrier currents flowing through Au-L1-Au SMJs for various STM probe bias voltages on 6 nm and 13 nm-thick gold films. An 830 nm continuous wave laser with an estimated power density of 0.3 mW/μm^2 (total power $\approx$ 7mW) was used to illuminate the gratings and excite SPPs. The SMJs were created at separations smaller than 1 μm from the grating edge as described in the manuscript and Figure 5.1. The error bars represent the propagated errors in the hot-carrier current that were estimated from the 90% confidence intervals of the most probable current in the molecular junctions current histograms. (B) Same as (A), but for hot-carrier currents in Au-H1-Au junctions.
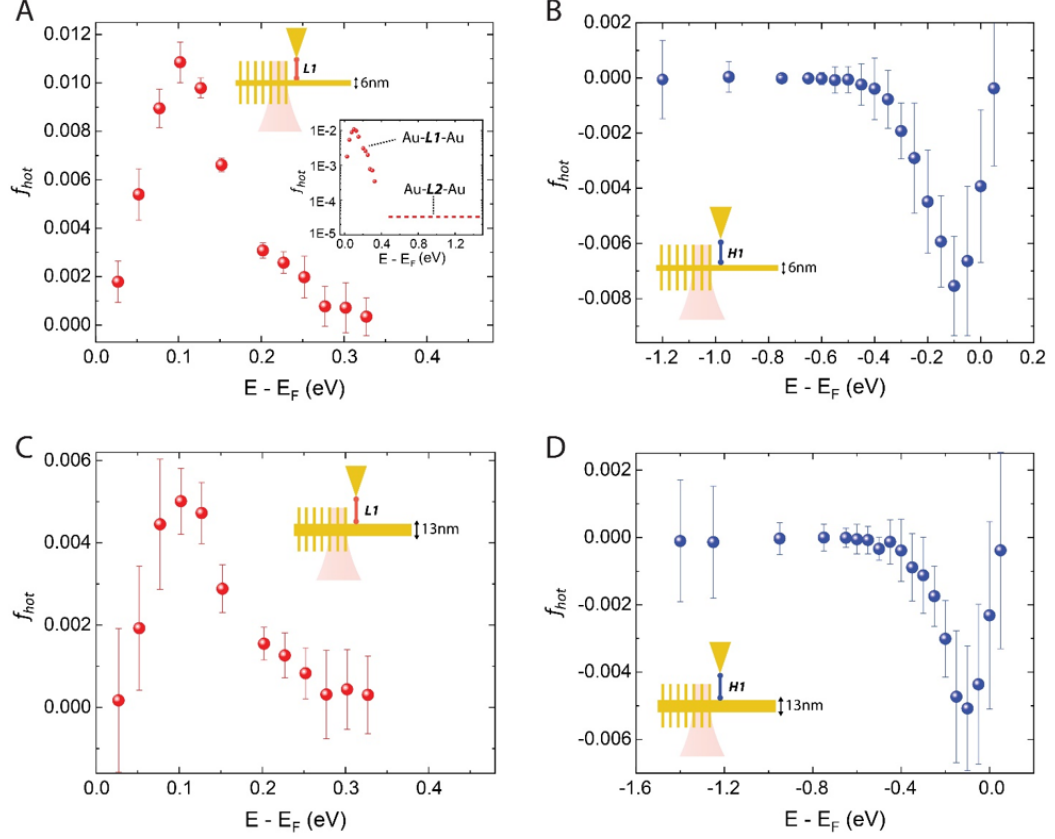
Fig. 6.2. Energy distributions of hot-carriers generated from the decay of SPPs in 6 nm and 13 nm-thick Au films. (A) The measured hot-electron energy distribution in a 6 nm Au film obtained from measurements on Au-L1-Au and Au-L2-Au molecular junctions. Note that all energies are reported relative to the Fermi level. Light from a 830 nm CW laser with electric field polarization perpendicular to grating strips is used to excite SPPs and the SMJs were created less than 1 μm from the last grating strip as depicted in the schematic. The energy distribution in the range up to 0.33 eV was measured with Au-L1-Au junctions. The inset shows the hot-electron energy distribution on a log scale and the dashed line represents the upper bound on the average $f_{hot}(E)$ in the energy window {0.4 eV:1.45 eV} as determined with Au-L2-Au junctions. (B) The measured hot-hole energy distribution in a 6 nm Au film using Au-H1-Au junctions under otherwise identical conditions compared to (A). (C) & (D) same as (A) & (B), respectively, but for a film thickness of 13 nm. The error bars correspond to the propagated errors from uncertainties in the measured hot-carrier currents.

To determine the energy distributions of hot-electrons with energies beyond 0.33 eV we performed similar measurements described above with Au-L2-Au SMJs. These measurements revealed that there are negligibly few hot-electrons with energies beyond 0.4 eV (indicated by dashed line in the inset of Figure 6.2A). These conclusions are described in more detail in the section 6.1.1 below.

6.1.1 Analysis showing that the number of hot-electrons beyond 0.4 eV are negligible

In this section, we provide an upper bound on the average of $f_{hot}(E)$ at energies beyond 0.4 eV using measurements from Au-L2-Au SMJs. For this purpose, we leveraged the computed transmission characteristics of Au-L2-Au SMJs from past work, which revealed that the $T(E)$ is negligibly small for energies -1.5 eV:0 eV compared with $T(E)$ in the energy range {0.45 eV:1.5 eV} relative to the Fermi level E_F [58] (note that the incident photon energy is ~1.5 eV, therefore $f_{hot}(E)$ is nonzero only in the energy range {-1.5 eV:1.5 eV} and zero everywhere else). Therefore, $I_{hot}(V)$ is largely determined from the hot-carriers with energy beyond E_F. Additionally, the sign of $f_{hot}(E)$ remains positive for all carriers with energies larger than E_F. Using these insights, we obtain the following inequality on Eq. 4.5, which relates $I_{hot}(V)$ and $f_{hot}(E)$ via the integral equation described in section 4.1, from integrating only over the energy subdomain {0.45 eV:1.5 eV} (all the energies are relative to E_F):

$$\frac{2e}{h}\int_{0.45eV}^{1.5eV} T(E)f_{hot}\left(E-\frac{eV}{2}\right)dE \leq I_{hot}(V). \tag{6.1}$$

We next use the computed transmission characteristics of Au-L2-Au SMJs [58] that showed that the $T(E)$ of L2 junctions is larger than 0.5 within the energy range {0.45 eV:1.5 eV}. Using this fact, we can obtain the following lower bound on the left hand side of Eq. 6.1 that holds true for Au-L2-Au SMJs

$$\frac{2e}{h} \int_{0.45eV}^{1.5eV} 0.5 f_{hot}\left(E - \frac{eV}{2}\right) dE < \frac{2e}{h} \int_{0.45eV}^{1.5eV} T(E) f_{hot}\left(E - \frac{eV}{2}\right) dE,$$

$$\implies \frac{e}{h} \int_{0.45eV}^{1.5eV} f_{hot}\left(E - \frac{eV}{2}\right) dE < \frac{2e}{h} \int_{0.45eV}^{1.5eV} T(E) f_{hot}\left(E - \frac{eV}{2}\right) dE. \tag{6.2}$$

Using Eq. 6.1 & 6.2 we get the following inequality

$$\int_{0.45eV}^{1.5eV} f_{hot}\left(E - \frac{eV}{2}\right) dE < \frac{h}{e} I_{hot}(V). \tag{6.3}$$

Finally, from the measured $I_{hot}(V_{bias} = 0.1eV)$ on L2 junctions and Eq. 6.3 an upper limit can be obtained for the average $f_{hot}(E)$ in the energy window $\{0.40$ eV:1.45 eV$\}$ $(\overline{f_{hot}(E)}_{\{0.40eV:1.45eV\}})$ as

$$\frac{\int_{0.45eV}^{1.5eV} f_{hot}(E - \frac{0.1eV}{2})}{1.05eV} = \frac{\int_{0.4eV}^{1.45eV} f_{hot}(E_2) dE_2}{1.05eV} = \overline{f_{hot}(E)}_{\{0.40eV:1.45eV\}} < \frac{\frac{h}{e} I_{hot}(0.1V)}{1.05eV}, \tag{6.4}$$

where a change of variable $E_2 = E - 0.05eV$ was used. Thus, from the measured $I_{hot}(V_{bias} = 0.1V)$ flowing through L2 SMJs on a 6 nm-thick gold film (Figure 6.3) we get

$$\overline{f_{hot}(E)}_{\{0.40eV:1.45eV\}} < 3.13 \text{ x } 10^{-5}, \tag{6.5}$$

which is over two orders of magnitude smaller than the hot-electron peak at 100 meV (dashed line in Figure 6.2A inset in the manuscript). This analysis suggests that there are negligibly few hot-electrons at energies beyond 0.4 eV.
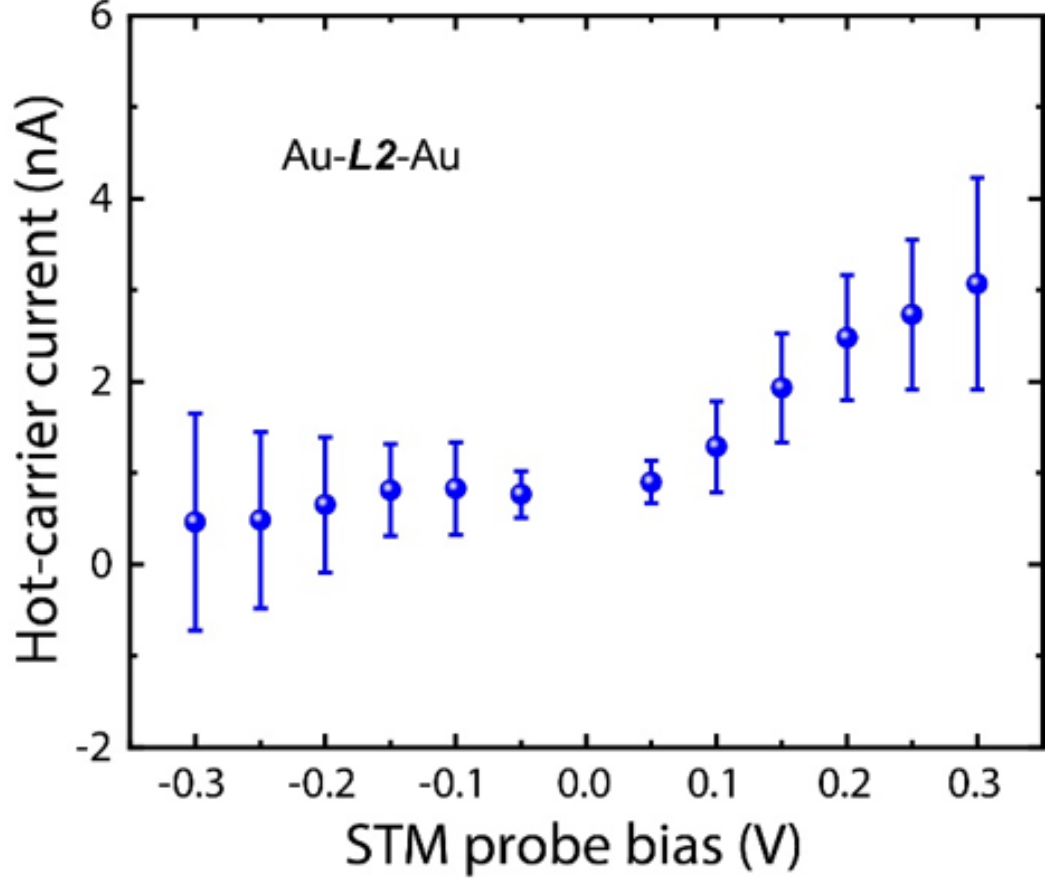
Fig. 6.3. Hot-carrier current measurements of Au-L2-Au SMJs as a function of bias voltage. These measurements were performed on a 6 nm-thick gold film with integrated grating coupler as described in the manuscript.

In order to determine the energy spectrum of hot-holes (energies below E_F), we repeated $I_{hot}(V)$ measurements on a new device with nanofabricated gratings and assembled a monolayer of molecule H1 on the Au film. The STM probe was positioned close to the grating strips as before and the $I_{hot}(V)$ flowing through Au-H1-Au SMJs was characterized for bias voltages in the range of {-1.5 V, 1 V} (see Figure 6.1B). Unlike for L1, where large hot-carrier currents were observed for positive bias voltages, no perceptible $I_{hot}(V)$ was recorded in H1 junctions for positive bias. Instead, $I_{hot}(V)$ in H1 junctions increased beyond the noise floor for negative bias voltages below -0.6 V and peaked around -1.2 V. Next, we use the measured transmission characteristics of

Au-H1-Au junctions following the approach described in section 5.2, and obtained the Lorentzian-shaped transmission characteristics shown in Figure 5.7B, which feature a peak at $E_o \approx$ -0.7 eV and a peak width of 6.8 meV, in good agreement with prior experimental work [57]. From the measured transmission function and $I_{hot}(V)$, we obtained $f_{hot}(E)$ using Equation 4.14 over the energy range {-1.2 eV,0.05 eV}—the energy spectrum of hot-holes (Figure 6.2B). The hot-hole energy spectrum featured a peak around -0.1 eV and a decaying tail that extends to energies about -0.4 eV with respect to the Fermi level (E_F).

Next, to understand the effect of film thickness on hot-carrier generation we performed all the measurements described above on thicker, 13 nm-thick Au films. The measured distribution (see Figure 6.2C & D), obtained following the same methods described above, showed that the hot-carriers are mostly populated close to the Fermi level. Besides, the total number of hot-carriers (sum of hot-electrons and hot-holes, $\int_{E_F-\hbar\omega}^{E_F+\hbar\omega} |f_{hot}(E)|dE$) was found to be about 40% smaller than those measured on 6 nm-thick Au film. In the next chapter we will employ density functional theory (DFT) calculations to compute the hot-carrier generation rates and combined them with the Boltzmann transport equation under the relaxation time approximation to obtain the steady-state distribution of hot-carriers. These calculations will be used to identify the underlying physical mechanisms governing the hot-carrier generation and the suitable frameworks for the relaxation rates that best describe our experimental observations.

6.2 Acknowledgements

I would like to acknowledge my colleague Dr. Kun Wang who meticulously contributed to the single molecule transport measurements presented in this chapter.

7. THEORETICAL ESTIMATES OF HOT-CARRIER DISTRIBUTIONS

Most of the material presented in this chapter is taken verbatim from the following paper: Reddy, Harsha et al. "Determining plasmonic hot-carrier energy distributions via single-molecule transport measurements", *Science*, 369 (6502), 423-426, 2020.

This chapter presents the *ab initio* theoretical framework that enabled the estimation of hot-carrier distributions. We will discuss competing theoretical frameworks and by comparing with our experimental findings from **Chapter 6**, we identify the theoretical approach that best describes our experimental findings. The fundamental role of Landau damping to hot-carrier generation will be discussed. Finally, the contributions of different plasmonic modes towards hot-carrier generation will also be presented and together with experiments and electromagnetic field profile simulations, the dominant contributors to hot-carrier generation will be identified.

7.1 Formalism employed for computing the steady-state hot-carrier distributions

To compute the steady-state hot-carrier distributions in our gold films and to gain insights into the microscopic origin of the experimental observations described in the previous chapter, we employed state-of-the-art first-principle density functional theory (DFT) calculations to estimate the hot-carrier generation rates and combined them with the Boltzmann transport equation under the relaxation time approximation to obtain the steady-state distribution of hot-carriers. Specifically, we first estimated the generation rates of hot-carriers employing an *ab initio* method based on Fermi's golden rule. Briefly, we first calculated the generation rates of hot-carriers that arise from the decay of SPPs in a thin film of gold surrounded by a dielectric

with a refractive index n = 1.45, mimicking the geometry in our experiments (see Figure 7.1). To compute these generation rates, we built upon the formalism developed in [30]. For the benefit of the reader, we summarize the key arguments from previous works [30,69] below (Eq. 7.1–7.18). Specifically, in this formalism the SPP is treated quantum mechanically using the exact quantization of the surface modes [69]. The vector potential of SPP is given by $A(r,t) = \sum_k [\overline{u}_k(r,t)\hat{a}_k + \overline{u}_k^\dagger(r,t)\hat{a}_k^\dagger]$, where $\hat{a}_k$ and $\hat{a}_k^\dagger$ are annihilation and creation operators of surface plasmons, while k and $\overline{u}_k(r,t))$ represent the wavevector of SPP, and the electric field mode profile, respectively. As is well known, the symmetric geometry considered here supports two SPP modes—a symmetric mode and an anti-symmetric mode [70,71]. As depicted in Figure 7.1, we define the symmetric (anti-symmetric) mode with respect to the mode profile of the electric field along the propagation direction (E_x).
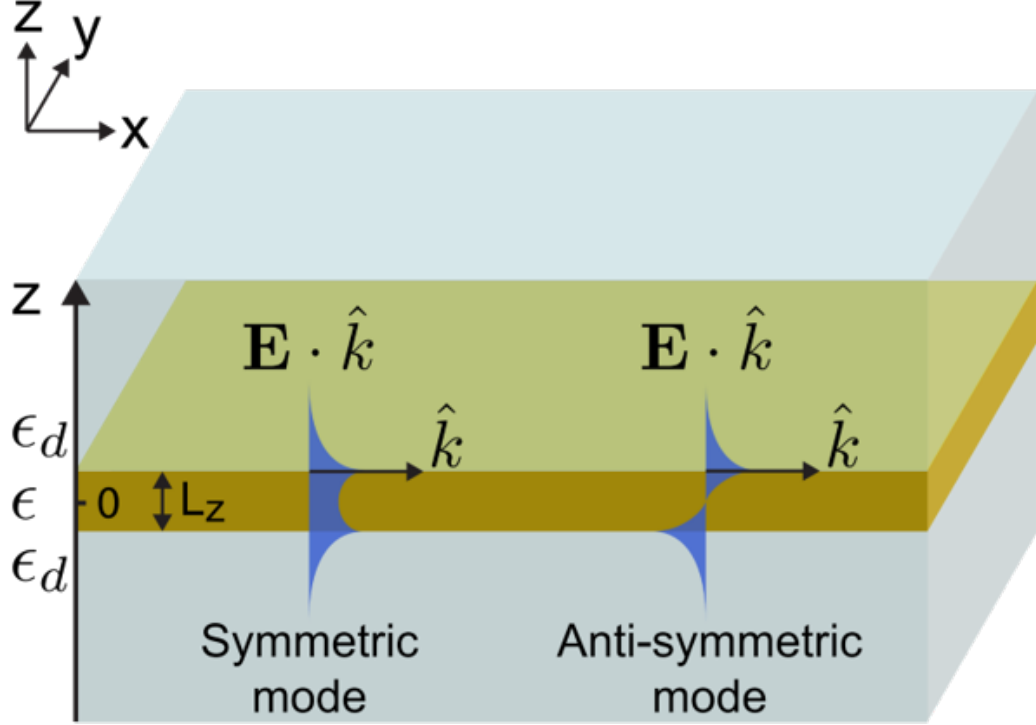
Fig. 7.1. Schematic of the geometry considered and the supported surface plasmon modes. The symmetric (anti-symmetric) mode refers to the mode with the electric field component along the propagating direction being symmetric (anti-symmetric) relative to the xy plane at z = 0. L_z, and ϵ_d represent the thickness of the gold film and the permittivity of the surrounding dielectric medium, respectively.

For the symmetric mode on a gold film of thickness L_z we have the normalized mode function as

$$\overline{u}_k^{sym}(r,t) = \sqrt{\frac{2\pi\hbar}{\omega L_{sym}(\omega)S}} e^{i(\overline{k}.\overline{r}-\omega t)} \, \overline{u}_k^{sym0}(z), \tag{7.1}$$

$$\overline{u}_k^{sym0}(z) = e^{-\gamma_{out}(|z|-\frac{L_z}{2})}\left(\hat{k} + \hat{z}\frac{ik}{\gamma_{out}}sign(z)\right), \text{ for } |Z| > \frac{L_z}{2} \tag{7.2}$$

$$\overline{u}_k^{sym0}(z) = \hat{k}\frac{cosh(\gamma_{in}z)}{cosh(\gamma_{in}\frac{L_z}{2})} - \hat{z}\frac{ik}{\gamma_{in}}\frac{sinh(\gamma_{in}z)}{cosh(\gamma_{in}\frac{L_z}{2})} \text{ for } |Z| \le \frac{L_z}{2} \tag{7.3}$$

while for the anti-symmetric mode

$$\overline{u}_k^{asym}(r,t) = \sqrt{\frac{2\pi\hbar}{\omega L_{asym}(\omega)S}} e^{i(\overline{k}.\overline{r}-\omega t)} \, \overline{u}_k^{asym0}(z), \tag{7.4}$$

$$\overline{u}_k^{asym0}(z) = e^{-\gamma_{out}(|z|-\frac{L_z}{2})}\left(\hat{k}sign(z) + \hat{z}\frac{ik}{\gamma_{out}}\right), \text{ for } |Z| > \frac{L_z}{2} \tag{7.5}$$

$$\overline{u}_k^{asym0}(z) = \hat{k}\frac{sinh(\gamma_{in}z)}{sinh(\gamma_{in}\frac{L_z}{2})} - \hat{z}\frac{k}{\gamma_{in}}\frac{cosh(\gamma_{in}z)}{sinh(\gamma_{in}\frac{L_z}{2})} \text{ for } |Z| \le \frac{L_z}{2} \tag{7.6}$$

Here, $\gamma_{out} = \sqrt{k^2 - \epsilon_d\omega^2/c^2}$ and $\gamma_{in} = \sqrt{k^2 - \epsilon\omega^2/c^2}$ where ϵ_d and $\epsilon(\omega)$ are the dielectric permittivity of the surrounding environment and Au film, respectively. The unit vector $\hat{k}$ points in the x direction. We use the Brendel-Bormann model in ref [72] for $\epsilon(\omega)$ of our Au film, while for the surrounding medium we use $\epsilon_d = n^2$ with n= 1.45. By enforcing the continuity of $\overline{E}.\hat{k}$ and $\overline{H}.\hat{k}$ across the interface, we arrive at the following dispersion relations for the symmetric and anti-symmetric modes

$$k_{sym} = \frac{\omega}{c}\sqrt{\epsilon_d + \frac{\epsilon_d - \epsilon(\omega)}{\left[\frac{\epsilon(\omega)}{\epsilon_d}\right]^2 tanh^2\left(\gamma_{in}\frac{L_z}{2}\right) - 1}}, \tag{7.7}$$

$$k_{asym} = \frac{\omega}{c}\sqrt{\epsilon_d + \frac{\epsilon_d - \epsilon(\omega)}{\left[\frac{\epsilon(\omega)}{\epsilon_d}\right]^2 coth^2\left(\gamma_{in}\frac{L_z}{2}\right) - 1}}. \tag{7.8}$$

In the modal functions described above, $L_{sym}(\omega)$ and $L_{asym}(\omega)$ are chosen such that the electromagnetic energy of the plasmon mode in the volume corresponding to a transversal area S in the xy plane (the volume includes $-\infty < z < \infty$), is a single quantum, $\hbar\omega$. This gives

$$L_{sym}(\omega) = \frac{[(\gamma_{in}^2 + k^2)sinh(\phi) + (\gamma_{in}^2 - k^2)\phi]\frac{d(\omega\epsilon)}{d\omega} + (\epsilon\frac{\omega}{c})^2[sinh(\phi) - \phi]}{2\gamma_{in}^3[cosh(\phi) + 1]}$$

$$+ \frac{(\gamma_{out}^2 + k^2)\frac{d(\omega\epsilon_d)}{d\omega} + (\epsilon_d\frac{\omega}{c})^2}{2\gamma_{out}^3}, \tag{7.9}$$

$$L_{asym}(\omega) = \frac{[(\gamma_{in}^2 + k^2)sinh(\phi) + (\gamma_{in}^2 - k^2)\phi]\frac{d(\omega\epsilon)}{d\omega} + (\epsilon\frac{\omega}{c})^2[sinh(\phi) + \phi]}{2\gamma_{in}^3[cosh(\phi) - 1]}$$

$$+ \frac{(\gamma_{out}^2 + k^2)\frac{d(\omega\epsilon_d)}{d\omega} + (\epsilon_d\frac{\omega}{c})^2}{2\gamma_{out}^3}, \tag{7.10}$$

where $\phi = \gamma_{in}L_z$.

Next, the electronic wave functions in the gold film were determined using density functional theory in an open-source plane-wave electronic density functional software package—JDFTx [73]. For this purpose, a full relativistic PBEsol+U generalized-gradient approximation [74] with U = 2.04 eV [75] on each gold atom was used. This approach has been shown to provide a good agreement to quasiparticle band structure [30], which we also confirmed.

Owing to the nanoscale confinement along the thickness direction in our thin Au film, the electronic wave functions in the thin film case can be substantially different from the bulk case. However, the optically thin film still contains many electrons, making it computationally demanding to directly solve for the electronic wave functions. To circumvent this computational constraint, we employed an ab initio tight-binding-like approach to construct the Hamiltonian of electrons in the Au film. Specifically, in this approach maximally-localized Wannier functions [76,77] were generated for a unit cell in the bulk crystal using 10^3 samples in the first Brillouin zone,

$$w_a^\sigma(\bar{r} - \overline{R}) = \frac{1}{N_q} \sum_{qb} U_{ab}^q e^{i\bar{q}.(\bar{r} - \overline{R})} \psi_{qb}^\sigma(\bar{r}). \tag{7.11}$$

Here, U_{ab}^q are the unitary rotations that minimize the spatial variance of $w_a^\sigma(\bar{r} - \overline{R})$, $\psi_{qb}^\sigma(\bar{r})$ are the eigenfunctions of the bulk crystal with energies ϵ_{qb}, N_q is the sampling number in the first Brillouin zone of the bulk crystal which equals 1000, and the subscripts a and b denote the orbitals. The Hamiltonian in the basis of the maximally-localized Wannier functions can then be derived as

$$H_{\overline{R}a,\overline{R}'a'} = \frac{1}{N_q}\sum_{qb} U_{ab}^{q*}U_{a'b}^{q}e^{i\overline{q}.(\overline{R}-\overline{R}')}\epsilon_{qb}. \tag{7.12}$$

Since $H_{\overline{R}a,\overline{R}'a'}$ is represented in the basis of maximally-localized Wannier functions, it decays rapidly as $|\overline{R}-\overline{R}'|$ — increases. This allows us to truncate it after a few sites and construct the Hamiltonian of the whole film by considering only those terms that are associated with atoms in the film and excluding all other terms. Furthermore, we take advantage of the periodicity of the film in the transverse directions—xy plane (we consider xy plane as the (111) plane of the bulk crystal)—and employ the Bloch theorem for the two transverse directions. The Hamiltonian constructed accordingly for the whole film was then diagonalized, which leads to the following eigenfunctions:

$$\psi_{\overline{q}n}^{\sigma} = \sum_{a\overline{R}} C_{\overline{q}naZ}e^{i\overline{q}.\overline{R}}w_a^{\sigma}(\overline{r}-\overline{R}), \tag{7.13}$$

with eigenenergies $\epsilon_{\overline{q}n}$. Here $\overline{q}$ is a wave vector in the two-dimensional Brillouin zone. The coefficients $C_{\overline{q}naZ}$ are obtained from the diagonalization of the constructed Hamiltonian of the whole film.

The eigenfunctions determined above were next used in conjunction with Fermi's golden rule to obtain the plasmon decay rate. To be consistent with the usual convention used in second quantization, we denote $\hat{c}_{\overline{q}n}$ ($\hat{c}_{\overline{q}n}^{\dagger}$) as the Fermionic annihilation (creation) operator. The initial state of the system contains a single surface plasmon with wavevector $\overline{k}$ and a Fermi sea of electrons. This state is denoted as $|\overline{k}\rangle = \hat{a}_{\overline{k}}^{\dagger}|0\rangle$, where $|0\rangle$ represents a system composed of just the Fermi sea and no surface plasmon. The final state of the system is represented as $|\overline{q}'n',\overline{q}n\rangle = \hat{c}_{\overline{q}'n'}^{\dagger}\hat{c}_{\overline{q}n}|0\rangle/\sqrt{(1-f_{\overline{q}'n'})f_{\overline{q}n}}$, where $\overline{q}(\overline{q}')$ and $n(n')$ denote the electron wave vector and the band index, respectively, for the initial(excited) electronic level. Here f represents the Fermi-Dirac distribution at 300 K.

We approximate the plasmon-quasiparticle interaction Hamiltonian as $\hat{H}_{int} = \sum_{\sigma}\int dr\psi_{\sigma}^{\dagger}\left(\frac{e}{2m_e}\hat{A}.\hat{p}\right)\psi_{\sigma}$, with $\hat{p} = \frac{\hbar}{i}\nabla$ being the electronic momentum operator. Using the Fermi's golden rule, the decay rate of the surface plasmon is given by

$$\Gamma = \frac{2\pi}{\hbar} \sum_{\bar{q}n'\bar{q}n} \delta(\epsilon_{\bar{q}n'} - \epsilon_{\bar{q}n} - \hbar\omega)|M_{\bar{q}'n',\bar{q}n}|^2, \tag{7.14}$$

where the transition matrix element is

$$M_{\bar{q}'n',\bar{q}n} = \left\langle \bar{q}'n', \bar{q}n \middle| \hat{H}_{int} \middle| \bar{k} \right\rangle = \left\langle \bar{q}'n', \bar{q}n \middle| \frac{e}{2m_e} \sum_\sigma \int dr \Psi_\sigma^\dagger \hat{A}.\hat{p}\hat{\Psi}_\sigma \middle| \bar{k} \right\rangle$$

$$= \sqrt{(1-f_{\bar{q}'n'})f_{\bar{q}n}} \frac{e}{2m_e} \frac{\Omega_{||}}{S} \sum_\sigma \int dr \psi_{\bar{q}'n'}^{\sigma*}(r) \overline{u}_k(r,0). \frac{\hbar\nabla}{i} \psi_{\bar{q}n}^\sigma(r). \tag{7.15}$$

Here, $\Omega_{||}$ is the area of the two-dimensional unit cell. The derivation above uses the electron field operator as $\hat{\Psi}_\sigma(r,t) = \sum_{\bar{q}n} \psi_{\bar{q}n}^\sigma(r)e^{-i\epsilon_{\bar{q}n}t/\hbar}\hat{c}_{\bar{q}n}$. By assuming that the plasmon field profile varies slowly on the atomic scale in the two transversal directions, the plasmon decay rate can be rewritten as:

$$\Gamma_{sym/asym} = \frac{\pi^2\hbar^2e^2}{m_e^2\omega L_{sym/asym}} \sum_{n'n} \int_{FBZ} \frac{d\bar{q}}{4\pi^2} \delta(\epsilon_{\bar{q}n'} - \epsilon_{\bar{q}n} - \hbar\omega)(1-f_{\bar{q}n'})f_{\bar{q}n}$$

$$\cdot \left| \sum_{a'aZ'Z} C_{\bar{q}n'a'z'}^* C_{\bar{q}naZ} \overline{u}_k^{sym0/asym0}\left(\overline{z}_{a'a}^{z'z}\right). \sum_{\overline{R}_{||}} e^{i\bar{q}.\overline{R}_{||}} <i\nabla>_{a'aZ'Z}^{\overline{R}_{||}} \right|^2. \tag{7.16}$$

Here, $\overline{z}_{a'a}^{z'z}$ is the z-center of the product density of the maximally-localized Wannier basis functions indexed by aZ and $a'z'$, and FBZ denotes the first Brillouin zone of the reciprocal lattice of the two-dimensional lattice. Using the above decay rates, the generation rate of the hot-electrons with an electronic energy level $\epsilon_{\bar{q}'n'}$ can be written as:

$$G_{e,sym/asym} = \frac{\pi^2\hbar^2e^2}{m_e^2\omega L_{sym/asym}} \sum_n \int_{FBZ} \frac{d\bar{q}}{4\pi^2} \delta(\epsilon_{\bar{q}n'} - \epsilon_{\bar{q}n} - \hbar\omega)(1-f_{\bar{q}n'})f_{\bar{q}n}$$

$$\cdot \left| \sum_{a'aZ'Z} C_{\bar{q}n'a'z'}^* C_{\bar{q}naZ} \overline{u}_k^{sym0/asym0}\left(\overline{z}_{a'a}^{z'z}\right). \sum_{\overline{R}_{||}} e^{i\bar{q}.\overline{R}_{||}} <i\nabla>_{a'aZ'Z}^{\overline{R}_{||}} \right|^2. \tag{7.17}$$

while the generation rate of hot-holes with an electronic energy level of $\epsilon_{\bar{q}n}$ is given by

$$G_{h,sym/asym} = \frac{\pi^2 \hbar^2 e^2}{m_e^2 \omega L_{sym/asym}} \sum_{n'} \int_{FBZ} \frac{d\bar{q}}{4\pi^2} \delta(\epsilon_{\bar{q}n'} - \epsilon_{\bar{q}n} - \hbar\omega)(1 - f_{\bar{q}n'})f_{\bar{q}n}$$

$$\cdot \left| \sum_{a'aZ'Z} C^*_{\bar{q}n'a'z'} C_{\bar{q}naZ} \overline{u}_k^{sym0/asym0} \left(\overline{z}^{z'z}_{a'a} \right) \cdot \sum_{\overline{R}_{||}} e^{i\bar{q}.\overline{R}_{||}} < i\nabla >^{\overline{R}_{||}}_{a'aZ'Z} \right|^2. \qquad (7.18)$$

The hot-carrier generation rates computed employing the above described formalism with a Monte Carlo sampling of 15 million random $\bar{q}$ in the first Brillion zone of the two-dimensional lattice on 6 nm and 13 nm-thick Au films are shown in Figure 7.2.
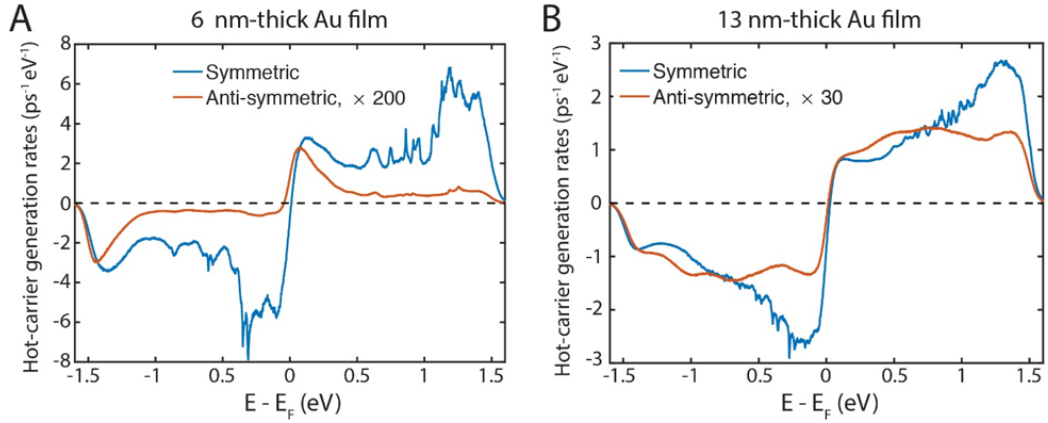
Fig. 7.2. Hot-carrier generation rates. (A) Hot-carrier generation rates in a 6 nm-thick gold film computed using the formalism outlined above. The computed generation rates for both symmetric and anti-symmetric plasmonic modes are shown. Note that the generation rates of the anti-symmetric mode have been scaled up by a factor of 200. (B) Same as in (A) but for a 13 nm-thick Au film. In this case, the anti-symmetric mode has been scaled up 30-times.

Armed with the generation rates (G(E)), we next focused on obtaining the steady state hot-carrier distributions ($f_{hot}(E)$) using Boltzmann transport equation (BTE).

Neglecting the spatial variations and under the absence of any external DC electric field the BTE simplifies as [78]

$$\frac{\partial f_{ne}(E)}{\partial t} = \frac{\partial f_{ne}(E)}{\partial t}\bigg|_{coll} + G(E). \tag{7.19}$$

Here $f_{ne}(E)$ is the non-equilibrium distribution function and $\frac{\partial f_{ne}(E)}{\partial t}\big|_{coll}$ encompasses the rate of change of $f_{ne}(E)$ due to electron-electron and electron-phonon collisions. We can therefore rewrite $\frac{\partial f_{ne}(E)}{\partial t}\big|_{coll}$ as

$$\frac{\partial f_{ne}(E)}{\partial t}\bigg|_{coll} = \frac{\partial f_{ne}(E)}{\partial t}\bigg|_{e\phi} + \frac{\partial f_{ne}(E)}{\partial t}\bigg|_{ee}, \tag{7.20}$$

where $\frac{\partial f_{ne}(E)}{\partial t}\big|_{e\phi}$ and $\frac{\partial f_{ne}(E)}{\partial t}\big|_{ee}$ represent the electron-phonon and electron-electron scattering rates, respectively. Furthermore, under continuous wave illumination, as is the case in our experiments, the distribution of hot-carriers is invariant with time. Under such steady state conditions, the left hand side in Eq. 7.19 goes to zero simplifying Eq. 7.19 as

$$-\frac{\partial f_{ne}(E)}{\partial t}\bigg|_{coll} = -\frac{\partial f_{ne}(E)}{\partial t}\bigg|_{e\phi} - \frac{\partial f_{ne}(E)}{\partial t}\bigg|_{ee} = G(E). \tag{7.21}$$

A rigorous approach to model these scattering rates involves Fermi's golden rule with matrix elements that are to be obtained from appropriate Hamiltonians describing the relevant scattering processes as shown in the following equation [78, 79]:

$$\frac{\partial f}{\partial t}\bigg|_{coll} = \sum_{n'} f(E_{n'})(1 - f(E_n))s_{n',n}^{coll} - f(E_n)(1 - f(E_{n'}))s_{n,n'}^{coll}, \tag{7.22}$$

where $s_{n',n}^{coll}$ are the matrix elements of the scattering processes.

While this approach is exact, it requires an enormous amount of computational power. An alternative approach is to adopt the relaxation time approximation (RTA) that circumvents the requirement of enormous computational resources [34, 78, 79]. Within the framework of RTA, the electron-phonon and electron-electron collision rates can be approximated as

$$\left.\frac{\partial f_{ne}(E)}{\partial t}\right|_{e\phi} + \left.\frac{\partial f_{ne}(E)}{\partial t}\right|_{ee} = -\frac{f_{ne}(E) - f_e(E)}{\tau_{e\phi}} - \frac{f_{ne}(E) - f_e(E)}{\tau_{ee}}, \tag{7.23}$$

$$\implies \left.\frac{\partial f_{ne}(E)}{\partial t}\right|_{coll} = -\frac{f_{hot}(E)}{\tau_{e\phi}} - \frac{f_{hot}(E)}{\tau_{ee}}, \tag{7.24}$$

where $f_e(E)$ and $f_{hot}(E)$ are the equilibrium and hot-carrier energy distribution functions as before (see discussion in section 4.1), and $\tau_{e\phi}$ and τ_{ee} are the characteristic electron-phonon and electron-electron relaxation times, respectively. Using Eq. 7.24, Eq. 7.21 can be rewritten as

$$G(E) = \frac{f_{hot}(E)}{\tau_{eff}}, \tag{7.25}$$

where $\frac{1}{\tau_{eff}} = \frac{1}{\tau_{e\phi}} + \frac{1}{\tau_{ee}}$. Thus, $f_{hot}(E)$ can be obtained from the computed generation rates and the relaxation times $\tau_{e\phi}$ and τ_{ee}, using Eq. 7.25. Furthermore, it is evident that $f_{hot}(E)$ depends on the choice of $\tau_{e\phi}$ and τ_{ee}.

We treat $\tau_{e\phi}$ as a constant energy-independent relaxation time. Prior experimental work has estimated $\tau_{e\phi}$ to be about 0.8 ps in Au [80], and we use the same number in our calculations. For the electron-electron relaxation time τ_{ee}, we consider the two widely used approaches. One approach treats τ_{ee} as a single energy-independent relaxation time [31, 33] , similar to $\tau_{e\phi}$. With this simple approach, the hot-carrier energy distribution is given by

$$f_{hot}(E) = G(E) * \tau_{eff} \tag{7.26}$$

Note that since τ_{eff} is a constant in this framework $f_{hot}(E)$ has the same energy dependence as the generation rates $G(E)$.

The second popular approach approximates τ_{ee} to be energy-dependent [34, 79]. Specifically, within the framework of Landau's Fermi-liquid theory (FLT) [81], τ_{ee} takes the following functional form:

$$\tau_{ee}(E) = (K((\pi K_B T)^2 + (E - E_F)^2))^{-1}, \tag{7.27}$$

here $K = m^{*}_{eff}{}^{3}/8\pi^{4}\hbar^{6}W_{ee}$ is a material dependent constant that contains the electron effective mass m^{*}_{eff} and the averaged angular scattering probability W_{ee}. For gold it has been estimated that $K = 2 \times 10^{14}/eV^{2}s$ [34]. While using the energy dependent τ_{ee} from FLT, we adopt the semi-quantitative approach described in [79] that conserves the electronic energy and charge. The central equations of this approach are shown below:

$$G(E) = \frac{f_{hot}(E)}{\tau_{eff}}, \text{ when } |E - E_{F}| > E_{crit}, \tag{7.28}$$

$$G(E) = \frac{f_{hot}(E)}{\tau_{eff}} - F_{gen}(E), \text{ when } |E - E_{F}| < E_{crit}, \tag{7.29}$$

$$F_{gen}(E) = \left(\frac{Q_{eff}}{\alpha.K_{B}T_{eff}.DOS_{F}}\right)\frac{1}{K_{B}}\frac{\partial f_{e}(E, T_{eff})}{\partial T}, \tag{7.30}$$

$$\text{where } Q_{eff} = \sum_{|E_{n}-E|>E_{crit}} E_{n}.G_{n}\left(\frac{\tau_{ee}(E_{n})}{\tau_{ee}(E_{n}) + \tau_{e\phi}}\right). \tag{7.31}$$

This approach includes an additional generation term $F_{gen}(E)$, for carriers with energies below a critical energy E_{crit}. This additional generation term accounts for the in-scattering of carriers generated at high energies. We use the same form of ansatz for $F_{gen}(E)$ proposed in [79] and vary the parameter α to conserve the total charge of hot-carriers ($\int_{-\infty}^{\infty} f_{hot}(E)dE = 0$). The parameter T_{eff} represents the effective temperature of hot-carriers, and DOS_{F} corresponds to the density of states near the Fermi level. In our calculations, we keep T_{eff} at 800 K and set $E_{crit} = 0.4eV$. As described in [79] , despite having some uncertainty in the choice of the free parameters α, T_{eff} and E_{crit}, the presented simple approach enables a good estimate of the steady-state hot-carrier distributions.

The computed hot-carrier distributions arising from the symmetric plasmonic mode on a 6 nm-thick Au film, obtained using both an energy-dependent electron-electron collision rate from Landau's Fermi liquid theory (FLT) [81] and an energy-independent scattering rate are shown in Figure 7.3A. Note that these computational

results are multiplied by a scaling factor so that the peak value is 1. It can be seen that the energy spectrum of the hot-carriers that we computed by employing energy-dependent collision rates from FLT shows that most of the hot-carriers are populated within the energy window of {-0.4 eV : 0.4 eV} relative to the Fermi level, and negligibly few carriers are present at higher energies—in excellent agreement with our experiments. In contrast, an energy-independent scattering rate produces hot-carriers at all energies (Figure 7.3A, blue curve), in stark difference with our experimental observations. Taken together, the close agreement between our experimental findings and the computed energy distribution with the scattering rates from FLT establishes the validity of employing the energy-dependent electron-electron collision rates to model the energy spectrum of hot-carriers in plasmonic nanostructures.
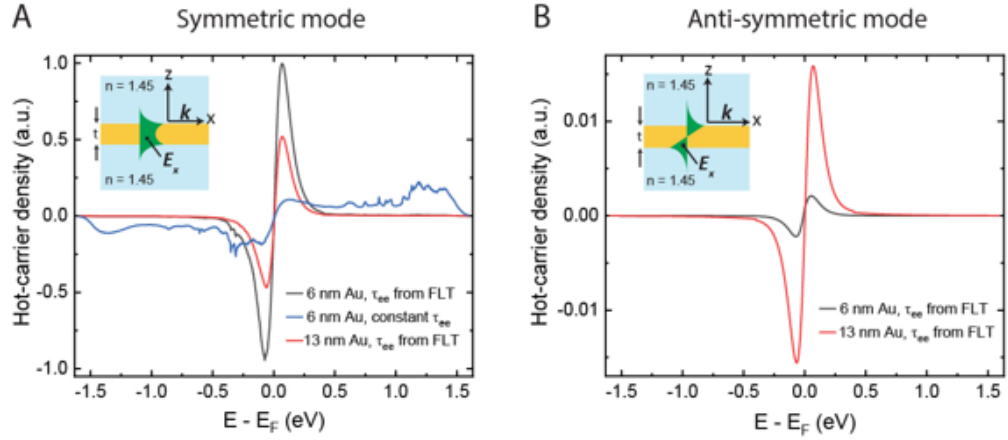
Fig. 7.3. Computed hot-carrier energy distributions, distance dependence and intensity profile. (A) Computed steady-state energy distribution of hot-carriers in 6 nm- and 13 nm-thick Au films, arising from the symmetric plasmonic mode. The inset shows the geometry considered in these calculations along with the symmetric mode profile. The computed distributions with electron-electron scattering rates from either Fermi liquid theory (FLT) or an energy-independent scattering rate are shown. (B) Same as (A), but for the anti-symmetric plasmonic mode. Note that the y-axis scale is smaller in (B) compared to (A).

Next, to understand the effect of film thickness on hot-carrier generation we performed all the calculations described above on thicker, 13 nm-thick Au films. The measured distribution (see Figure 7.3 (red curve)), obtained following the same methods described above, revealed that the hot-carriers are mostly populated close to the Fermi level. The observed reduction in the hot-carrier generation rates with the film thickness can be attributed to the effect of surface-assisted absorption—Landau damping—associated with hot-carrier generation. These computational results are shown in Figure 7.3A (red curve). For comparison purposes, we scaled these results by the same scaling factor from 6 nm symmetric mode case. As evident from Figure 7.3A, the generated hot-carriers are populated close to the Fermi level, similar to the 6 nm-thick Au film. However, about 43% fewer hot-carriers (sum of hot-electrons and hot-holes) are generated in the 13 nm-thick gold film, in good agreement with our experiments. The reduction in hot-carrier numbers can be understood from Figure 7.2, where we show that the hot-carrier generation rates from a symmetric plasmonic mode in a 13 nm-thick Au film are smaller compared to their 6 nm-thick counterparts. Owing to the smaller film thickness, the reflection and backscattering of tightly confined electrons from the surfaces of the 6 nm film efficiently break the linear momentum conservation of electrons [33]. These effects lead to larger amplitudes for the generation of carriers from the Fermi sea to excited energy levels in the 6 nm film compared to the 13 nm film—a manifestation of Landau damping [4,33,60]. The reduced Landau damping along with the lower propagation loss of the symmetric SPP mode in the 13 nm film lead to reduced generation rates, which in turn decrease the number of generated hot-carriers. Overall, the excellent agreement between our experiments and computations provides additional support for the validity of our experimental approach.

7.2 Distance dependence and contributions from different plasmonic modes

Finally, we performed experiments to elucidate the distance-dependence of the observed hot-carrier generation rates. Specifically, we measured the hot-carrier current flowing through Au-L1-Au SMJs at a voltage bias of 0.1V for varying separations from the grating edge on a 6 nm-thick gold film (Figure 7.4). It can be seen that the hot-carrier current decreases as the separation from the edge of the gratings increases and I_{hot} drops close to zero for separations larger than 7.5 μm.
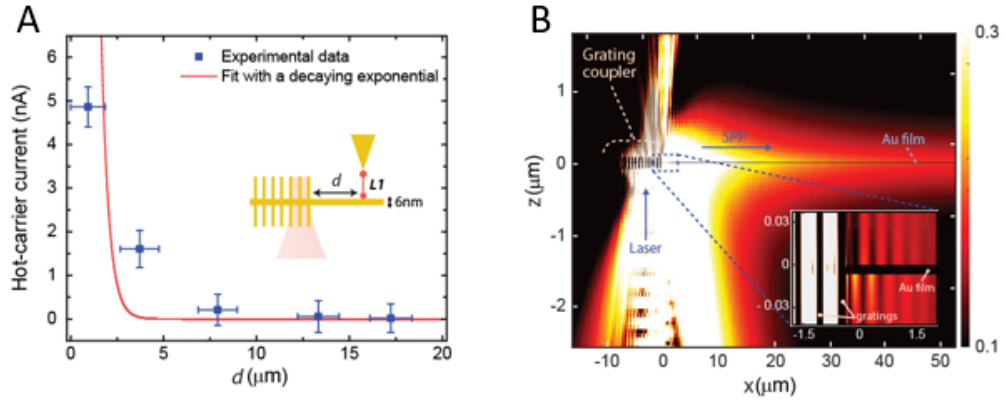
Fig. 7.4. (A) Measured hot-carrier current through Au-L1-Au SMJs (at 0.1V bias voltage) for varying separations d between the tip of the STM probe and the grating edge as shown in the schematic. The error bars correspond to the uncertainty in the separation d and the uncertainty in the hot-carrier current, respectively. The red curve is an exponential fit with a decay constant equal to the estimated propagation length of the symmetric plasmonic mode in 6 nm gold film and ϵ_{Au} = -28.8 +1.6i. (B) Simulated intensity profile upon illuminating the gratings with a focused 830 nm laser beam, showing the power coupled into the Au film. The gold film thickness was 6 nm, and a focused Gaussian beam with a spot size of 5.6 μm at the focal point was used in these calculations. The inset in the bottom right is the magnified image of the intensity profile close to the grating edge. The observed beating pattern in the inset confirms the excitation of both the symmetric and anti-symmetric modes near the grating edge, while for separations larger than 5 − 10 μm only the anti-symmetric mode remains. The color map of the inset is adjusted to show the beating pattern, and is different from the main panel color map.

To understand the observed distance dependence, we first simulated (using the Lumerical FDTD package) the intensity profile in the 6 nm-thick plasmonic Au film upon illuminating the grating coupler with an 830 nm laser. As shown in Figure 7.4B, we observe a beating profile close to the gratings, which we attribute to the interference between the two plasmonic modes (see inset in Figure 7.4B and computational methods in section 7.3, for additional details). However, for separations larger than 10 μm from the grating edge the symmetric mode decays while the anti-symmetric mode remains with nearly unchanged amplitude. Since there are no observed hot-carriers at large separations, in spite of the presence of the anti-symmetric mode, we conclude that the contribution of the anti-symmetric mode to hot-electron generation is negligible. In order to explore the relative contribution of symmetric and antisymmetric modes to hot-carrier generation, we performed additional calculations (Figure 7.3B), which clearly predict that the anti-symmetric mode is indeed much less effective in generating hot-electrons, resulting in 400-times (30-times) fewer carriers, in comparison to the symmetric mode for the 6 nm (13 nm)-thick film.

7.3 Computational methods for estimating the electromagnetic field profile and temperature rise

7.3.1 Optimization of the SPP coupler

We optimized the plasmonic grating coupler design, aiming to maximize the coupling efficiency of the illuminated focused beam ($\lambda = 830nm$) into SPPs. The grating coupler design comprises of parallel and periodic rectangular ridges (period $= \Lambda$) (Figure 7.5A). For this geometry, the momentum conservation condition required for the excitation of SPP is given by [44]:

$$k_{SPP} = k_0 sin(\theta) + Ng, \tag{7.32}$$

here, $k_{SPP} = 2\pi/\lambda_{SPP}$ and k_0 are the wave-vectors of SPP and incident light respectively, while θ, N and $g = 2\pi/\Lambda$ correspond to the excitation angle, grating

order and grating momentum, respectively. For normal incidence ($\lambda = 0$) and for first grating order ($N = 1$), the momentum conservation condition requires $\Lambda = \lambda_{SPP}$ for efficient excitation of SPPs. This condition reduces the optimization space to two parameters—width and height of the grating ridges (Figure 7.5A).
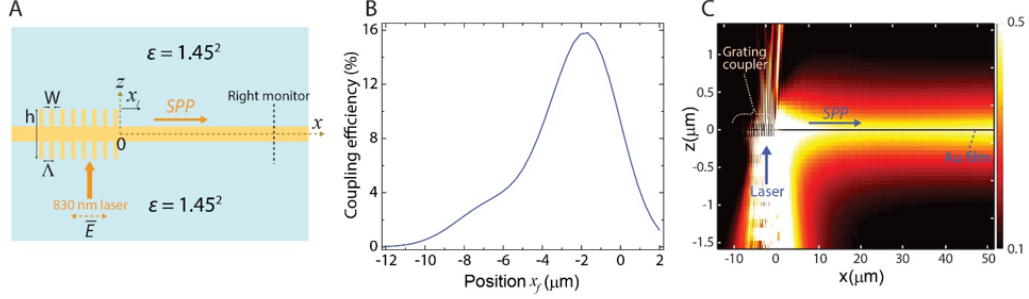
Fig. 7.5. Optimization of grating coupler. (A) Schematic showing the geometry of the simulation domain. The incident light polarization is indicated by a dashed orange line. (B) Coupling efficiency as a function of the incident laser focusing position x_f. (C) Simulated electric field intensity profile on a 13 nm-thick gold film, normalized to the incident field intensity.

In our simulations, we considered a focused Gaussian beam incident on the Au grating coupler with a background refractive index of n =1.45. A linearly polarized Gaussian beam, with a wavelength of 830 nm is assumed to be focused on the grating surface with 5.6 μm spot size (distance from waist 9 μm and a divergence angle of 12°), similar to the estimated focused spot size in our experiments. The polarization of the laser beam is chosen to be perpendicular to the grating strips, which enables the excitation of transverse magnetic modes. This polarization maximizes the excitation of SPPs. To optimize the parameters of the grating coupler a monitor was placed 50 μm away from the grating edge (see Figure 7.5A), and the optimization was performed using particle swarm optimization technique in Lumerical FDTD package. The width (w) and the height (h) of the ridges are optimized in the following ranges: $w \in [170nm, 460nm]$ and $h \in [50nm, 200nm]$. The optimized geometrical parameters of the Au grating coupler were found to be: $w = 220$ nm and $h = 80$ nm, while the

above mentioned momentum conservation condition and the background refractive index set the gating period $\Lambda = 572$ nm.

In such geometry, the excitation efficiency of SPPs is sensitive to the lateral position of the incident beam (along x) relative to the grating coupler [82]. To determine the best focusing position x_f we performed a parametric search, which swept from $x_{min} = $ -16 μm to $x_{max} = 2$ μm The origin of the coordinate system was chosen to be close to the right edge of the grating coupler (see Figure 7.5A), while the total length of the parametric sweep was set to be 18 μm. Figure 7.5B shows the dependence of the transmission through the right monitor (power coupled to the right propagating SPP), placed at x $= 50$ μm It can be seen that the optimal focusing spot for launching right-propagating SPPs is $x_f = $ -2 μm. With this focusing position, approximately 15% of the excitation beam energy couples to right-propagating SPP, while less than 5% couples to the left-propagating SPP. The origin of the asymmetry in the coupling efficiencies is due to second-order Bragg reflection from ridges, which converts part of the left-propagating SPP wave into right-propagating SPP. Another source of the reduced coupling to the left propagating SPP is the out-coupling of the SPP wave while propagating along the "long-arm" of the grating [82]. The computed spatial electric field intensity profiles ($|E|^2$) for $x_f = $ -2 μm are shown in Figure 7.4 & 7.5C for two different gold film thicknesses.

It is evident from these electric field profiles that there is an oscillatory beating pattern close to the grating edge, indicating interference due to the excitation of both the symmetric and anti-symmetric plasmonic modes [83]. To further investigate this beating pattern and to estimate the relative amplitudes of the excited symmetric and anti-symmetric mode we performed another simulation of the electric field profile in a slightly modified geometry shown in Figure 7.6A. In this geometry, we included a high index dielectric ($\epsilon = 8$) above and below the grating coupler (see Figure 7.6A for the geometry considered in this simulation). This allowed us to block the incident, scattered light from interfering with the excited SPP modes, thereby revealing the interference purely due to the launched SPP modes. The simulated electric field dis-

tribution in this modified geometry is shown in Figure 7.6B, which clearly reveals the beating pattern close to the gratings. In Figure 7.6C we plot the electric field at a distance of 2.4 nm above the 7 nm Au film as a function of lateral displacement x. We fit the oscillating field intensity with a functional form $|E|^2 = ae^{-\alpha x}cos(kx+b)+c$—that describes the interference between a rapidly decaying wave and a nearly constant amplitude wave—and determined that the oscillation wavelength $2\pi/k$ to be 444 nm. This number is close to $\frac{2\pi}{K_{sy-spp}-K_{asy-spp}} = 442$ nm, where K_{sy-spp} and $K_{asy-spp}$ are the wavevectors of the symmetric and anti-symmetric SPP modes, respectively, thereby confirming that the interference is indeed due to the excitation of both the symmetric and anti-symmetric modes. Furthermore, from the fit, we estimated that the ratio of the amplitudes of the excited anti-symmetric and symmetric modes to be 2.8.
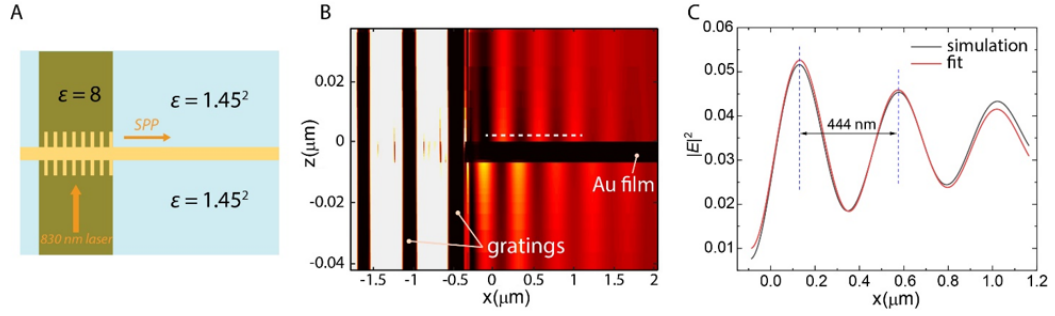
Fig. 7.6. Beating profile due to the interference of symmetric and anti-symmetric modes. (A) Schematic of the geometry considered to reveal the interference between symmetric and anti-symmetric SPP modes. In this geometry, a dielectric permittivity of $\epsilon = 8$ was used for the region above and below the grating coupler, while for the rest of the surrounding medium $\epsilon = 1.45^2$ as before. The grating coupler was illuminated with an 830 nm laser and the SPPs coupled to the right are analyzed. (B) Simulated electric field intensity profile in the geometry considered in (A) for a 6 nm-thick Au film. An oscillatory beating profile is observed. (C) Electric field intensity versus x at a height of 2.4 nm above the gold film, as indicated by the dashed line in (B). The fit in (C) was performed using the functional form of interference between a rapidly decaying wave and a constant amplitude wave as described above. The oscillation wavelength was found to be 444 nm.

7.3.2 Estimation of temperature rise due to the absorption of the incident laser power.

We performed an opto-thermal simulation to estimate the temperature rise due to the absorption of incident laser power. Our opto-thermal simulation proceeds in two steps. In the first step, the absorbed power in the gold film upon illuminating the optimized grating coupler with an 830 nm focused Gaussian beam ($P_{tot} = \frac{1}{2}\omega \int \int \int |E(x,y,z)|^2 imag(\epsilon_{Au})dxdydz$, beam waist of 5.6 μm at the focal spot and 6.6 mW laser power) was computed in Lumerical FDTD. The computed absorbed power was introduced as the heat source and the spatial temperature distribution was determined as the solution to heat diffusion equation in COMSOL multiphysics. We used a computational domain size of 480 x 480 x 250 μm^3 and imposed the convective heat transfer coefficient for gold-fused silica index matching oil as 250 W/m^{2}K—a typical number for oil heat transfer coefficients under free convection [84]. The fused silica substrate thermal conductivity was set at 1.4 W/m.K and all the exterior walls were set as constant ambient temperature (293.15 K) boundaries. The computed spatial profile of the temperature distribution with these parameters and boundary conditions in the xy and xz planes on a 6 nm-thick Au film are shown in Figure 7.7. These calculations revealed that the maximum temperature rise is about 67 °C. Furthermore, our additional analysis treating the conduction through the fused silica substrate as the dominant heat loss mechanism showed that the temperature rise is a few tens of kelvin, consistent with the estimates from our opto-thermal simulations.
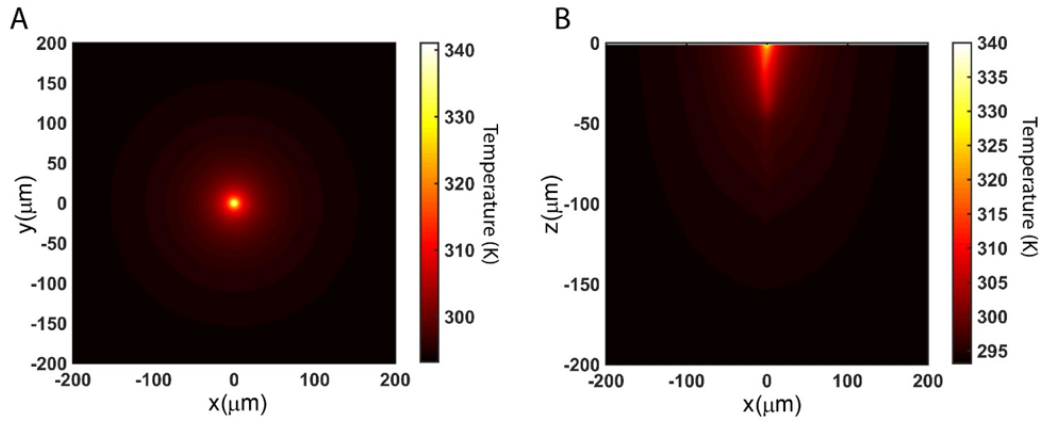
Fig. 7.7. Temperature increase due to the absorption of incident laser power. Spatial profile of the temperature distribution in the domain for 6 nm-thick gold film in xy (A) and xz planes (B).

7.4   Acknowledgements

I would like to acknowledge my colleagues Dr. Linxiao Zhu and Dr. Zhxylyk Kudyshev who contributed immensely to the theoretical estimates of the hot-carrier energy distributions, and field profile and temperature rise simulations, respectively, that are described in this chapter.

8. CONCLUSIONS AND OUTLOOK

This thesis work describes the development of experimental methods to probe and understand a variety of light-matter interactions in plasmonic nanostructures. Plasmonic nanostructures offer unique routes to engineer and enhance light-matter interactions at unprecedented length scales. However, an unavoidable consequence of this strong confinement is the emergence of strong losses that are either radiative or non-radiative in nature. In this work, we explored both the expected consequences of non-radiative losses on the material optical properties and also engineered and enhanced the non-radiative losses to generate energetic "hot-carriers". We developed innovative experimental tools to explore and unravel the rich physics governing the light-matter interactions in plasmonic nanostructures.

One of the most important contributions was to exploit the scanning probe based quantum transport measurements through molecular junctions to gain key insights into the nature of hot-carrier energy distributions in nanoplasmonic systems. The unique and distinctive transmission characteristics of molecular and atomic junctions have been widely used to study the fundamental charge and energy transport properties at the atomic scale. The study presented in this thesis [85] pushes the boundaries of quantum transport and combines molecular electronics with nanoplasmonics—opening a new direction of research to systematically address a variety of interesting questions in plasmonics. It is the hope of the author that the methods developed in this study will motivate interest and perhaps create a path towards elucidating the role of plasmonic hot-spots in hot-carrier generation, nanometer-scale spatial profiling of hot-carriers and correlating hot-carrier distributions with the electromagnetic field distribution in a range of plasmonic nanostructures, which have all been explored theoretically [31, 33] but have thus far remained inaccessible due to the lack of suitable experimental tools. Finally, on a speculative note, advancing

the techniques presented in this thesis even further and integrating them with the recently developed ultra-sensitive *picowatt resolution* scanning-probe based calorimeters [38, 58] could potentially enable experimental platforms to systematically investigate the kinetics of hot-carrier mediated chemical reactions at the single molecule level. If successful, such studies would provide foundational insights into the role of hot-carriers in reducing the activation barriers and catalyzing the chemical reactions.

REFERENCES

REFERENCES

[1] E. Ozbay, "Plasmonics: merging photonics and electronics at nanoscale dimensions," *science*, vol. 311, no. 5758, pp. 189–193, 2006.

[2] M. L. Brongersma and V. M. Shalaev, "The case for plasmonics," *science*, vol. 328, no. 5977, pp. 440–441, 2010.

[3] S. A. Maier and H. A. Atwater, "Plasmonics: Localization and guiding of electromagnetic energy in metal/dielectric structures," *Journal of applied physics*, vol. 98, no. 1, p. 10, 2005.

[4] J. B. Khurgin, "How to deal with the loss in plasmonics and metamaterials," *Nature nanotechnology*, vol. 10, no. 1, pp. 2–6, 2015.

[5] N. Zhou, X. Xu, A. T. Hammack, B. C. Stipe, K. Gao, W. Scholz, and E. C. Gage, "Plasmonic near-field transducer for heat-assisted magnetic recording," *Nanophotonics*, vol. 3, no. 3, pp. 141–155, 2014.

[6] M. H. Kryder, E. C. Gage, T. W. McDaniel, W. A. Challener, R. E. Rottmayer, G. Ju, Y.-T. Hsia, and M. F. Erden, "Heat assisted magnetic recording," *Proceedings of the IEEE*, vol. 96, no. 11, pp. 1810–1835, 2008.

[7] W. Challener, C. Peng, A. Itagi, D. Karns, W. Peng, Y. Peng, X. Yang, X. Zhu, N. Gokemeijer, Y.-T. Hsia *et al.*, "Heat-assisted magnetic recording by a near-field transducer with efficient optical energy transfer," *Nature photonics*, vol. 3, no. 4, pp. 220–224, 2009.

[8] E. I. Galanzha, R. Weingold, D. A. Nedosekin, M. Sarimollaoglu, A. S. Kuchyanov, R. G. Parkhomenko, A. I. Plekhanov, M. I. Stockman, and V. P. Zharov, "Spaser as novel versatile biomedical tool," *arXiv preprint arXiv:1501.00342*, 2015.

[9] U. Guler, J. C. Ndukaife, G. V. Naik, A. A. Nnanna, A. V. Kildishev, V. M. Shalaev, and A. Boltasseva, "Local heating with lithographically fabricated plasmonic titanium nitride nanoparticles," *Nano letters*, vol. 13, no. 12, pp. 6078–6083, 2013.

[10] L. R. Hirsch, R. J. Stafford, J. A. Bankson, S. R. Sershen, B. Rivera, R. Price, J. D. Hazle, N. J. Halas, and J. L. West, "Nanoshell-mediated near-infrared thermal therapy of tumors under magnetic resonance guidance," *Proceedings of the National Academy of Sciences*, vol. 100, no. 23, pp. 13 549–13 554, 2003.

[11] D. P. O'Neal, L. R. Hirsch, N. J. Halas, J. D. Payne, and J. L. West, "Photothermal tumor ablation in mice using near infrared-absorbing nanoparticles," *Cancer letters*, vol. 209, no. 2, pp. 171–176, 2004.

[12] U. Guler, A. Boltasseva, and V. M. Shalaev, "Refractory plasmonics," *Science*, vol. 344, no. 6181, pp. 263–264, 2014.

[13] E. Rephaeli and S. Fan, "Absorber and emitter for solar thermo-photovoltaic systems to achieve efficiency exceeding the shockley-queisser limit," *Optics express*, vol. 17, no. 17, pp. 15 145–15 159, 2009.

[14] A. Lenert, D. M. Bierman, Y. Nam, W. R. Chan, I. Celanović, M. Soljačić, and E. N. Wang, "A nanophotonic solar thermophotovoltaic device," *Nature nanotechnology*, vol. 9, no. 2, p. 126, 2014.

[15] K. Nanda, "Size-dependent melting of nanoparticles: Hundred years of thermodynamic model," *Pramana*, vol. 72, no. 4, pp. 617–628, 2009.

[16] G. V. Naik, V. M. Shalaev, and A. Boltasseva, "Alternative plasmonic materials: beyond gold and silver," *Advanced Materials*, vol. 25, no. 24, pp. 3264–3294, 2013.

[17] P. R. West, S. Ishii, G. V. Naik, N. K. Emani, V. M. Shalaev, and A. Boltasseva, "Searching for better plasmonic materials," *Laser & Photonics Reviews*, vol. 4, no. 6, pp. 795–808, 2010.

[18] W. Li, U. Guler, N. Kinsey, G. V. Naik, A. Boltasseva, J. Guan, V. M. Shalaev, and A. V. Kildishev, "Refractory plasmonics with titanium nitride: broadband metamaterial absorber," *Advanced Materials*, vol. 26, no. 47, pp. 7959–7965, 2014.

[19] H. Reddy, U. Guler, A. V. Kildishev, A. Boltasseva, and V. M. Shalaev, "Temperature-dependent optical properties of gold thin films," *Optical Materials Express*, vol. 6, no. 9, pp. 2776–2802, 2016.

[20] J. M. Ziman, *Principles of the Theory of Solids*. Cambridge university press, 1972.

[21] C. Clavero, "Plasmon-induced hot-electron generation at nanoparticle/metal-oxide interfaces for photovoltaic and photocatalytic devices," *Nature Photonics*, vol. 8, no. 2, p. 95, 2014.

[22] S. Linic, P. Christopher, and D. B. Ingram, "Plasmonic-metal nanostructures for efficient conversion of solar to chemical energy," *Nature materials*, vol. 10, no. 12, pp. 911–921, 2011.

[23] S. Linic, U. Aslam, C. Boerigter, and M. Morabito, "Photochemical transformations on plasmonic metal nanoparticles," *Nature materials*, vol. 14, no. 6, pp. 567–576, 2015.

[24] L. Zhou, D. F. Swearer, C. Zhang, H. Robatjazi, H. Zhao, L. Henderson, L. Dong, P. Christopher, E. A. Carter, P. Nordlander *et al.*, "Quantifying hot carrier and thermal contributions in plasmonic photocatalysis," *Science*, vol. 362, no. 6410, pp. 69–72, 2018.

[25] A. Naldoni, F. Riboni, U. Guler, A. Boltasseva, V. M. Shalaev, and A. V. Kildishev, "Solar-powered plasmon-enhanced heterogeneous catalysis," *Nanophotonics*, vol. 5, no. 1, pp. 112–133, 2016.

[26] M. W. Knight, H. Sobhani, P. Nordlander, and N. J. Halas, "Photodetection with active optical antennas," *Science*, vol. 332, no. 6030, pp. 702–704, 2011.

[27] H. Chalabi, D. Schoen, and M. L. Brongersma, "Hot-electron photodetection with a plasmonic nanostripe antenna," *Nano letters*, vol. 14, no. 3, pp. 1374–1380, 2014.

[28] A. Sobhani, M. W. Knight, Y. Wang, B. Zheng, N. S. King, L. V. Brown, Z. Fang, P. Nordlander, and N. J. Halas, "Narrowband photodetection in the near-infrared with a plasmon-induced hot electron device," *Nature communications*, vol. 4, no. 1, pp. 1–6, 2013.

[29] A. O. Govorov, H. Zhang, and Y. K. Gun'ko, "Theory of photoinjection of hot plasmonic carriers from metal nanostructures into semiconductors and surface molecules," *The Journal of Physical Chemistry C*, vol. 117, no. 32, pp. 16 616–16 631, 2013.

[30] R. Sundararaman, P. Narang, A. S. Jermyn, W. A. Goddard III, and H. A. Atwater, "Theoretical predictions for hot-carrier generation from surface plasmon decay," *Nature communications*, vol. 5, no. 1, pp. 1–8, 2014.

[31] A. Manjavacas, J. G. Liu, V. Kulkarni, and P. Nordlander, "Plasmon-induced hot carriers in metallic nanoparticles," *ACS nano*, vol. 8, no. 8, pp. 7630–7638, 2014.

[32] J. B. Khurgin, "Hot carriers generated by plasmons: where are they generated and where do they go from there?" *Faraday discussions*, vol. 214, pp. 35–58, 2019.

[33] H. Zhang and A. O. Govorov, "Optical generation of hot plasmonic carriers in metal nanocrystals: the effects of shape and field enhancement," *The Journal of Physical Chemistry C*, vol. 118, no. 14, pp. 7606–7614, 2014.

[34] Y. Dubi and Y. Sivan, ""hot" electrons in metallic nanostructures—non-thermal carriers or heating?" *Light: Science & Applications*, vol. 8, no. 1, pp. 1–8, 2019.

[35] T. Heilpern, M. Manjare, A. O. Govorov, G. P. Wiederrecht, S. K. Gray, and H. Harutyunyan, "Determination of hot carrier energy distributions from inversion of ultrafast pump-probe reflectivity measurements," *Nature communications*, vol. 9, no. 1, pp. 1–6, 2018.

[36] B. Xu and N. J. Tao, "Measurement of single-molecule resistance by repeated formation of molecular junctions," *science*, vol. 301, no. 5637, pp. 1221–1223, 2003.

[37] P. Reddy, S.-Y. Jang, R. A. Segalman, and A. Majumdar, "Thermoelectricity in molecular junctions," *Science*, vol. 315, no. 5818, pp. 1568–1571, 2007.

[38] L. Cui, W. Jeong, S. Hur, M. Matt, J. C. Klöckner, F. Pauly, P. Nielaba, J. C. Cuevas, E. Meyhofer, and P. Reddy, "Quantized thermal transport in single-atom junctions," *Science*, vol. 355, no. 6330, pp. 1192–1195, 2017.

[39] J.-L. Stehle and P. Boher, "Method and apparatus for ellipsometric metrology for a sample contained in a chamber or the like," Feb. 3 2004, uS Patent 6,687,002.

[40] H. Reddy, U. Guler, K. Chaudhuri, A. Dutta, A. V. Kildishev, V. M. Shalaev, and A. Boltasseva, "Temperature-dependent optical properties of single crystalline and polycrystalline silver thin films," *ACS Photonics*, vol. 4, no. 5, pp. 1083–1091, 2017.

[41] H. Reddy, U. Guler, Z. Kudyshev, A. V. Kildishev, V. M. Shalaev, and A. Boltasseva, "Temperature-dependent optical properties of plasmonic titanium nitride thin films," *ACS photonics*, vol. 4, no. 6, pp. 1413–1420, 2017.

[42] J. Trollmann and A. Pucci, "Infrared dielectric function of gold films in relation to their morphology," *The Journal of Physical Chemistry C*, vol. 118, no. 27, pp. 15 011–15 018, 2014.

[43] J. Hyuk Park, P. Nagpal, S.-H. Oh, and D. J. Norris, "Improved dielectric functions in metallic films obtained via template stripping," *Applied Physics Letters*, vol. 100, no. 8, p. 081105, 2012.

[44] S. A. Maier, *Plasmonics: fundamentals and applications.* Springer Science & Business Media, 2007.

[45] J. B. Herzog, M. W. Knight, and D. Natelson, "Thermoplasmonics: quantifying plasmonic heating in single nanowires," *Nano letters*, vol. 14, no. 2, pp. 499–503, 2014.

[46] Z. J. Coppens, W. Li, D. G. Walker, and J. G. Valentine, "Probing and controlling photothermal heat generation in plasmonic nanostructures," *Nano letters*, vol. 13, no. 3, pp. 1023–1028, 2013.

[47] G. Baffou and R. Quidant, "Thermo-plasmonics: using metallic nanostructures as nano-sources of heat," *Laser & Photonics Reviews*, vol. 7, no. 2, pp. 171–187, 2013.

[48] D. A. Boyd, L. Greengard, M. Brongersma, M. Y. El-Naggar, and D. G. Goodwin, "Plasmon-assisted chemical vapor deposition," *Nano letters*, vol. 6, no. 11, pp. 2592–2597, 2006.

[49] C.-Y. Young, "The frequency and temperature dependence of the optical effective mass of conduction electrons in simple metals," *Journal of Physics and Chemistry of Solids*, vol. 30, no. 12, pp. 2765–2769, 1969.

[50] W. Lawrence and J. Wilkins, "Electron-electron scattering in the transport coefficients of simple metals," *Physical Review B*, vol. 7, no. 6, p. 2317, 1973.

[51] T. Holstein, "Theory of transport phenomena in an electron-phonon gas," *Annals of Physics*, vol. 29, no. 3, pp. 410–535, 1964.

[52] R. Beach and R. Christy, "Electron-electron scattering in the intraband optical conductivity of cu, ag, and au," *Physical Review B*, vol. 16, no. 12, p. 5277, 1977.

[53] W. Lawrence, "Electron-electron scattering in the low-temperature resistivity of the noble metals," *Physical Review B*, vol. 13, no. 12, p. 5316, 1976.

[54] S. Datta, *Electronic transport in mesoscopic systems.* Cambridge university press, 1997.

[55] A. Vezzoli, I. Grace, C. Brooke, K. Wang, C. J. Lambert, B. Xu, R. J. Nichols, and S. J. Higgins, "Gating of single molecule junction conductance by charge transfer complex formation," *Nanoscale*, vol. 7, no. 45, pp. 18 949–18 955, 2015.

[56] K. Wang, A. Vezzoli, I. M. Grace, M. McLaughlin, R. J. Nichols, B. Xu, C. J. Lambert, and S. J. Higgins, "Charge transfer complexation boosts molecular conductance through fermi level pinning," *Chemical Science*, vol. 10, no. 8, pp. 2396–2403, 2019.

[57] B. Capozzi, J. Z. Low, J. Xia, Z.-F. Liu, J. B. Neaton, L. M. Campos, and L. Venkataraman, "Mapping the transmission functions of single-molecule junctions," *Nano letters*, vol. 16, no. 6, pp. 3949–3954, 2016.

[58] W. Lee, K. Kim, W. Jeong, L. A. Zotti, F. Pauly, J. C. Cuevas, and P. Reddy, "Heat dissipation in atomic-scale junctions," *Nature*, vol. 498, no. 7453, pp. 209–212, 2013.

[59] J. J. Apperloo, L. Groenendaal, H. Verheyen, M. Jayakannan, R. A. Janssen, A. Dkhissi, D. Beljonne, R. Lazzaroni, and J.-L. Brédas, "Optical and redox properties of a series of 3, 4-ethylenedioxythiophene oligomers," *Chemistry–A European Journal*, vol. 8, no. 10, pp. 2384–2396, 2002.

[60] G. V. Hartland, L. V. Besteiro, P. Johns, and A. O. Govorov, "What's so hot about electrons in metal nanoparticles?" *ACS Energy Letters*, vol. 2, no. 7, pp. 1641–1653, 2017.

[61] I. Doron-Mor, Z. Barkay, N. Filip-Granit, A. Vaskevich, and I. Rubinstein, "Ultrathin gold island films on silanized glass. morphology and optical properties," *Chemistry of Materials*, vol. 16, no. 18, pp. 3476–3483, 2004.

[62] T. Karakouz, D. Holder, M. Goomanovsky, A. Vaskevich, and I. Rubinstein, "Morphology and refractive index sensitivity of gold island films," *Chemistry of Materials*, vol. 21, no. 24, pp. 5875–5885, 2009.

[63] A. Kossoy, V. Merk, D. Simakov, K. Leosson, S. Kéna-Cohen, and S. A. Maier, "Optical and structural properties of ultra-thin gold films," *Advanced Optical Materials*, vol. 3, no. 1, pp. 71–77, 2015.

[64] M. Hu, S. Noda, T. Okubo, Y. Yamaguchi, and H. Komiyama, "Structure and morphology of self-assembled 3-mercaptopropyltrimethoxysilane layers on silicon oxide," *Applied surface science*, vol. 181, no. 3-4, pp. 307–316, 2001.

[65] C. A. Goss, D. H. Charych, and M. Majda, "Application of (3-mercaptopropyl) trimethoxysilane as a molecular adhesive in the fabrication of vapor-deposited gold electrodes on glass substrates," *Analytical Chemistry*, vol. 63, no. 1, pp. 85–88, 1991.

[66] B. Ren, G. Picardi, and B. Pettinger, "Preparation of gold tips suitable for tip-enhanced raman spectroscopy and light emission by electrochemical etching," *Review of Scientific Instruments*, vol. 75, no. 4, pp. 837–841, 2004.

[67] L. Cui, R. Miao, C. Jiang, E. Meyhofer, and P. Reddy, "Perspective: Thermal and thermoelectric transport in molecular junctions," *The Journal of Chemical Physics*, vol. 146, no. 9, p. 092201, 2017.

[68] B. Capozzi, J. Xia, O. Adak, E. J. Dell, Z.-F. Liu, J. C. Taylor, J. B. Neaton, L. M. Campos, and L. Venkataraman, "Single-molecule diodes with high rectification ratios through environmental control," *Nature nanotechnology*, vol. 10, no. 6, p. 522, 2015.

[69] A. Archambault, F. Marquier, J.-J. Greffet, and C. Arnold, "Quantum theory of spontaneous and stimulated emission of surface plasmons," *Physical Review B*, vol. 82, no. 3, p. 035411, 2010.

[70] S. I. Bozhevolnyi and K. V. Nerkararyan, "Channel plasmon polaritons guided by graded gaps: closed-form solutions," *Optics express*, vol. 17, no. 12, pp. 10 327–10 334, 2009.

[71] P. Berini, "Long-range surface plasmon polaritons," *Advances in optics and photonics*, vol. 1, no. 3, pp. 484–588, 2009.

[72] A. D. Rakić, A. B. Djurišić, J. M. Elazar, and M. L. Majewski, "Optical properties of metallic films for vertical-cavity optoelectronic devices," *Applied optics*, vol. 37, no. 22, pp. 5271–5283, 1998.

[73] R. Sundararaman, K. Letchworth-Weaver, K. A. Schwarz, D. Gunceler, Y. Ozhabes, and T. Arias, "Jdftx: software for joint density-functional theory," *SoftwareX*, vol. 6, pp. 278–284, 2017.

[74] J. P. Perdew, A. Ruzsinszky, G. I. Csonka, O. A. Vydrov, G. E. Scuseria, L. A. Constantin, X. Zhou, and K. Burke, "Restoring the density-gradient expansion for exchange in solids and surfaces," *Physical review letters*, vol. 100, no. 13, p. 136406, 2008.

[75] S. Dudarev, G. Botton, S. Savrasov, C. Humphreys, and A. Sutton, "Electron-energy-loss spectra and the structural stability of nickel oxide: An lsda+ u study," *Physical Review B*, vol. 57, no. 3, p. 1505, 1998.

[76] N. Marzari and D. Vanderbilt, "Maximally localized generalized wannier functions for composite energy bands," *Physical review B*, vol. 56, no. 20, p. 12847, 1997.

[77] I. Souza, N. Marzari, and D. Vanderbilt, "Maximally localized wannier functions for entangled energy bands," *Physical Review B*, vol. 65, no. 3, p. 035109, 2001.

[78] M. Lundstrom, *Fundamentals of carrier transport.* Cambridge university press, 2009.

[79] L. V. Besteiro, X.-T. Kong, Z. Wang, G. Hartland, and A. O. Govorov, "Understanding hot-electron generation and plasmon relaxation in metal nanocrystals: Quantum and classical mechanisms," *Acs Photonics*, vol. 4, no. 11, pp. 2759–2781, 2017.

[80] R. H. Groeneveld, R. Sprik, and A. Lagendijk, "Femtosecond spectroscopy of electron-electron and electron-phonon energy relaxation in ag and au," *Physical Review B*, vol. 51, no. 17, p. 11433, 1995.

[81] P. Coleman, *Introduction to many-body physics.* Cambridge University Press, 2015.

[82] I. Radko, S. I. Bozhevolnyi, G. Brucoli, L. Martín-Moreno, F. García-Vidal, and A. Boltasseva, "Efficient unidirectional ridge excitation of surface plasmons," *Optics express*, vol. 17, no. 9, pp. 7228–7232, 2009.

[83] J. M. Montgomery and S. K. Gray, "Enhancing surface plasmon polariton propagation lengths via coupling to asymmetric waveguide structures," *Physical Review B*, vol. 77, no. 12, p. 125407, 2008.

[84] F. P. Incropera, A. S. Lavine, T. L. Bergman, and D. P. DeWitt, *Fundamentals of heat and mass transfer.* Wiley, 2007.

[85] H. Reddy, K. Wang, Z. Kudyshev, L. Zhu, S. Yan, A. Vezzoli, S. J. Higgins, V. Gavini, A. Boltasseva, P. Reddy, V. M. Shalaev, and E. Meyhofer, "Determining plasmonic hot-carrier energy distributions via single-molecule transport measurements," *Science*, vol. 369, no. 6502, pp. 423–426, 2020.